Investigations on Stokes polarization parameters of Vertical-Cavity Surface-Emitting Lasers: spatially, spectrally and time-resolved

TECHNISCHE
UNIVERSITÄT
DARMSTADT

Fachbereich Physik
Institut für Angewandte Physik
Halbleiteroptik

Investigations on Stokes polarization parameters of Vertical-Cavity Surface-Emitting Lasers: spatially, spectrally and time-resolved

Approved Dissertation by Dipl.-Phys. Andreas Molitor from Worms

First referee: Prof. Dr. Wolfgang Elsäßer
Second referee: Prof. Dr. Thomas Walther

Day of submission: 19.11.2014
Day of examination: 10.12.2014

Darmstadt – D17

Table of Content

1. Introduction

Their unique geometrical structure first suggested by Prof. Kenichi Iga in 1977 [1] [2], makes vertical-cavity surface-emitting lasers (VCSELs) compact, versatile, robust and reliable optoelectronic devices, which have already outperformed edge-emitting lasers (EELs) in terms of low threshold current and high wall-plug efficiency. Most relevantly, regarding application field entering and mass production, is their low cost manufacturing due to their property of enabling wafer-level testing. In addition to these benefits provided by their vertical design, VCSELs exhibit complex polarization behavior resulting from the circular symmetry of their resonator and from the isotropic gain of their active medium, mostly based on quantum well (QW) [3] [4] or quantum dots (QD) [5]. In principle, the polarization of the light emitted by these optoelectronic devices should reflect the selection rules of the quantum well (QW) optical transition symmetry and thus should exhibit a circularly polarized state of light. However, various symmetry breaking mechanisms [6], such as strain [7] [8], thermal effects [9] [10], electro-optically induced birefringence [11] [12], dichroism [13] or an applied magnetic field [14] convert this circular polarization to an elliptically polarized emission, often with a large amount of linearly polarized light. Therefore, at a first glance, polarization resolved investigations, using a linear polarizer only, on intensity noise [15], wave chaos [16], transverse mode behavior [17] [18] and time-resolved measurements [19] [20] are legitimized, although being restricted to a projection on two orthogonal linear polarization components. But clearly these kinds of measurements do not reveal the entire knowledge of the polarization state, due to the conversion of an eventual circular component into a linear component.

In contrast to this rather simple, straightforward projection method the full information about the state of polarization is accessible only by determining the four Stokes polarization parameters (SPPs) S_0, S_1, S_2 and S_3. The remarkable fact of these four parameters is that they are directly measurable quantities, thus enabling the complete description of any state of polarization in mathematical terms, including unpolarized light as well as partially polarized light. Noteworthy about the Stokes formalism is the fact, that it has been invented already in 1852 by Sir George Gabriel Stokes [21]. During this time, a crisis in optics appeared due to fundamentally different approaches namely the wave- as well as the corpuscular-ansatz. The formulation of the SPPs essentially supports the wave theory, providing explanation of the famous Fresnel-Arago interference laws on the basis of the wave approach for the first time. These SPPs, formulated in 1852, are even nowadays the appropriate formalism to describe the complex polarization behavior of VCSELs.

The aim of this work is to conduct comprehensive experimental investigations on spatially, spectrally and time-resolved SPPs of transverse single-mode and transverse multi-mode VCSELs. Furthermore, combined measurements such as spatio-spectrally as well as spectro-temporally resolved measurements will also be performed and compared among each other, demonstrating the consistency and reliability of these quantitative results. Moreover, a detailed analysis of each particular transverse mode will be performed, uncovering the

physical mechanisms responsible for the state of polarization of the total emission of transverse single-mode as well as multi-mode VCSELs. In addition the time dependence of polarization states of the total emission on a microsecond timescale will be investigated. These overall results in combination with investigations on time-resolved SPPs measurements for each particular transverse mode will be a point of origin for future numerical simulations.

In detail this thesis is organized as follows:

First, fundamental operating principles of VCSELs, their emission properties, as well as their polarization behavior are explained in chapter 2, followed by a detailed introduction of the Stokes formalism, where all necessary formulae and relations are explicitly given (chapter 3). At the end of chapter 3 the underlying measurement technique, representing the basis of this work, is explained in detail.

The manifold experimental results are presented in six chapters from which each has a similar structure. First, the underlying experimental setup is described, followed by the presentation and the discussion of the experimental results and finally a short summary together with a motivation for the next chapter is given. The motivation for these versatile investigations, schematically visualized in the pictogram below, is to experimentally quantify in detail the complex polarization behavior of each particular transverse mode under continuous wave as well as under pulsed operation, to understand the physical mechanisms.
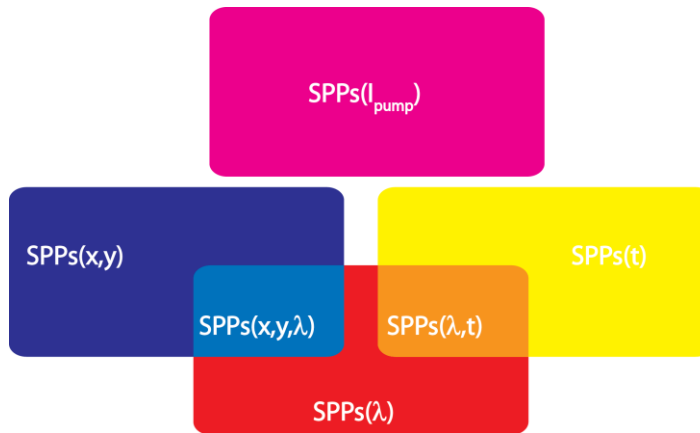
The first experimental results (chapter 4) on SPPs are spatially, spectrally and temporally integrated, however, resolved as a function of pump current ($SPPs(I_{pump})$). Representative VCSELs with different oxide aperture diameters have been selected, in order to cover transverse single-mode as well as transverse multi-mode operation regimes. Thereby, we recapitulate characteristic polarization behaviors according to the selected size of their oxide aperture diameter.

In chapter 5 we propose a modified experimental setup, enabling us to perform spatially resolved SPP measurements ($SPP(x,y)$). These experimentally obtained results ($SPPs_{exp}(x,y)$) of a transverse single-mode VCSEL are directly compared with their numerically simulated counterparts $SPPs_{sim}(x,y)$, allowing to unveil the physical mechanism of the observed complex spatial distribution.

In chapter 6 spatially resolved SPPs of each transverse mode of a multi-mode VCSEL are investigated individually. With these spatio-spectrally resolved SPPs (SPPs(x,y,λ)) for each particular transverse mode, the characteristic polarization behavior observed in chapter 4 can be explained.

The spectral resolution is further enhanced, allowing experimental access to highly resolved optical spectra, from which one can determine the polarization behavior of polarization modes belonging pairwise to one transverse mode, already predicted by theory. This ensures an even closer insight into the transverse mode behavior, down to their absolute spectral decomposition.

After already comprehensive investigations on VCSELs under continuous wave operation, we present in chapter 8 time-resolved SPPs (SPPs(t)) of pulsed VCSELs and compare them with continuous wave measurements showing interesting coincidences.

Then, in chapter 9, the time-resolved polarization behavior of each particular transverse mode is unveiled by investigating the spectro-temporally resolved SPPs (SPPs(λ,t)), uncovering fundamental findings such as the spectral redshift.

Finally the experimental results are summarized and essential outcomes are discussed in chapter 10, together with an outlook and some perspectives also according to numerical simulations.

2. Vertical-Cavity Surface-Emitting Lasers

In this chapter we outline the fundamental operating principle of vertical-cavity surface-emitting lasers (VCSELs), together with their unique emission properties, such as polarization, transverse mode and temperature behavior just to name a few. In addition, this introduction to VCSELs provides an overview of several applications of these versatile devices, covering a broad area of every-day-used semiconductor based technologies, such as computer mice, bar code scanners and printing heads. Further information can be found in several recent textbooks about VCSELs such as [22] [23] [24] [25]. This chapter is organized as follows: First, the principle structure of VCSELs is defined, along with resulting properties, providing advantage over edge-emitting lasers (EELs). After that, relevant emission properties to understand the experimental results presented in this thesis are shown and explained. Finally, a short overview of applications is given.
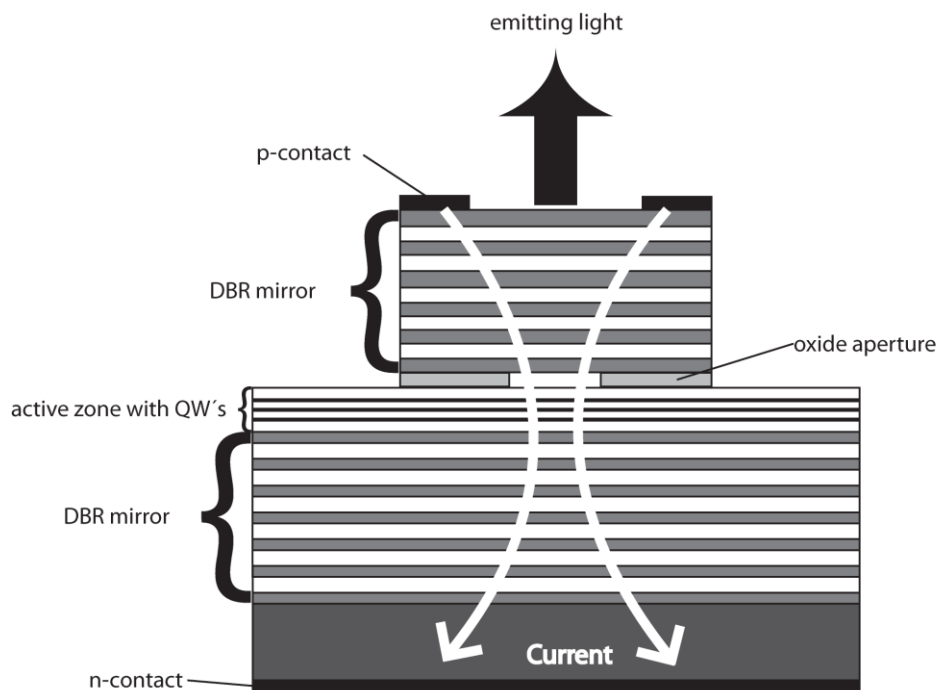
Figure 2.1 Schematic drawing of a typical structure of an oxide-confined VCSEL, containing the active layer consisting of a quantum well (QW) semiconductor material, sandwiched between two DBR mirrors, framed by the electrical n- and p-contact. The current as well as the light is guided in the transverse direction by an oxide aperture right above the active zone.

The fundamental principle of generating photons in nearly most of the optoelectronic devices is the electron-hole recombination from the conduction band (CB) to the valence band (VB), thus generating photons with the frequency υ corresponding to the energy gap of the two energy bands ($E_{CB} - \mathrm{E_{VB}} = \Delta\mathrm{E}$) via $\Delta\mathrm{E} = \mathrm{h}\upsilon$ (h=Planck constant, υ=frequency of the photon) [26]. Light emitting diodes (LEDs) are semiconductor optoelectronic devices, which permit current to flow in only one direction. A diode is formed by bringing two slightly different materials together to form a p-n junction, where p and n denote the semiconductor material

with a majority of positive (p) and negative (n) charge carriers, respectively. An applied forward bias voltage pushes both the electron-holes (positive carriers in the p-type region) as well as the electrons (negative carriers in the n-type region) toward the junction. Near the junction electrons and holes recombine and release their energy in form of light, emitted by the LED. In contrast to the rather simple concept of LEDs, semiconductor lasers, such as edge-emitting lasers (EELs) or vertical-cavity surface-emitting lasers (VCSELs) exhibit, beside the p-n junction, a resonator that can either be realized as a Fabry-Pérot type resonator in EELs, where the resonator is aligned perpendicular to the layer normal of the semiconductor layer material [25]. Or, on the other hand, the resonator can be aligned with the layer normal, as it is the case for VCSELs. This feature is a major advantage of VCSELs with respect to EELs. Because EELs have to be diced and packaged before they can be tested, these manufacturing steps are omitted in the production of VCSELs. This property enables, that they can directly be tested on wafer, thus making VCSELs a low cost mass production item. In the following, the unique structure of VCSELs is presented in detail again in comparison with EELs in some points.
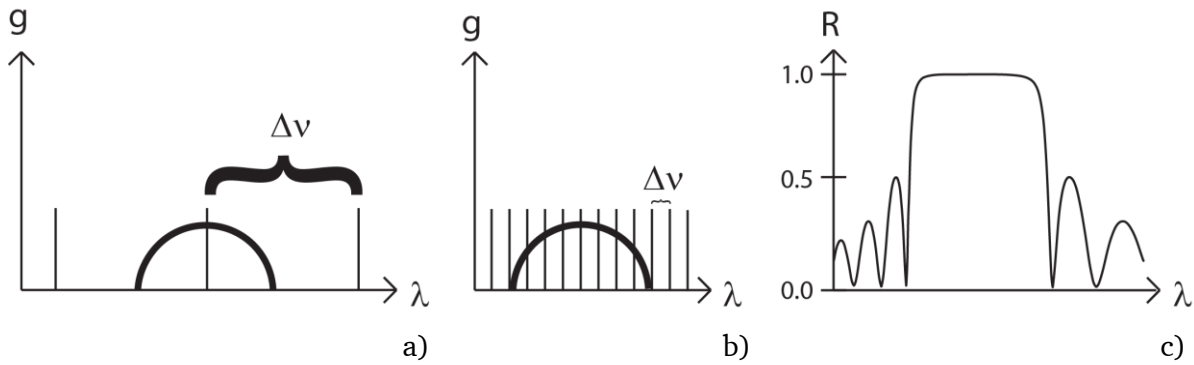

Figure 2.2 a)Sketch of the spectral longitudinal mode spacing of a VCSEL with a short cavity, resulting in a spacing exceeding the optical gain curve in comparison with the spectral longitudinal mode spacing of an EEL with a long cavity, resulting in a small spacing b) which has been taken to be equal for both devices, due to the same semiconductor active layer material. Reflectivity R of a DBR mirror as a function of the wavelength c).

In Fig. 2.1 a schematic drawing of a typical layer structure of a VCSEL is depicted, consisting of the active zone, where the photons are generated via electron-hole recombination. These photons propagate perpendicular to the semiconductor layer structure, guided by an oxide aperture and obeying the vertical cavity selection rules. The active zone is chosen to be quite short usually having an effective length in the order of about one wavelength, thus resulting in a large spacing Δv between the longitudinal Fabry-Pérot modes calculated via the following formula

$$\Delta v = \frac{c}{2nL} \tag{2.1}$$

c is the speed of light in vacuum, n is the refractive index of the active layer material and L is the geometric cavity length. This geometrical property of the cavity, in combination with the

utilized semiconductor material[1] characteristic spectral gain curve, results in longitudinal single-mode operation, depicted in Figure 2.2a) in comparison with edge-emitting lasers (EELs) schematically illustrated in Figure 2.2b), where the cavity is several hundreds of micrometers long, thus resulting in a reduced longitudinal mode spacing, leading to a longitudinal multi-mode operation.

Due to the small longitudinal dimension of the VCSELs cavity, the reflectivity R of the utilized mirrors has to be at least as high as 99% to enlarge the photon lifetime, thus enabling an amplification of spontaneously generated photons. Such a high reflectivity is realized by utilizing distributing Bragg reflecting mirrors (DBR mirrors). These structures composed of alternating high and low refracting layers of the thickness of one quarter of the material wavelength, exhibit a reflectivity R of over 99%, as it is visible from Figure 2.2c), illustrating exemplarily the reflectivity R of a DBR mirror as a function of the wavelength λ. The high reflectivity over 99%, depends on the amount N of utilized layers, clearly visible from the formula for the reflectivity R for a certain wavelength λ_0 such as

$$R = \left(\frac{n_O (n_2)^{2N} - n_S (n_1)^{2N}}{n_O (n_2)^{2N} + n_S (n_1)^{2N}} \right)^2 \tag{2.2}$$

$$\Delta\lambda_0 = \frac{4\lambda_0}{\pi} \arcsin \left(\frac{n_2 - n_1}{n_2 + n_1} \right) \tag{2.3}$$

where n_O, n_1, n_2 and n_s are denoting the refractive indices of the surrounding medium, the alternating materials 1 and 2 as well as the terminating substrate material, respectively. Formula (2.3) describes the width of the reflectivity $\Delta\lambda_0$ with respect to a central wavelength λ_0 as a function of the refractive indices of the alternating material n_1 and n_2. These two formulae clearly demonstrate that the reflectivity R as well as the width of the reflectivity $\Delta\lambda_0$ can be increased by increasing the number N of repeated pairs of high and low refractive index materials and the difference $n_2 - n_1$ of the refractive indices of these two materials, respectively. Beside the reflection of light in the longitudinal direction of the cavity, the reflection in the transverse direction is realized by an oxide aperture and will be explained in the following.

The oxide aperture confines the injected current as well as the optical field in the transverse direction and has usually a diameter of a few micrometers, resulting in a transverse single-mode operation together with a reduced laser threshold below 100μA [27]. For oxide aperture diameters exceeding 4μm, higher order transverse modes start lasing, thus resulting in higher optical output powers up to 100mW for devices with oxide aperture diameters up to 100μm [28] [29]. In Figure 2.3a) and c) the optical output power as a function of pump current (P-I curves) together with highly resolved optical spectra (Figure 2.3b) and c)) are illustrated for both a transverse single-mode VCSEL with an oxide aperture diameter of 3μm (red line) as well as a transverse multi-mode VCSEL with an oxide aperture diameter of 20μm

---

[1] Most of the VCSELs investigated in this thesis are based on the compound semiconductor material gallium arsenide (GaAs), thus resulting in an emission wavelength of 850nm. The only exception is the MEMS tunable VCSEL with an emission wavelength of 1550nm presented in appendix A based in indium gallium arsenide (InGaAs).

(black line). In addition spatio-spectrally resolved nearfield images of the emitting facet of the transverse single- (Figure 2.3b) and transverse multi-mode VCSEL (Figure 2.3d)) are visible, illustrating the complexity of transverse multi-mode VCSELs.
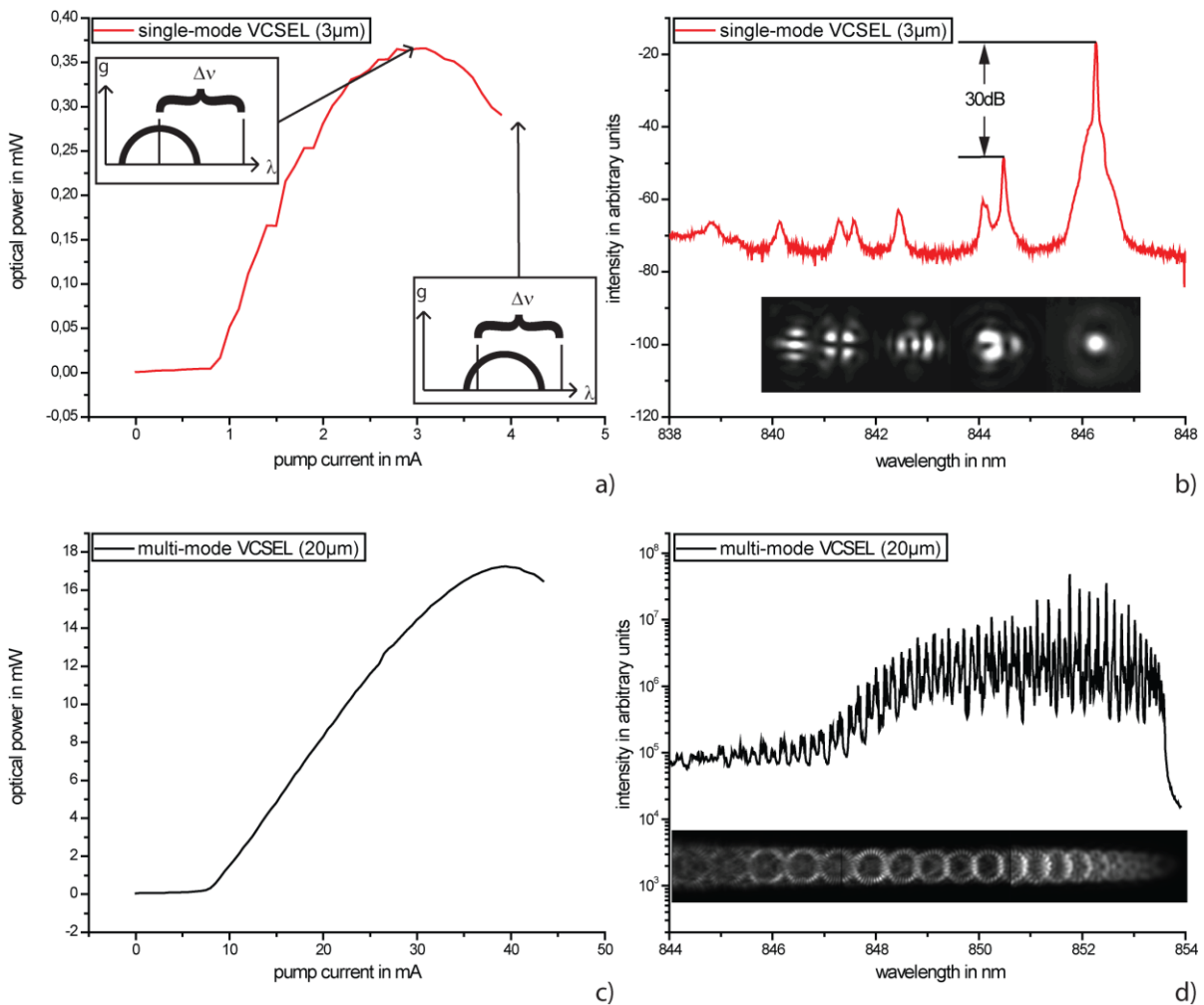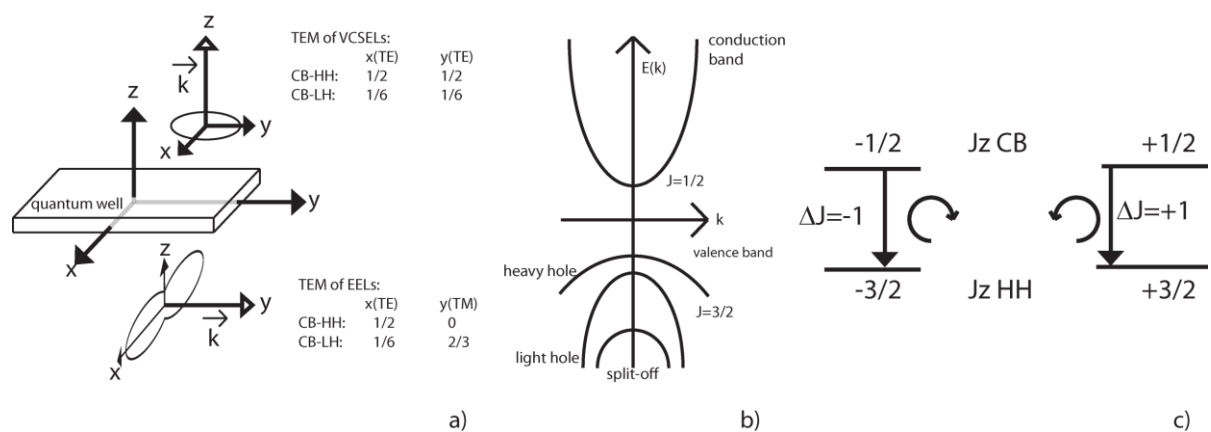

Figure 2.3 (left) P-I curve of a transverse single-mode VCSEL a) and a transverse multi-mode VCSEL c) with oxide aperture diameters of 3μm and 20μm, respectively. The insets in a) schematical depict the faster redshift of the spectral gain with respect to the cavity modes with increasing temperature, thus resulting in the thermally induced rollover. Right: Highly-resolved optical spectra of the same VCSELs, clearly demonstrating the transverse single-mode emission b) as well as the transverse multi-mode emission d) both together with spatio-spectrally resolved nearfield images, illustrating the complex transverse mode behavior a) as well as the Laguerre-Gaussian-shaped transverse intensity distribution d).

The experimentally obtained P-I curves are depicted in Figure 2.3a) and c), uncovering the characteristic kink at the laser threshold and the VCSELs characteristic thermally induced rollover, which will be explained later in more detail with the help of the schematic insets of the gain and the resonator modes. Moreover, the difference of both P-I curves with respect to their laser threshold values of below 1mA for the transverse single-mode VCSEL (red line) in comparison with the increased laser threshold of the transverse multi-mode VCSEL of about 7mA (black line), together with the different maximal optical output power of below 1mW and above 10mW for the transverse single- (red line) as well as for the transverse multi-mode VCSEL (black line), respectively.

The experimentally obtained optical spectra are depicted in Figure 2.3b) nicely illustrating the transverse single-mode operation with a side-mode suppression ratio (SMSR) of 30dB. In addition, spatio-spectrally resolved nearfield images clearly separate higher order transverse modes of the Laguerre-Gaussian mode family [30]. The spectral transverse mode spacing is reduced by increasing the oxide aperture diameter from $3\mu m$ (Figure 2.3b)) up to $20\mu m$ (Figure 2.3d)), such that the spatial transverse mode intensity distribution cannot be well separated from their nearest neighbors, resulting in a complex transverse mode pattern as it is clearly visible in the spatio-spectrally resolved nearfield images of the transverse multi-mode VCSEL. The influence of an enlargement of the oxide aperture diameter on the emission properties is clearly demonstrated here, regarding the optical output power as well as the transverse mode behavior. Beside the size of the oxide aperture diameter, the temperature influences the emission properties of VCSELs as well, as it is explained in the following section.

Because of the short cavity in the longitudinal direction the emission wavelength λ of the VCSEL is determined by the resonator peak and not by the gain peak as it is the case in conventional Fabry-Pérot type EELs, schematically depicted in Figure 2.2a) and b), respectively. The thermally induced spectral redshift of the resonator modes (vertical lines) depends on the material composition of the DBR mirrors as we already know from (2.2) and (2.3).

For VCSELs emitting in the spectral range between 800nm and 1000nm the thermally induced resonator mode redshift is typically to be $\partial\lambda/\partial T \approx 0.07nm/K$, enabling the estimation of internal temperature rise from measured redshifts of corresponding optical spectra. In contrast to this value the redshift of the peak material gain λ_g is about 0.32nm/K, thus resulting in different shift velocities. Hence, the spectral redshift of the optical spectra can be explained as well as the reduction of the optical output power with increasing pump current beyond the thermally induced rollover point (cf. Figure 2.3a)).

Figure 2.4 a) Schematic drawing of quantum well active material, together with the TME for VCSELs (top) and EELs (bottom), thus demonstrating the isotropic gain properties of VCSELs in contrast to the anisotropy of the gain of EELs. b) The energy band structure E as a function of the wave vector k shows the conduction band (CB) (top) together with the degenerated heavy hole valence band (HH) with a higher energy and the light hole valence band (LH) with a lower energy together with the split-off band with an almost negligible energy value. Furthermore, the total angular momentum values of J are depicted. c) The most probable transitions from the CB to the HH obeying the quantum selection rules $\Delta J=\pm 1$, thus resulting in right and left circular polarized generated photons represented by the clockwise and counterclockwise oriented bended arrows.

Furthermore, the quasi isotropic properties of both the gain as well as the circular resonator geometry in the plane of the active layer are the reason for the instable polarization, which means that the polarization changes from VCSEL to VCSEL merely by increasing the pump current showing polarization switching (PS) from one linearly polarized state to an orthogonally linearly polarized state of light. The isotropic properties, resulting in intrinsic polarization bistability can be explained via interband transition matrix elements (TME) [31] [32] reflecting the probability of a transition from the conduction band (CB) to the heavy hole valence band (HH) (CB-HH transition) as well as a transition from the CB to the light hole valence band (LH) (CB-LH transition), schematically depicted in Figure 2.4b). Here, the transition from the conduction band (CB) to the split off band can be neglected with respect to its low energy in comparison with HH and LH. Moreover, it can be shown that the probability of a CB-HH transition is three times higher than a CB-LH transition [26]. Furthermore, in comparison with EELs the probability for the CB-HH as well as the CB-LH transition is the same for both polarizations in the x- and in the y-direction, respectively (see Figure 2.4a)). In contrast to EELs, where the TME is zero for CB-HH transitions, thus resulting in anisotropy. However, there is no intrinsic polarization gain anisotropy mechanism in conventional VCSELs (cf. Figure 2.4a)).

Moreover, the polarization of the emitted light of such optoelectronic emitters, should reflect the selection rules of the quantum well optical transition, thus allowing a transition with a change of angular momentum of $J=\pm 1$ (see Figure 2.4c)). The total angular momentum of an electron state in the CB of zero momentum $k=0$ is $J=1/2$. In contrast to this, the valence band in particular the heavy hole and the light hole exhibits a total angular momentum $J=3/2$ and $J=1/2$, respectively. The non-degeneracy of HH and LH at $k=0$ is due to the quantum confinement in the z-direction with respect to the quantum well structure in comparison with bulk material (degeneracy of HH and LH at $k=0$), where the HH and the LH exhibit even the same energy. However, the angular momentum of the electrons is conserved and will be transferred to the generated photon, which means that, the angular momentum is reflected by a circular state of polarization. In more detail, right circularly polarized light corresponds to $\Delta J=-1$ and left circularly polarized light to $\Delta J=+1$ for example at the transition from the CB with $J_z^2=-1/2$ ($J_z=+1/2$) to the HH with $J_z=-3/2$ ($J_z=+3/2$) resulting in right and left circularly polarized light as it is schematically depicted in Figure 2.4c) neglecting the transition to the LH due to smaller energy values together with a three times lower transition probability as we know from the sequence above, regarding to the TME (cf. Figure 2.4a)).

In conclusion, the polarization state of light is in principle circular due to the optical selection rules for transition, supported by the circular device symmetry, together with the isotropic gain material properties. However, in the real world, semiconductor based optoelectronic emitter various symmetry breaking mechanisms, mentioned above, convert this circularly polarized emission to an elliptically polarized state of light. This elliptical polarization often exhibits a large amount of linear polarization, which at a first glance legitimates polarization resolved measurements on a linear orthogonal linear polarization basis utilizing a linear polarizer only. Further investigations on intensity noise [15], wave chaos [16] or transverse

---

[2] J_z means here the projection of the total angular momentum on the z-axis

mode dynamics [33] have already been measured for two orthogonally oriented polarizations. On the basis of this linear orthogonal polarization basis, even polarization switching (PS) phenomena including polarization bistability have been investigated [34] and are described in the following in more detail.
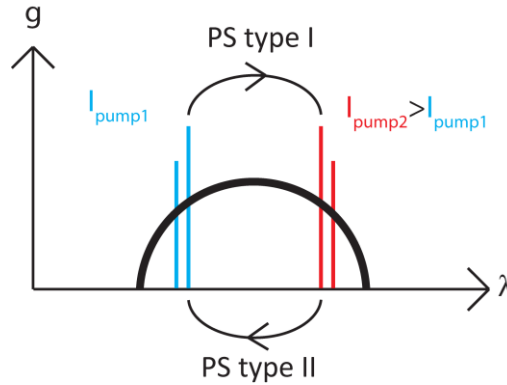

Figure 2.5 Sketch of spectral gain as a function of wavelength (black) together with the (very close to each other) polarization modes of the fundamental transverse mode (vertical lines) at different pump current values I_{pump1} (blue) and I_{pump2} (red), thus illustrating a polarization switch type I from the dominant higher wavelength to the shorter wavelength represented by the longer red and blue line, respectively. Together with the PS type II with a switch vice versa.

The polarization switching (PS) phenomenon can be classified into two different types namely PS type I which means that the switch occurs from a polarization mode with a shorter emission wavelength to a polarization mode with a longer emission wavelength when increasing current or temperature, respectively. And the opposite case is called a PS type II [35], both PS type I and type II are depicted schematically in Figure 2.5. The PS type I is found more frequently than PS type II [36] and can be followed by a PS type II at higher current [37]. The separation in frequency of the illustrated polarization modes are in the range of a few GHz, is caused by birefringence and can be experimentally determined by measuring highly resolved optical spectra [12].

To conclude this chapter, in the following a comparison of the fundamental properties of VCSELs is presented in a table together with the corresponding properties of LEDs and EELs, thus illustrating the potential of VCSELs with respect to applications given at the end.

VCSELs vs EEL
Low threshold current
Slowly divergent circular beam
Wafer-level testing, low cost
Simplified mounting and packaging
Two-dimensional arrays

Table 2.1 Summarized advantages of VCSELs over EELs.

At least these properties shown in Table 2.1 enable VCSELs to be appropriate candidates for applications in single-fiber and parallel optical data communication, furthermore in sensing applications as e.g. in optical mice and in laser printing devices.

The significant success of VCSELs especially in communication application, based on reliability, performance, high production volumes and supplies stability provides a foundation for new communication applications and other emerging markets. For most of these applications a stable polarization of the emitted light is necessary also under the aspects of additionally utilized polarization selective elements, necessitating further investigations on the polarization features of VCSELs.

3. Stokes formalism

The polarization of light, which is one of light´s basic properties beside its intensity, wavelength and coherence, has its origin in the vectorial wave character of the light. In this chapter we present a mathematical formalism completely describing polarized light. Furthermore, we illustrate different states of polarization in terms of that formalism. At the end of this chapter an introduction to a technique capable of measuring the polarization states of light will be given.

A comprehensive mathematical expression in terms of four parameters has been derived in 1852 by Sir George Gabriel Stokes [21]. These four Stokes polarization parameters (SPPs) are directly measurable quantities, describing beside fully polarized light for the first time partially polarized light and additionally unpolarized light. Within this formalism the Fresnel-Arago interference laws[3] could have been written and understood on the basis of wave theory for the first time. SPPs provide a powerful tool to investigate and understand the polarization states of light as well as its interaction with matter.

At the beginning of the 19th century, many scientists proposed a new theory of light in analogy to the wave concept of classical mechanics. One of the prime example experiments to demonstrate the wave character of light is the double slit experiment, first realized by Thomas Young in about 1800, where the intensity modulation of light, passing a double slit, is explained by interfering waves with their starting point on both slits. Young´s work provided the first crucial step in the development and acceptance of wave theory of light. In 1818, fundamental investigations on Young´s interference experiment have been carried out by Fresnel and Arago using polarized light. Comprehensive historical notes regarding the investigations on polarization of light can be found in [38] [39] [40]. In conclusion from these results, light consists of two orthogonally linearly polarized electric field components such as:

$$E_x(z,t) = E_{0x}\cos[\omega t - \kappa z + \delta_x] \tag{3.1}$$

$$E_y(z,t) = E_{0y}\cos[\omega t - \kappa z + \delta_y]. \tag{3.2}$$

Where E_{0x} and E_{0y} are the maximum amplitudes and $\omega t - \kappa z$ is the propagator of the electric field. The propagating direction is represented by z, time is represents by t, whereas x and y

---

[3]   1) Two waves linearly polarized in the same plane can interfere.

2) Two waves linearly polarized with perpendicular polarizations cannot interfere.

3) Two waves linearly polarized with perpendicular polarizations, if derived from perpendicular components of unpolarized light and subsequently brought into the same plane, cannot interfere.

4) Two waves linearly polarized with perpendicular polarizations, if derived from the same linearly polarized wave and subsequently brought into the same plane, can interfere.

(with $x \perp y$) span a transverse plane orthogonal to the direction of propagation and δ_x and δ_y represent the respective phases. These two components $E_x(z, t)$ and $E_y(z, t)$ result via superposition in a vector $E(x, y, z, t)$, describing a locus of points in space. It can be shown, that these points obey the equation of an ellipse that can be derived from $E_x(z, t)$ and $E_y(z, t)$ such that one takes into account a point in space, resulting in a fixed value of z as well as t. Therefore, one can rewrite (3.1) and (3.2) utilizing that $\tau = \omega t - \kappa z$ and $\cos(\tau + \delta_x) = \cos\tau \, \cos\delta_x - \sin\tau \, \sin\delta_x$ such as

$$\frac{E_x(t)}{E_{0x}} = \cos\tau \, \cos\delta_x - \sin\tau \, \sin\delta_x \tag{3.3}$$

$$\frac{E_y(t)}{E_{0y}} = \cos\tau \, \cos\delta_y - \sin\tau \, \sin\delta_y. \tag{3.4}$$

Hence,

$$\frac{E_x(t)}{E_{0x}} \sin\delta_y - \frac{E_y(t)}{E_{0y}} \sin\delta_x = \cos\tau \, \sin(\delta_y - \delta_x) \tag{3.5}$$

$$\frac{E_x(t)}{E_{0x}} \cos\delta_y - \frac{E_y(t)}{E_{0y}} \cos\delta_x = \sin\tau \, \sin(\delta_y - \delta_x). \tag{3.6}$$

Squaring and adding equation (3.5) and (3.6) and using $\delta = \delta_y - \delta_x$ results in an equation of an ellipse such as:

$$\frac{E_x^2(t)}{E_{0x}^2} + \frac{E_y^2(t)}{E_{0y}^2} - \frac{2E_x(t)E_y(t)}{E_{0x}E_{0y}} \cos\delta = \sin^2\delta. \tag{3.7}$$

The characteristic travel of the tip of the vector $E(x, y, z, t) = \vec{E}(t)$ representing the electric field amplitude as a function of space and time is spoken of as *optical polarization* (see Figure 3.1). Hence, (3.7) is called the *polarization ellipse*.

The mathematical relation connecting the parameters of the polarization ellipse E_{0x}, E_{0y} and δ with the in Figure 3.1 schematically depicted angles of rotation ψ and ellipticity χ terms as follows

$$\tan 2\psi = \frac{2E_{0x}E_{0y} \cos\delta}{E_{0x}^2 - E_{0y}^2} \tag{3.8}$$

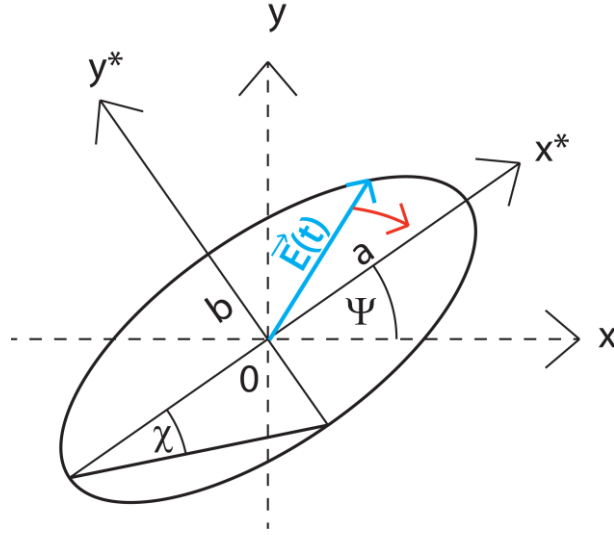$$\sin 2\chi = \frac{2E_{0x}E_{0y} \sin\delta}{E_{0x}^2 + E_{0y}^2}. \tag{3.9}$$

Figure 3.1 Schematic drawing of the polarization ellipse defined by the propagation of the tip of the electric field vector $\vec{E}(t)$ (blue) illustrating the rotation angle of the ellipse ψ together with the angle of ellipticity χ.

In order to represent (3.7) in terms of the observables of the optical field, we must take an average over the time of observation. Because this is a long period of time, relative to the time for a single oscillation (only 10^{-15}s), it can be taken to be infinite. However, in view of the periodicity of $E_x(t)$ and $E_y(t)$, we need average (3.7) only over a single period of oscillation. The time average is represented by the symbol $\langle ... \rangle$, hence we write (3.7) as

$$\frac{\langle E_x^2(t) \rangle}{E_{0x}^2} + \frac{\langle E_y^2(t) \rangle}{E_{0y}^2} - \frac{2\langle E_x(t)E_y(t) \rangle}{E_{0x}E_{0y}} \cos \delta = \sin^2 \delta. \tag{3.10}$$

Here the time average terms

$$\langle E_x(t)E_y(t) \rangle = \lim_{T \to \infty} \frac{1}{T} \int_0^T E_x(t)E_y(t)\, dt. \tag{3.11}$$

When the period of time T relative to the time for a single oscillation is large, it can be taken as infinity. Regarding the periodicity of $E_x(t)$ and $E_y(t)$ it is sufficient to average over a single periode of oscillation only. Furthermore, we multiply (3.10) by $4\, E_{0x}^2 E_{0y}^2$, which results in

$$4\, E_{0y}^2 \langle E_x^2(t) \rangle + 4\, E_{0x}^2 \langle E_y^2(t) \rangle - 8\, E_{0x}E_{0y}\langle E_x(t)E_y(t) \rangle \cos \delta = (2\, E_{0x}E_{0y} \sin \delta)^2 \tag{3.12}$$

The average values of (3.12) are found by using (3.11) and term

$$\langle E_x^2(t) \rangle = \frac{1}{2} E_{0x}^2 \tag{3.13}$$

$$\langle E_y^2(t) \rangle = \frac{1}{2} E_{0y}^2 \tag{3.14}$$

$$\langle E_x(t)E_y(t)\rangle = \frac{1}{2}E_{0x}E_{0y}\cos\delta. \tag{3.15}$$

Substituting (3.13), (3.14), (3.15) into (3.12) yields

$$2E_{0x}^2 E_{0y}^2 + 2E_{0x}^2 E_{0y}^2 - (2E_{0x}E_{0y}\cos\delta)^2 = (2E_{0x}E_{0y}\sin\delta)^2. \tag{3.16}$$

By adding and subtracting the term $E_{0x}^4 + E_{0y}^4$ to the left hand side of (3.16) we end up with perfect squares

$$(E_{0x}^2 + E_{0y}^2)^2 - (E_{0x}^2 - E_{0y}^2)^2 - (2E_{0x}E_{0y}\cos\delta)^2 = (2E_{0x}E_{0y}\sin\delta)^2. \tag{3.17}$$

Now we reorder equation (3.17)

$$\left(E_{0x}^2 + E_{0y}^2\right)^2 = \left(E_{0x}^2 - E_{0y}^2\right)^2 + \left(2E_{0x}E_{0y}\cos\delta\right)^2 + \left(2E_{0x}E_{0y}\sin\delta\right)^2 \tag{3.18}$$

and write the quantities inside the parenthesis as

$$S_0 = E_{0x}^2 + E_{0y}^2 \tag{3.19}$$
$$S_1 = E_{0x}^2 - E_{0y}^2 \tag{3.20}$$
$$S_2 = 2E_{0x}E_{0y}\cos\delta \tag{3.21}$$
$$S_3 = 2E_{0x}E_{0y}\sin\delta. \tag{3.22}$$

These four quantities defined by (3.19) - (3.22) are the *Stokes polarization parameters* (SPPs) S_0, S_1, S_2 and S_3 for a plane wave. Using that the intensity I is proportional to the square of the electric field vector E the SPPs can also be written as

$$S_0 = I_x + I_y \tag{3.23}$$
$$S_1 = I_x - I_y \tag{3.24}$$
$$S_2 = I_{45°} - I_{-45°} \tag{3.25}$$
$$S_3 = I_{RCP} - I_{LCP}. \tag{3.26}$$

From this notation it is clear, that the first Stokes polarization parameter S_0 is the total intensity of the light. The parameter S_1 describes the amount of linear horizontal or vertical polarization, the parameter S_2 describes the amount of linear +45° or -45° polarization and the parameter S_3 describes the amount of right circular polarization (RCP) and left circular polarization (LCP) contained within the beam.

Furthermore, they are simply the observables of the polarization ellipse and, hence the optical field. To obtain the Stokes polarization parameters of an optical beam, one must always take a time average of the polarization ellipse at least over a single periode of oscillation as it has been shown above. This time-averaging process can be formally bypassed by representing the (real) optical amplitudes (3.1) and (3.2) in terms of complex amplitudes,

$$E_x(t) = E_{0x} \exp[i(\omega t + \delta_x)] = \widetilde{E}_{0x} \exp(i\omega t) \qquad (3.27)$$

$$E_y(t) = E_{0y} \exp[i(\omega t + \delta_y)] = \widetilde{E}_{0y} \exp(i\omega t). \qquad (3.28)$$

Where $\widetilde{E}_{0x} = E_{0x} \exp(i\delta_x)$ and $\widetilde{E}_{0y} = E_{0y} \exp(i\delta_y)$ are complex amplitudes. The Stokes polarization parameters for a plane wave are now obtained from the formulae such as

$$S_0 = E_x E_x^* + E_y E_y^* \qquad (3.29)$$
$$S_1 = E_x E_x^* - E_y E_y^* \qquad (3.30)$$
$$S_2 = E_x E_y^* + E_y E_x^* \qquad (3.31)$$
$$S_3 = i(E_x E_y^* + E_y E_x^*). \qquad (3.32)$$

The following schematic drawings illustrate different states of polarization and exemplarily explain the definition of the four SPPs. In addition, with a clear definition of right-handed and left-handed circularly polarized light. The schematic drawings of states of polarization with exclusive contributions of S_1, S_2 and S_3 are depicted in Figure 3.2. Additionally, the sign of S_1, S_2 and S_3 is taken into account, such that the states of polarization denoted by positive values are on top, whereas the negative values are depicted below. In Figure 3.2(top left) an emitting source is depicted by a yellow cross within a circle with the same color. The direction of propagation points into the positive z-direction, supported by the coordinate axis illustrated as an inset. The sketch of the emitting source is not further depicted in the other graphs, for the sake of clarity. The projection of the electric field components on the x-y-plane at an arbitrary value of z is represented by green arrows. Both, the linear horizontal (top) and the linear vertical (bottom) polarization are clearly visible and associated with the in the table below depicted corresponding SPP S_1=+1 and S_1=-1, respectively.

The visualization of the SPP S_2 is depicted in Figure 3.2(middle), here in addition with two orthogonal electric field components E_x and E_y represented by blue and red lines, respectively. The resulting oscillation of the electrical field is consequently represented by a black line. Furthermore, the phase difference, showing up for the first time for S_2=-1 with a value of $\delta = \pi$, is illustrated by an orange dash especially labeled in the graph. This phase difference causes a rotation of the resulting electric field (black line, bottom) about 90°, which means that, a change of sign in this SPP S_2 represents a change of the orientation about 90° as it has already been observed in the case of S_1.

Figure 3.2(right) depicts the right-handed (top) and left-handed (bottom) circularly polarized state of light. The traditional terminology tells that the polarization is right-handed, when looking into the direction from which the light is coming (negative z-direction); the end point of the electric field vector (black line) describes a circle (or in general an ellipse) in clockwise direction (cf. Figure 3.2(top right)). The opposite can be observed in Figure 3.2(bottom right)), here left-handed circularly polarized light with S_3=-1 is schematically depicted.
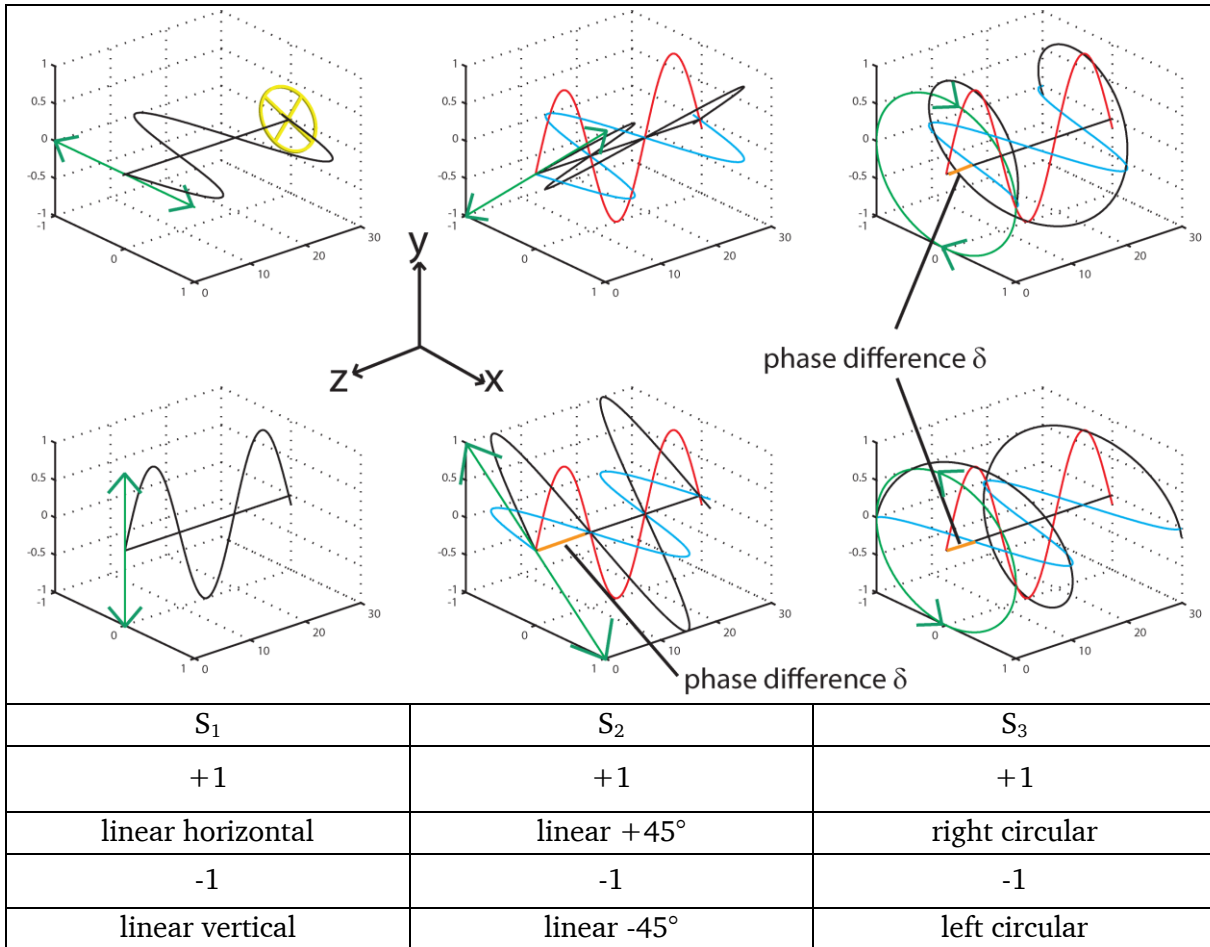
Figure 3.2 A schematic representation of states of polarization with exclusive contributions of S_1 (left), S_2 (middle) and S_3 (right) with a positive sign (top) as well as a negative sign (bottom). The orthogonal electric field components E_x (blue line) and E_y (red line) together with the phase difference δ (orange stroke) as well as the projection of the resulting electric field oscillation (black line) on the x-y-plane (green) are visible.

Beside fully polarized light, partially and unpolarized states of light can be formulated as well. Substituting (3.19) - (3.22) into (3.18) results in the following equation which is valid for fully polarized light only

$$(S_0)^2 = (S_1)^2 + (S_2)^2 + (S_3)^2. \tag{3.33}$$

If we now have partially polarized light, we see that (3.19) - (3.22) are still valid for very short time intervals, since the phase and amplitude fluctuate slowly. Using Schwarz´s inequality, one can show that for any state of polarized light the Stokes polarization parameters always satisfy the following relation

$$(S_0)^2 \geq (S_1)^2 + (S_2)^2 + (S_3)^2. \tag{3.34}$$

Here, the equal sign applies when we have completely polarized light and the inequality when we have partially polarized light and unpolarized light.

In addition one can express the degree of polarization (DOP) for any state of polarization. By definition

$$ \text{DOP} = \frac{I_{\text{pol}}}{I_{\text{total}}} = \frac{(S_1^2 + S_2^2 + S_3^2)^{\frac{1}{2}}}{S_0} \qquad\qquad 0 \leq \text{DOP} \leq 1. \qquad (3.35) $$

Where I_{pol} is the intensity of the sum of the polarization components and I_{total} is the total intensity of the beam. The value DOP=1 corresponds to completely polarized light, DOP=0 corresponds to unpolarized light and 0<DOP<1 corresponds to any partially polarized state of light.

The Stokes polarization parameters S_0, S_1, S_2 and S_3 can be merged to a column matrix such that

$$ \vec{S} = \begin{pmatrix} S_0 \\ S_1 \\ S_2 \\ S_3 \end{pmatrix} \qquad\qquad (3.36) $$

This column matrix $\vec{S}$ is called the *Stokes vector* and can be illustrated by utilizing the Poincaré sphere as it is depicted in
Figure 3.3. Here, the Stokes polarization parameters S_1, S_2 and S_3 span the orthogonal space in which the Poincaré sphere exists. Every state of polarization is described by a vector starting at the origin at (0,0,0) pointing on the surface of this sphere.
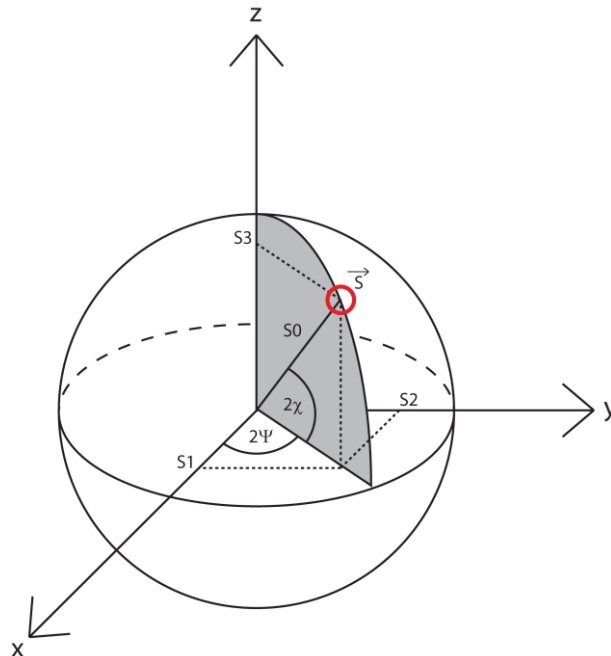

Figure 3.3 Poincaré representation of fully polarized light, represented by the Stokes vector $\vec{S}$, pointing to a point on the surface of the sphere marked with a red circle. The total intensity I_{total} is represented by the length S_0 of the Stokes vector $\vec{S}$, whereas the other Stokes polarization parameters S_1, S_2 and S_3 are represented by projections on the x-, y- and z-axis, respectively. Furthermore, the polarization ellipse parameters ψ and χ are clearly visible, denoting the angles of the spherical coordinates.

Furthermore, the SPPs S_0, S_1, S_2 and S_3 can be related to the polarization ellipse parameters ψ and χ combining (3.8) and (3.9) with (3.19) - (3.22), thus resulting in

$$\tan 2\psi = \frac{2E_{0x}E_{0y}\cos\delta}{E_{0x}^2 - E_{0y}^2} = \frac{S_2}{S_1} \tag{3.37}$$

$$\sin 2\chi = \frac{2E_{0x}E_{0y}\sin\delta}{E_{0x}^2 + E_{0y}^2} = \frac{S_3}{S_0}. \tag{3.38}$$

In addition to the compact illustration of the SPPs on the basis of the Poincaré sphere, in the following they will be connected with another fundamental property of light, namely its coherence. Moreover, a relation to the Pauli Spin matrices will be given, just to demonstrate the powerfulness of the Stokes formalism.

We start with the definition of the polarization or coherency matrix J [41]

$$J = \begin{bmatrix} J_{xx} & J_{xy} \\ J_{yx} & J_{yy} \end{bmatrix} = \begin{bmatrix} \langle E_x^*(t)E_x(t) \rangle & \langle E_x^*(t)E_y(t) \rangle \\ \langle E_y^*(t)E_x(t) \rangle & \langle E_y^*(t)E_y(t) \rangle \end{bmatrix} \tag{3.39}$$

which characterizes the correlation properties of the electric field represented by two orthogonal components

$$E_x(t) = E_{0x}\exp[i(\omega t + \delta_x)] \tag{3.40}$$

$$E_y(t) = E_{0y}\exp[i(\omega t + \delta_y)]. \tag{3.41}$$

Here, the asterisk denotes the complex conjugate. This matrix J is an equal-time correlation matrix [42] [43]. Its diagonal elements $\langle E_x^*(t)E_x(t) \rangle$ and $\langle E_y^*(t)E_y(t) \rangle$ are averages of the intensities associated with each of the two components. The following equations recall the definition of the SPPs in terms of the complex electric field together with the relation to the elements of the coherency matrix J, namely J_{xx}, J_{xy}, J_{yx} and J_{yy} such as

$$S_0 = E_xE_x^* + E_yE_y^* = J_{xx} + J_{yy} \tag{3.42}$$

$$S_1 = E_xE_x^* - E_yE_y^* = J_{xx} - J_{yy} \tag{3.43}$$

$$S_2 = E_xE_y^* + E_yE_x^* = J_{xy} + J_{yx} \tag{3.44}$$

$$S_3 = i(E_xE_y^* + E_yE_x^*) = i(J_{xy} - J_{yx}). \tag{3.45}$$

Furthermore, the degree of polarization can be expressed in terms of the coherency matrix J as well

$$\text{DOP} = \sqrt{1 - \frac{4\det(J)}{(\text{Tr}(J))^2}} \tag{3.46}$$

where $\text{Tr}(J)$ is the trace of the coherency matrix J ($\text{Tr}(J) = J_{xx} + J_{yy}$) and $\det(J) = J_{xx}J_{yy} - J_{yx}J_{xy}$ means the determinant of J. Finally, there is a remarkable relation between the SPPs S_0, S_1, S_2 and S_3 and the entries of the coherency matrix J such as

$$J_{xx} = \frac{S_0 + S_1}{2} \tag{3.47}$$

$$J_{yy} = \frac{S_0 - S_1}{2} \tag{3.48}$$

$$J_{xy} = \frac{S_2 - iS_3}{2} \tag{3.49}$$

$$J_{yx} = \frac{S_2 + iS_3}{2}. \tag{3.50}$$

Hence, we can express these equations in matrix form as

$$J = \begin{bmatrix} J_{xx} & J_{xy} \\ J_{yx} & J_{yy} \end{bmatrix} = \frac{1}{2} \begin{bmatrix} S_0 + S_1 & S_2 - iS_3 \\ S_2 + iS_3 & S_0 - S_1 \end{bmatrix}. \tag{3.51}$$

One can easily decompose (3.51) into 2x2 matrices such that

$$J = \frac{1}{2} \sum_{i=0}^{3} \sigma_i S_i. \tag{3.52}$$

Where

$$\sigma_0 = \begin{bmatrix} 1 & 0 \\ 0 & 1 \end{bmatrix} \qquad \sigma_1 = \begin{bmatrix} 1 & 0 \\ 0 & -1 \end{bmatrix} \tag{3.53} \tag{3.54}$$

$$\sigma_2 = \begin{bmatrix} 0 & 1 \\ 1 & 0 \end{bmatrix} \qquad \sigma_3 = \begin{bmatrix} 0 & -i \\ i & 0 \end{bmatrix} \tag{3.55} \tag{3.56}$$

The remarkable fact about this decomposition is that the σ_i with i=0,1,2,3 matrices are the Pauli spin matrices of quantum mechanics. This connection between the coherency matrix J, the Stokes polarization parameters S_0, S_1, S_2 and S_3, and the Pauli Spin matrices σ_0, σ_1, σ_2 and σ_3 appears to have been first pointed out by U. Fano in 1954 [44]. Furthermore, the Spin matrices have been introduced to quantum mechanics by Wolfgang Pauli in order to describe the behavior of the spin of the electron, a particle. This connection of the SPPs with the Pauli spin matrices as well as the coherency matrix demonstrates the comprehensive properties of the Stokes formalism. A unified treatment of the algebra of SPPs and the coherency matrix

can be found in [45], whereas a formalism connecting the Stokes vector with the polarization of lasers is given in [46].

The four Stokes polarization parameters S_0, S_1 S_2 and S_3 can be measured as follows. First, a "classical" measurement technique of these parameters is presented, whereas in the second part a method using a rotating quarter-wave plate in combination with a fixed linear polarizer is explained in more detail, because this is the method of choice and is applied for every SPP measurements within this thesis.

It can be shown, that the intensity of a beam of light passing a combination of a quarter-wave plate and a linear polarizer is given by

$$I(\theta, \varphi) = \frac{1}{2}[S_0 + S_1 \cos 2\theta + S_2 \cos \varphi \sin 2\theta + S_3 \sin \varphi \cos 2\theta] \tag{3.57}$$

where θ is an angle between the horizontal axis and the transmission axis of the linear polarizer and φ is the phase retardation between the vertical and the horizontal electric field component. This equation is Stokes´ famous intensity formula for measuring the four SPPs and reflects that S_0, S_1, S_2 and S_3 are directly accessible quantities.
The SPPs can be determined by measuring four intensities $I(\theta, \varphi)$ with the following well-selected combination of θ and φ such that (3.57) reduces to

$$I(\theta = 0, \varphi = 0) = \frac{1}{2}[S_0 + S_1] \tag{3.58}$$

$$I\left(\theta = \frac{\pi}{4}, \varphi = 0\right) = \frac{1}{2}[S_0 + S_2] \tag{3.59}$$

$$I\left(\theta = \frac{\pi}{2}, \varphi = 0\right) = \frac{1}{2}[S_0 - S_1] \tag{3.60}$$

$$I\left(\theta = \frac{\pi}{4}, \varphi = \frac{\pi}{2}\right) = \frac{1}{2}[S_0 + S_3] \tag{3.61}$$

where a phase retardation of $\varphi = 0$ means that the retarder is removed, except for the last measurement. Here, a retardation of $\varphi = \frac{\pi}{2}$ is required to obtain a formula containing S_0 and S_3 only. Solving (3.58) - (3.61) for the SPPs, we obtain

$$S_0 = I(0,0) + I\left(\frac{\pi}{2}, 0\right) \tag{3.62}$$

$$S_1 = I(0,0) - I\left(\frac{\pi}{2}, 0\right) \tag{3.63}$$

$$S_2 = 2I\left(\frac{\pi}{4}, 0\right) - I(0,0) - I\left(\frac{\pi}{2}, 0\right) \tag{3.64}$$

$$S_3 = 2I\left(\frac{\pi}{4}, \frac{\pi}{2}\right) - I(0,0) - I\left(\frac{\pi}{2}, 0\right) \tag{3.65}$$

To conclude this section, equations (3.62) - (3.65) clearly show that it is possible to directly measure the four SPPs S_0, S_1, S_2 and S_3 by measuring the intensities given in (3.58) - (3.61) as it has been done in [47], where even spatially resolved Stokes polarization parameters have been measured. However, within this method it is necessary to measure with and without a quarter-wave plate; this manipulates the intensity measurements, due to the non-negligible

absorption of the quarter-wave plate. To circumvent this perturbation, a more reliable technique is presented in the following section, where the quarter-wave plate is always in the measurement path and will be rotated, whereas the linear polarizer is fixed. This in combination with the fact, that the technique can be automated, result in easier and faster measurements. Detailed description of realizations of this technique can be found in [39], [48] and [49]; in [50] additionally with experimental examples and possible sources of errors. Further experimental alternative methods are presented in [51] in terms of the null intensity method. The use of a rotating linear polarizer to determine the SPPs can be found in [39]. A method described in [52] is based on the recording of only one single-shot image to obtain the SPPs characteristic. However, this method is inappropriate to perform spatially resolved measurements.

The underlining theory of the rotating quarter-wave plate technique is briefly explained in the following using the 4x4 Müller matrices $\overline{\overline{M}}$ which describe the effect of polarizing elements on an incident Stokes vector $\vec{S}_{in}$, thus resulting in a state of polarization given by $\vec{S}_{out}$ and terms

$$\vec{S}_{out} = \overline{\overline{M}} \, \vec{S}_{in}. \tag{3.66}$$

The effect of a linear polarizer on unpolarized light is given in the following to illustrate the combination of the Stokes and the Müller formalism. An unpolarized state of light is represented by a Stokes vector such as

$$\vec{S}_{unp} = (S_0 \quad S_1 \quad S_2 \quad S_3)^T = (1 \quad 0 \quad 0 \quad 0)^T \tag{3.67}$$

the $(...)^T$ denotes the transposed Stokes vector. The 4x4 Müller matrix of a linear polarizer $\overline{\overline{M_{LP}}}(\alpha)$ where α denotes the angle between the transmission axis and the horizontal axis as it is schematically depicted in Figure 3.4 is written as

$$\overline{\overline{M_{LP}}}(\alpha) = \begin{pmatrix} 1 & \cos(2\alpha) & \sin(2\alpha) & 0 \\ \cos(2\alpha) & \cos^2(2\alpha) & \cos(2\alpha)\sin(2\alpha) & 0 \\ \sin(2\alpha) & \cos(2\alpha)\sin(2\alpha) & \sin^2(2\alpha) & 0 \\ 0 & 0 & 0 & 0 \end{pmatrix}. \tag{3.68}$$

The formula to determine the Stokes vector $\vec{S}$ of an unpolarized beam of light $\vec{S}_{unp}$ passing a linear polarizer terms
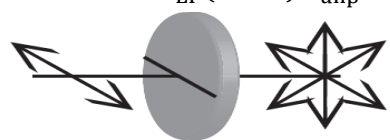
$$\vec{S} \qquad = \overline{\overline{M_{LP}}}(\alpha = 0) \, \vec{S}_{unp}. \tag{3.69}$$

Figure 3.4 Schematic representation of formula (3.69) illustrating unpolarized light (right), passing a linear polarizer with its transmission axis aligned with the horizontal axis (middle) and the resulting linearly polarized state of light (left)

By fixing the angle α equal to zero, thus simplifies the 4x4 Müller matrix $\overline{\overline{M_{LP}}}(\alpha = 0)$ and the matrix calculation in (3.69) as follows

$$\begin{pmatrix} 1 \\ 1 \\ 0 \\ 0 \end{pmatrix} = \begin{pmatrix} 1 & 1 & 0 & 0 \\ 1 & 1 & 0 & 0 \\ 0 & 0 & 0 & 0 \\ 0 & 0 & 0 & 0 \end{pmatrix} \begin{pmatrix} 1 \\ 0 \\ 0 \\ 0 \end{pmatrix}. \tag{3.70}$$

Where $\vec{S} = (1 \quad 1 \quad 0 \quad 0)^T$ represents a linearly horizontally polarized state of light (with $S_1 = 1$), as expected in this example.

In the following, the influence of a revolvable quarter-wave plate in combination with a fixed linear polarizer with their Müller matrices $\overline{\overline{M_{QWP}}}(\beta, \delta)$ and $\overline{\overline{M_{LP}}}(\alpha)$ is mathematically explained in detail. The arguments of the different Müller matrices, β, δ and α denote the angle of the quarter-wave plate with respect to the horizontal axis, its phase retardation and the angle between the linear polarizer´s transmission axis and the horizontal axis, respectively as it is visible from Figure 3.5. The mathematical equation (3.71) directly connecting the mathematical terms is depicted above and terms

$$\vec{S}` = \overline{\overline{M_{LP}}}(\alpha)\, \overline{\overline{M_{QWP}}}(\beta, \delta)\, \vec{S}. \tag{3.71}$$
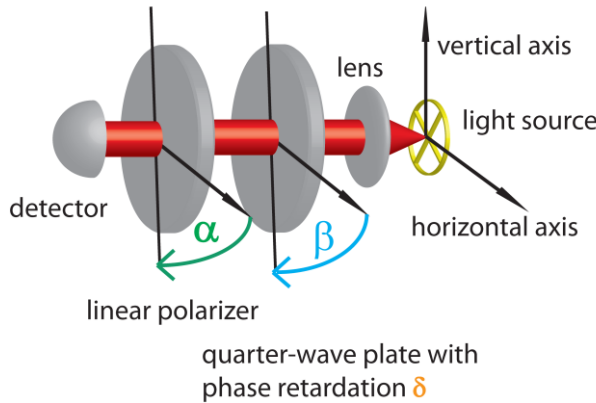

Figure 3.5 Schematic drawing of the functional principle of the method of the revolvable quarter-wave plate in combination with a fixed linear polarizer together with a light source (right) and a detector (left)

The most general mathematical expressions for the Müller matrices are given by

$$\begin{pmatrix} S_0`(\alpha, \beta, \delta) \\ S_1`(\alpha, \beta, \delta) \\ S_2`(\alpha, \beta, \delta) \\ S_3`(\alpha, \beta, \delta) \end{pmatrix} = \begin{pmatrix} 1 & \cos(2\alpha) & \sin(2\alpha) & 0 \\ \cos(2\alpha) & \cos^2(2\alpha) & \cos(2\alpha)\sin(2\alpha) & 0 \\ \sin(2\alpha) & \cos(2\alpha)\sin(2\alpha) & \sin^2(2\alpha) & 0 \\ 0 & 0 & 0 & 0 \end{pmatrix} \tag{3.72}$$

$$\times \begin{pmatrix} 1 & 0 & 0 & 0 \\ 0 & \cos^2(2\beta) + \cos(\delta)\sin^2(2\beta) & -\cos(2\beta)\sin(2\beta)(\cos(\delta)-1) & \sin(2\beta)\sin(\delta) \\ 0 & -\cos(2\beta)\sin(2\beta)(\cos(\delta)-1) & \cos(\delta)\cos^2(2\beta) + \sin^2(2\beta) & -\cos(2\beta)\sin(\delta) \\ 0 & -\sin(2\beta)\sin(\delta) & \cos(2\beta)\sin(\delta) & \cos(\delta) \end{pmatrix} \begin{pmatrix} S_0 \\ S_1 \\ S_2 \\ S_3 \end{pmatrix}$$

Multiplying the Müller matrix of the quarter-wave plate $\overline{\overline{M_{QWP}}}(\beta, \delta)$ with the Stokes vector $\vec{S}$ of interest leads to

$$
\begin{pmatrix} S_0{}^{`}(\alpha, \beta, \delta) \\ S_1{}^{`}(\alpha, \beta, \delta) \\ S_2{}^{`}(\alpha, \beta, \delta) \\ S_3{}^{`}(\alpha, \beta, \delta) \end{pmatrix} = \begin{pmatrix} 1 & \cos(2\alpha) & \sin(2\alpha) & 0 \\ \cos(2\alpha) & \cos^2(2\alpha) & \cos(2\alpha)\sin(2\alpha) & 0 \\ \sin(2\alpha) & \cos(2\alpha)\sin(2\alpha) & \sin^2(2\alpha) & 0 \\ 0 & 0 & 0 & 0 \end{pmatrix}
\tag{3.73}
$$

$$
\times \begin{pmatrix} S_0 \\ S_1\left(\cos^2(2\beta) + \cos(\delta)\sin^2(2\beta)\right) - S_2\cos(2\beta)\sin(2\beta)(\cos(\delta) - 1) + S_3\sin(2\beta)\sin(\delta) \\ -S_1\cos(2\beta)\sin(2\beta)(\cos(\delta) - 1) + S_2\left(\cos(\delta)\cos^2(2\beta) + \sin^2(2\beta)\right) - S_3\cos(2\beta)\sin(\delta) \\ -S_1\sin(2\beta)\sin(\delta) + S_2\cos(2\beta)\sin(\delta) + S_3\cos(\delta) \end{pmatrix}.
$$

After further calculations one comes to the following result, giving the explicit expression for the first SPP $S_0{}^{`}$ of $\vec{S}$ which is equivalent to the measured intensity of the incident beam, passing a combination of a quarter-wave plate and a linear polarizer

$$
\begin{aligned}
S_0{}^{`}(\alpha, \beta, \delta) = \; & S_0 \\
& + S_1(\cos(2\alpha)\cos^2(2\beta) + \cos(\delta)\sin^2(2\beta) - \cos^2(2\beta)\sin(2\alpha)\sin(2\beta)(\cos(\delta) - 1) \\
& + S_2(\sin(2\alpha)(\cos^2(\beta) + \sin^2(2\beta) - \cos(2\alpha)\cos(2\beta)\sin(2\beta)(\cos(\delta) - 1) \\
& + S_3(\cos(2\alpha)\sin(2\beta)\sin(\delta) - \cos(2\beta)\sin(2\alpha)\sin(\delta)).
\end{aligned}
\tag{3.74}
$$

Now the desired SPPs S_0, S_1, S_2 and S_3 can be determined by a multi-parameter fit[4] to the measured intensity $S_0{}^{`}(\alpha, \beta, \delta)$. Keeping α and δ constant at values of $0°$ and $\frac{\pi}{2}$ respectively, hence (3.74) reduces to

$$
S_0{}^{`}(\beta) = 1/2(S_0 + S_1\cos^2(2\beta) + S_2\cos(2\beta)\sin(2\beta) + S_3\sin(2\beta)).
\tag{3.75}
$$

In conclusion, we introduced the Stokes polarization parameters which are four measurable quantities that describe any state of polarization. Furthermore, within the Stokes formalism one can distinguish between completely polarized, partially polarized as well as unpolarized states of light, quantified by the degree of polarization. Furthermore, we explained the theoretical basis of the method of the rotating quarter-wave plate, which enables one to determine the four Stokes polarization parameters of an arbitrary source.

---

[4] A discussion on the convergences of the multi-parameter fit can be found in [48] and [50] and a proof of correctness of this method will be additionally given in the next chapter.

4. Stokes polarization parameters integrated over space, time and wavelength

After the introduction of VCSELs in chapter 2 and the powerful Stokes formalism in the previous chapter, now in the present chapter first experimental results of injection current dependent Stokes polarization parameter (SPP(I_{pump})) measurements on VCSELs are presented and discussed. First, a detailed overview of the experimental setup utilized for measuring the SPPs is given. Then, fundamental characterizations of the utilized optical components, such as their configurations and adjustments, including their orientation with respect to the crystalline axis of the VCSELs are pointed out. At the end of the chapter, experimental results on the polarization behavior of VCSELs with different oxide aperture diameters are shown. Finally, the behavior of the observed SPPs is discussed.

As it was explained in the previous chapter a robust and reliable experimental technique to obtain the SPPs is to use a combination of a revolvable quarter-wave plate and a fixed linear polarizer. A schematic drawing of the experimental setup is depicted in Figure 4.1(left), including the VCSEL together with its crystalline axes [-110] and [110] as well as a collimation lens. The collimated beam passes a combination of a revolvable quarter-wave plate and a fixed linear polarizer. Both, the fast axis of the quarter-wave plate as well as the transmission axis of the linear polarizer are in-line with the crystalline axis [110] of the investigated devices. When looking into the direction of the propagation of the beam, the rotation of the quarter-wave plate is performed clockwise as it is visible from Figure 4.1(left). Because of this alignment of the polarization selective components with respect to the VCSELs crystalline axis [-110] and [110] the SPPs $S_1 = -1$ and $S_1 = +1$ represent a linear horizontal and a linear vertical polarization, thus being in-line with the crystalline axis [-110] and [110], respectively. The SPPs S_0, S_1, S_2 and S_3 of the investigated optoelectronic devices were obtained within a multi-parameter fit to the experimentally obtained data (cf. Figure 4.1 inset) using the following mathematical expression

$$
\begin{aligned}
S_0{}^`(\alpha, \beta, \delta) = \ &S_0 \\
+S_1 &(\cos(2\alpha)\cos^2(2\beta) + \cos(\delta)\sin^2(2\beta) - \cos^2(2\beta)\sin(2a)\sin(2\beta)(\cos(\delta) - 1) \\
+S_2 &(\sin(2\alpha)(\cos^2(\beta) + \sin^2(2\beta) - \cos(2\alpha)\cos(2\beta)\sin(2\beta)(\cos(\delta) - 1) \\
+S_3 &(\cos(2\alpha)\sin(2\beta)\sin(\delta) - \cos(2\beta)\sin(2\alpha)\sin(\delta))
\end{aligned}
\tag{4.1}
$$

which has been derived in the previous chapter, representing the total intensity $S_0{}^`(\alpha, \beta, \delta)$ of an incident beam of light, passing a combination of a quarter-wave plate and a linear polarizer, as a function of

   i)   an offset angle $\alpha = 0$ of the linear polarizer,

   ii)   the rotation angle β of the revolvable quarter-wave plate relative to the transmission axis of the linear polarizer and

   iii) the wavelength dependent phase retardation δ.

In (4.1) α and δ are constant parameters due to the fixed linear polarizer and the constant phase retardation for one fixed wavelength, respectively. This results in a mathematical expression for the measurable total intensity of the detected beam $S_0{}^`(\beta)$ only as a function of the angle β of the quarter-wave plate such as

$$S_0`(\beta) = 1/2(S_0 + S_1 \cos^2(2\beta) + S_2 \cos(2\beta) \sin(2\beta) + S_3 \sin(2\beta)). \qquad (4.2)$$

Within a fit of $S_0`(\beta)$ to the experimentally obtained data (cf. Figure 4.1 inset) one is able to derive the four SPPs S_0, S_1, S_2 and S_3 together with the degree of polarization (DOP)

$$DOP = \sqrt{\frac{S_1{}^2 + S_2{}^2 + S_3{}^2}{S_0{}^2}} \qquad (4.3)$$

reflecting the ratio of the amount of polarized light to the total intensity.

In our experimental setup we used an achromatic quarter-wave plate (B.Halle Nachfolger), whose phase retardation δ is a function of the wavelength. The deviations of the phase retardation from $\pi/2$ in a spectral range between 600nm and 1200nm should be adapted to (4.1) to obtain the correct values of the SPPs. The usable spectral range of the linear polarizer (Glan-Thompson polarizing prism B.Halle Nachfolger) is between 300nm and 2700nm, which together with its extinction ratio, describing the ratio of the transmitted intensities of the wanted and unwanted orthogonally linearly polarized components of better than 10^6, makes these components reliable and feasible for polarization selective applications. This combination together with a commercial photo detection system, covering a spectral range from at least 400nm up to 1500nm, using two different types of photo detectors, makes this experimental setup utilizable to characterize the full polarization behavior in terms of the SPPs for any light source emitting in a spectral range between 600nm and 1200nm.
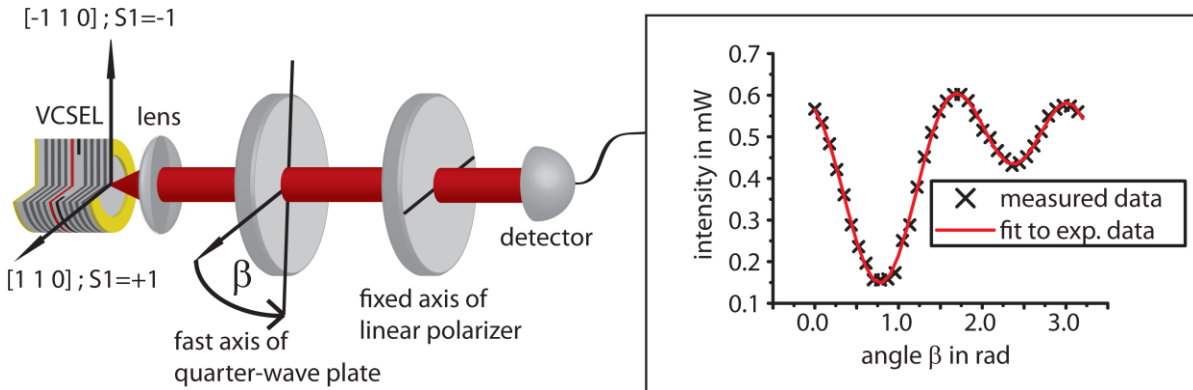

Figure 4.1 (left) Schematical drawing of the experimental setup showing the VCSEL with the crystalline axes [110] and [-110]. The emitted light is collimated by a lens, passes a combination of a quarter-wave plate with revolvable fast axis and a linear polarizer with fixed transmission axis and is finally detected by a photo detector. Right: a representative set of measured data (black cross) together with a fit to the measured data (red line) to extract the Stokes polarization parameters.

Before the experimental results of the injection current dependent SPPs of VCSELs are shown, one has to check the reliability of the utilized detection system composed of a quarter-wave plate, a linear polarizer and a photo detector. In detail, one has to determine the lowest intensity or signal to noise ratio (SNR) from which one gets the correct state of polarization of a pre-assigned fixed linear polarization, generated via an additionally utilized linear polarizer positioned between the lens and the revolvable quarter-wave plate. The SPPs S_0 (black star), S_1 (red plus), S_2 (blue cross) and S_3 (green circle) as a function of the attenuation in dB, according to different utilized neutral density filters, are depicted in Figure 4.2. This color-symbol representation of the SPPs will be used throughout this thesis apart from figures and graphs where another representation will be explicitly given. From this kind of representation of the results the coincidence of the states of polarization is hard to see. These polarization states are reflected by the SPPs with respect to different attenuation values in dB, well

reflected by a decreased value of S_0 representing the total intensity of the VCSEL´s emitted light.

For an easy comparison of the polarization states of light according to different total intensities S_0, one has to normalize the SPPs S_1, S_2 and S_3 with respect to S_0. Because of this normalization the SPPs S_1/S_0, S_2/S_0 and S_3/S_0 from now are called normalized Stokes polarization parameters (nSPPs) and are depicted in Figure 4.3a). Another fact is that all these nSPPs are now in the range between -1 and +1, however with the same representative color coded symbols of a red plus, a blue cross and a green circle, for S_1, S_2 and S_3, respectively. Moreover, it should be clear that a normalization of S_0 to itself result in a constant value of one that will not be depicted at all for the sake of clarity. Instead of this nSPP, the degree of polarization (DOP) represented by magenta squares will always be depicted together with the nSPPs S_1, S_2 and S_3 as it is clearly visible from Figure 4.3a). In this figure, the preassigned linearly horizontally polarized state of light (crystalline axis [110]; S1=+1) is clearly observable at an attenuation of 0dB. Here, S1=+1 (red plus) as well as the DOP=1 (magenta squares), whereas S_2 (blue cross) and S_3 (green circle) are almost zero. The small amount of S_2 of 0.1 is due to a non-relevant misalignment of the transmission axis of the linear polarizer with respect to the crystalline axes of the VCSEL of about 3°. By increasing the attenuation from 0dB up to 1.86dB the SNR drops down from roughly 10000 to a value of 100 (right scale). However, the values of the nSPPs together with the DOP remain constant. By increasing the attenuation further above 2dB up to a value of 4.16dB the SNR drops down to a value of two, together with a reduction of the DOP as well as the nSPP S_1 from 1 to 0.2, denoting a nearly unpolarized state of light. From these results we conclude that a SNR above 100 is needed to measure the correct nSPPs together with the correct value of the DOP as well.
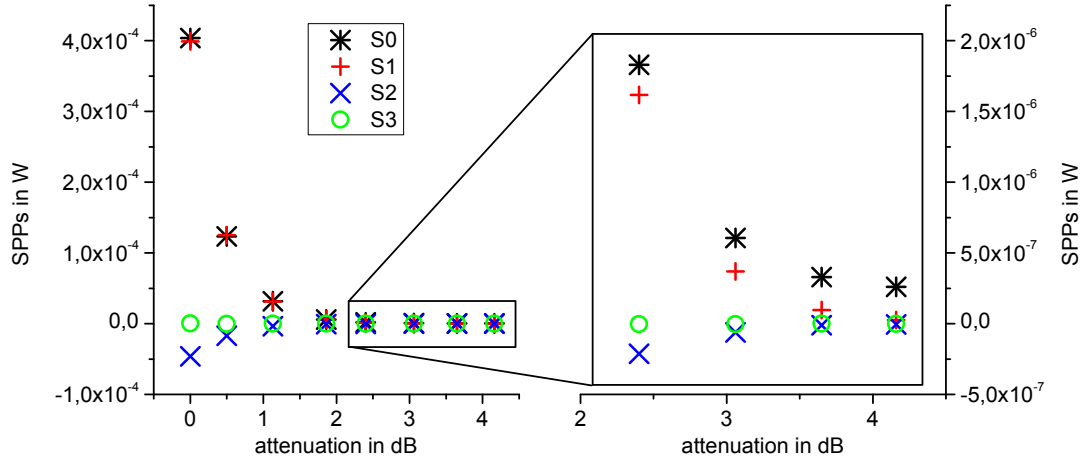

Figure 4.2 Stokes polarization parameters S_0 (black star), S_1 (red plus), S_2 (blue cross) and S_3 (green circle) as a function of attenuation in dB for a preassigned linear polarization on differently scaled y-axis (left) and (right).

The next considerations are about the experimentally obtained sets of data, namely the amount of recorded data with respect to the rotation angle β of the quarter-wave plate multiple modulo π and the resolution of the angle β between 5° and 35° in steps of 5°. The nSPPs obtained from these different sets of data are depicted in Figure 4.3b). In this figure, A), B), C) and D) denote the range of β being between 0 and 4π, 0 and 3π, 0 and 2π, 0 and π, respectively. Furthermore, the different angle resolutions of β result in different amounts of data points on the basis of measurements between 0 and π are depicted as well, denoted with I), II), III), IV), V), VI) and VII) representing an amount of data points of 37, 19, 13, 10, 8, 7 and 6, respectively. Additionally, the error bars according to each nSPPs and the DOP value

are depicted in Figure 4.3b). These errors, obtained from the multi-parameter fitting process performed with a MatLab routine, demonstrate that a set of data, within the range between 0 and π (Figure 4.3b)D)) is sufficient, to obtain the right state of polarization together with the correct value of the DOP both exhibiting small errors not exceeding 2%. Furthermore, the nSPPs obtained from different values for the resolution of the rotation angle β starting at 5° exhibiting 37 data points at I) increasing in steps of 5° up to 35° (6 data points only) at VII) uncovering that the state of polarization as well as the DOP remain constant, however, by decreasing the amount of data points from 37 to 6 the error increases as well, such that large error bars at VII) are clearly observable, however not exceeding 10% at all. Taking these results serious, the measurements have to be performed by recording data points in a range between 0 and π with a resolution of 5°, to optimize measurement time, effort and reliability, such as small errors of less than 2%. With this proof of correctness of the in detail explained reliable measurement technique we are now able to quantify the complex polarization states of VCSELs as follows.
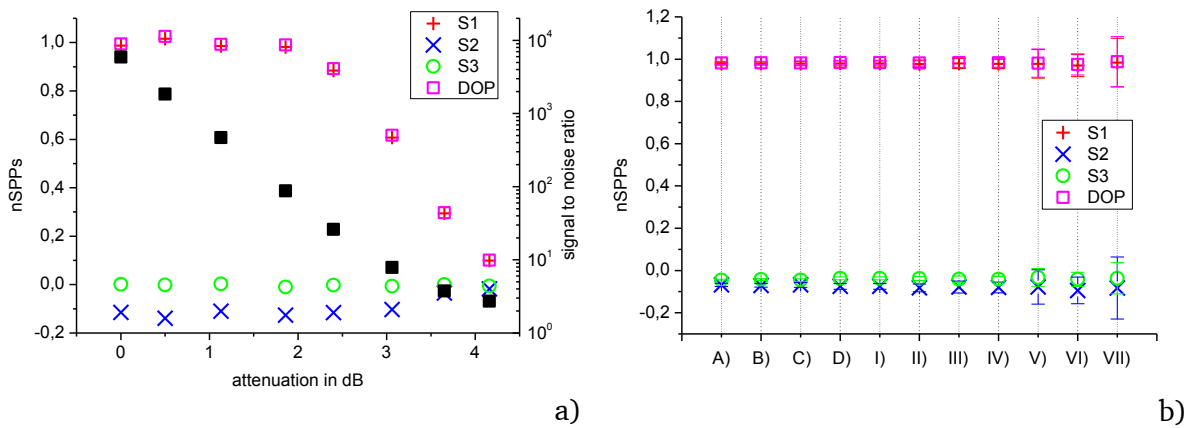

Figure 4.3 a) Normalized Stokes polarization parameters (left scale) S_1 (red plus), S_2 (blue cross), S_3 (green circle) and DOP (magenta squares) as a function of attenuation in dB together with SNR (black squares, right scale), showing a reduction of the DOP when decreasing the SNR below a value of 100. b) Normalized Stokes polarization parameters for different sets of data points A), B), C) and D) from $0 - 4\pi$, $0 - 3\pi$, $0 - 2\pi$ and $0 - \pi$ with a resolution of 5°, together with a variation of the angle of resolution from 5° to 35° in steps of 5° I)-VII).

In the following part the experimental results of nSPPs as a function of pump current for VCSELs (ULM Photonics Philips) emitting at a central wavelength of 850nm are presented. These devices were selected with respect to the diameter of their oxide aperture of 3μm, 4μm and 10μm, in order to provide a hierarchical complexity of the spatial emission, where the threshold for the selected devices amounts to 0.5mA, 0.6mA and 2.0mA, respectively.

In Figure 4.4a) one can observe the total optical power as a function of pump current represented by a black line for a 3μm device, with the laser threshold at 0.5mA and the thermally induced rollover at 5mA. Additionally in this graph, the two orthogonal linear polarizations, aligned with the crystaline axes [110] and [-110], represented by a blue and a red line, uncover a polarization switch (PS) at 2.5mA and a second polarization changing event between 3.5mA and 4.0mA. If we now analyze the polarization behavior in terms of the Stokes formalism, we find in comparison to these results, the complex behavior reflected by the nSPPs S_1 (red plus), S_2 (blue cross), S_3 (green circle) together with the DOP (magenta square) all as a function of pump current, depicted in Figure 4.4b) which will be explained in the following.
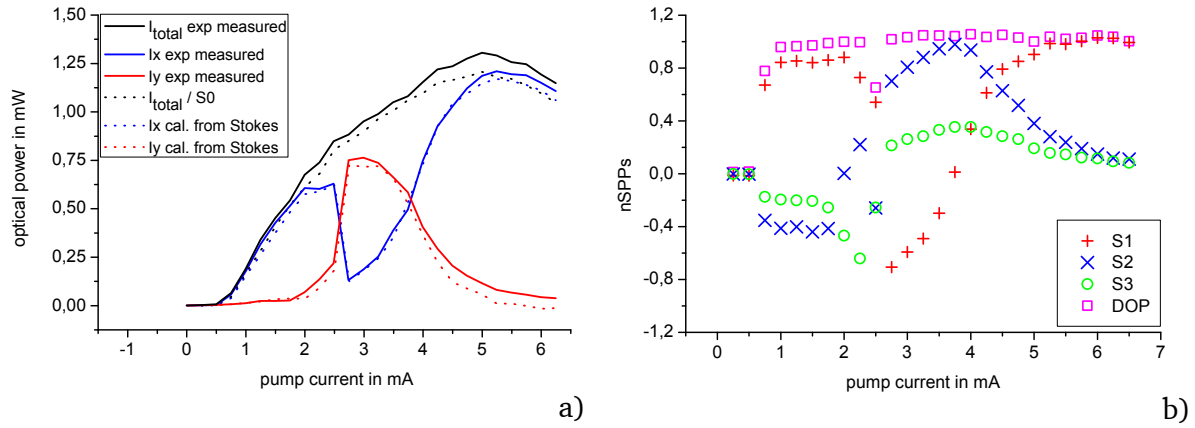
Figure 4.4 a) Polarization resolved P-I curve of a 3µm device (straight lines measured) together with the, from the Stokes polarization parameters, calculated intensities projected on an orthogonal linear polarization projection basis aligned with the crystalline axis [-110] and [110] (dotted lines calculated from SPP), in comparison with the normalized Stokes polarization parameters together with the DOP all as a function of pump current b).

Below the laser threshold at 0.5mA, all these values are very close to zero, representing an unpolarized state of light due to the spontaneous character of the emitted light. Increasing the pump current above the laser threshold up to 2.0mA, the DOP (magenta square) as well as S_1 (red plus) are now close to 1, together with S_2 (blue cross) of about -0.5 and a small value of S_3 (green circle) of -0.2. Therefore, we conclude that the state of polarization is almost linear with its orientation slightly tilted with respect to the crystalline axis [1 1 0] and it still contains a small amount of left circular polarization. In the pump current regime between 2mA and 3mA at 2.25mA, we find a state of polarization with a large amount of left circular polarization $S_3 \approx$ -0.8 (green circle). Then, with increasing current the polarization state switches back to linear with a small amount of right circular polarization S_3 = 0.4 (green circle) like that below 2.0mA. However, it is now with an opposite sign, which means that the direction of rotation has changed. Furthermore, the signs of both values S_1 (red plus) and S_2 (blue cross) have changed too, denoting a rotation of the orientation of the linear polarization by about 90°. Only this latter behavior can clearly be seen in the P-I curve (Figure 4.4a)), where the vertical polarization is dominant above the PS. By further increasing the pump current, the horizontal polarization becomes more and more dominant up to 3.75mA, where an equal power condition with respect to both linear polarizations is clearly visible in Figure 4.4a). At this operation condition in Figure 4.4b) the orientation of the linear polarization with an orientation of +45° is well reflected by $S_2 \approx 1$ (blue cross) together with negligible contributions of both S_1 (red cross) and S_3 (green circle). Up to the rollover at 5mA the state of polarization remains fully linear due to a still negative contributions of S_3 (green circle), however with a rotation of the orientation of the linear polarization from +45° (S_1 = 0, S_2 = 1) back to linear horizontal (S_1 = 1, S_2 = 0).

Beside the total optical power (black line) and the linearly orthogonally polarized components I_y (red line) and I_x (blue line), their counterparts calculated from the experimentally obtained (not normalized) SPPs are depicted for comparison in Figure 4.4a). These counterparts are represented by dotted lines and the same color code such as black for the total intensity as well as blue and red for the intensity projected on the x- and y-axis, respectively. This comparison clearly shows that the SPP S_0 (black dotted line) coincides with the measured total optical power I_{tot} (black line) as well as the two orthogonally linearly polarized counterparts I_x and I_y determined via the following mathematical expressions

$$I_x = \frac{1}{2}(S_0 + S_1) \tag{4.4}$$

and

$$I_y = \frac{1}{2}(S_0 - S_1). \tag{4.5}$$

This comparison clearly demonstrates that also the incomplete results of the polarization resolved P-I curves using a linear polarizer only are captured by the powerful Stokes formalism. However, for the sake of clarity, this comparison will not be explicitly given for the following results of VCSELs with larger oxide aperture diameters.
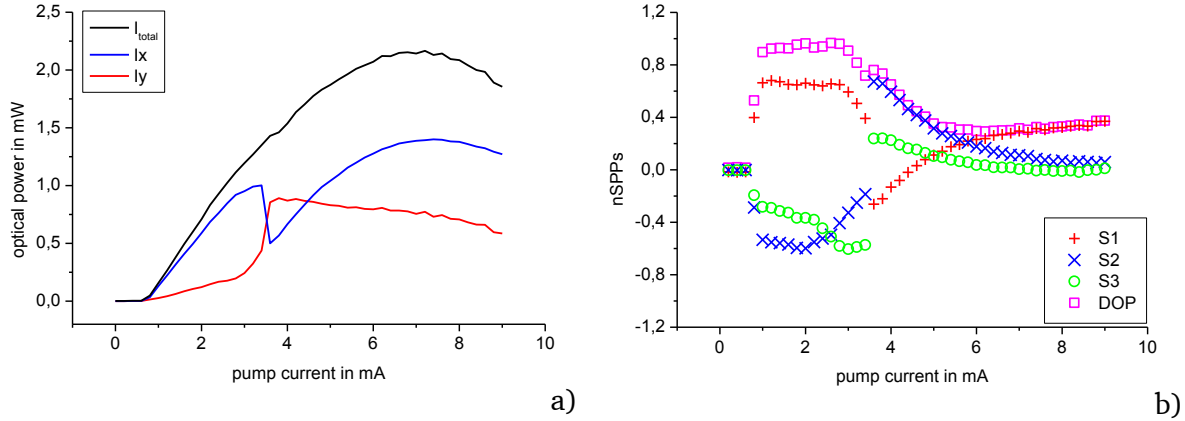

a) b)
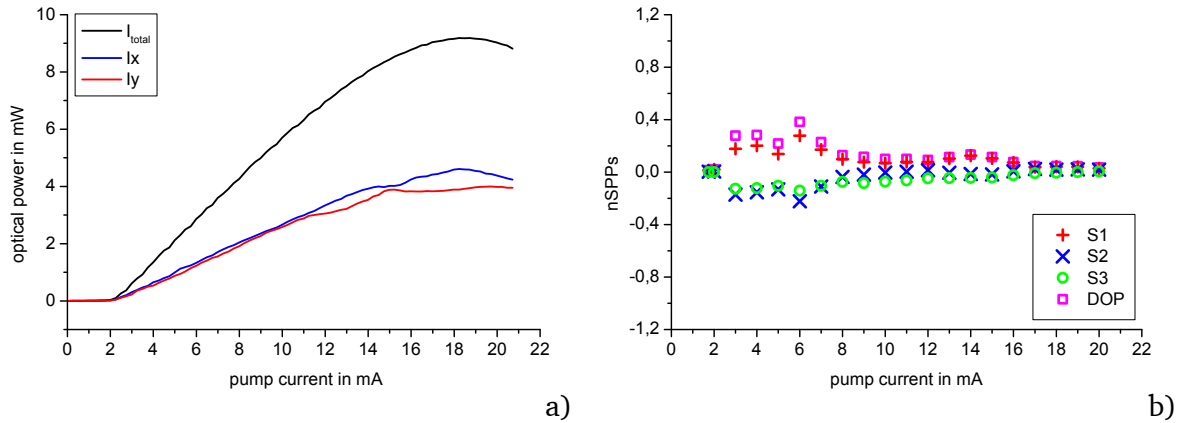
Figure 4.5 a) Polarization resolved P-I curve of a 4µm device, total optical power I_{tot} (black line) together with the optical power of the linear horizontal polarization (blue line) and the linear vertical polarization (red line), in comparison with the normalized Stokes polarization parameters S_1 (red plus), S_2 (blue cross), S_3 (green circle) and the DOP (magenta square) all as a function of pump current b).

Figure 4.5 shows the results of a $4\mu m$ device, which are nearly identical to the behavior of the $3\mu m$ device up to the PS. The behavior of the polarization resolved P-I curves (on a linear polarization basis only) visible in Figure 4.4a) and Figure 4.5a) is completely comparable, whereas the nSPPs show a different behavior above the PS, showing up in a reduction of the DOP (magenta square) from 1 to a value of 0.4 for high pump current values. This means that the amount of polarized light is now less than half of the total emission. Furthermore, the polarized part of the light is linearly polarized and horizontally aligned due to the fact that S_1 (red plus) is almost equal to the DOP (magenta square).

The polarization resolved P-I curve of the third device with an oxide aperture of $10\mu m$ depicted in Figure 4.6a), exhibits a good coexistence of both orthogonal linear polarizations I_x and I_y represented by a blue and a red line, respectively. Here, from this observation only the polarization state of the VCSEL could be either linearly polarized with an orientation of $+45°$, circularly polarized or being unpolarized. In Figure 4.6b) the nSPPs unveil that the state of polarization except in the pump current regime between 3mA and 7mA is in fact unpolarized, due to the fact that all nSPPs together with the DOP are very close to zero. This result of an unpolarized state of light has been verified utilizing a revolvable linear polarizer only, in a first step, as well as a combination of a quarter-wave plate and a linear polarizer in a second step comparable to the method described in [53]. In contrast to the quantitative method described above analyzing the intensity as a function of the rotation angle β of the quarter-wave plate, here the intensity as a function of the rotation angle of the transmission axis of the linear polarizer with respect to the horizontal axis, with and without a quarter-wave plate has been analyzed. With this qualitative method one can differentiate between the seven

states of polarization, such as, linear, circular, elliptical, partial[5] linear, partial elliptical, partial circular and finally an unpolarized state of light[6]. In the present case (the qualitative method), the measured intensity as a function of the rotation angle of the linear polarizer shows rather a modulation neither with nor without a quarter-wave plate, which means that the state of the light is indeed unpolarized. The reduction of the DOP by increasing the oxide aperture diameter is probably related to the stimulated emission of higher order transverse modes due to the increased oxide aperture diameter. This assumption will be investigated further in the following chapters.

Figure 4.6 a) Polarization resolved P-I curve of a 10µm device, total optical power I_{tot} (black line) together with the optical power of the linear horizontal polarization I_x (blue line) and the vertical linear polarization I_y (red line), in comparison with the normalized Stokes polarization parameters S_1 (red plus), S_2 (blue cross), S_3 (green circle) and the DOP (magenta square) all as a function of pump current b).

Our comparison of the polarization resolved P-I curves and the injection current dependence of the nSPPs clearly shows that only the latter unveil the complete information about

    (i)   the amount and the orientation of the linear polarization,

    (ii)   the amount and the orientation of the circular polarization and finally

    (iii)   the degree of polarization.

The presented technique can also give insight into the polarization behavior of the recently intensively investigated field of spin-polarized semiconductor emitters [54] [55] [56] and of VCSELs exhibiting extraordinary additional structures such as a monolithically integrated surface grating on top to control the polarization technologically or micro-electro-mechanical-systems (MEMS) instead of the upper DBR mirror to achieve a mode-hop free tuneability in wavelength of about 100nm. The experimentally obtained results of the SPPs of surface-grating VCSEL, MEMS tunable VCSEL together with a standard VCSEL under mechanical stress, which should give an idea of how sensitive the polarization behavior in these devices is, can be found in the appendix.

To conclude the presented experimental results of this chapter, one should keep in mind that polarization resolved experiments based only on a linear polarizer projection camouflage the

---

[5] partial means here with an amount of unpolarized light
[6] a detailed guidance can be found in [53]

full polarization state knowledge. Using Stokes polarization parameters, however, the full information about the polarization state of light is clearly visible.

Further investigations on Stokes polarization parameters of VCSELs regarding spatially, spectrally and time-resolved measurements are presented in the following chapters. In the next one the actual experimental setup is expanded to perform spatially resolved measurements of Stokes polarization parameters of a small-area VCSEL. Furthermore, these results are compared with their numerically simulated counterparts.

5. Spatially resolved Stokes polarization parameters SPPs(x,y)

The previous chapter exposed that the Stokes polarization parameters (SPPs) are mandatory to uncover the full information of the state of polarization of VCSELs with different size of their oxide apertures. In the present chapter the previously utilized experimental setup, using a photo detector measuring the spatially integrated intensity, is extended by a charge-coupled device (CCD) camera to perform spatially resolved Stokes polarization parameter (SPPs(x,y)) measurements to uncover spatially inhomogenous polarization characteristics, that have been predicted by theoretical calculations [57]. Even nowadays the polarization of light plays an important role in optical science and engineering due to an increasing interest in beams with spatially inhomogeneous states of polarization as it is comprehensively described in [58] which motivate the spatially resolved measurements even further.

First in this chapter, some detailed information concerning the utilized CCD camera and the analysis routine, for the determination of the SPPs are given, together with a validation of this extended experimental setup in form of a comparison of nSPPs obtained with a photo detector and a CCD camera. After that, the spatially resolved nSPPs of a small-area VCSEL in comparison with their numerically simulated counterparts are presented and discussed.
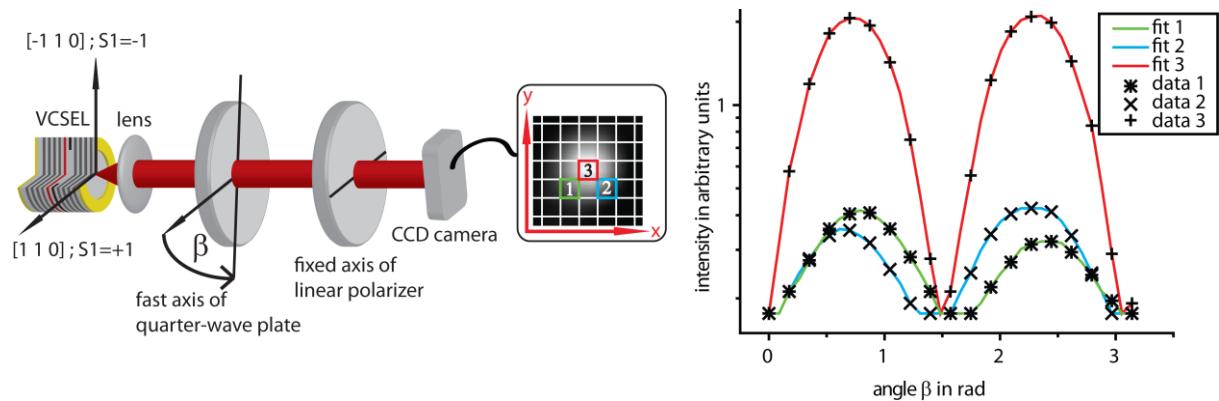

Figure 5.1 (left) Schematical drawing of an experimental setup showing the VCSEL with the crystalline axes [110] and [-110]. The emitted light is collimated by a lens, passes a combination of a quarter-wave plate with revolvable fast axis and a linear polarizer with fixed transmission axis and finally the spatial intensity distribution is detected by a CCD camera. In the right part a representative set of the intensity of three selected different pixels (1-star, 2-cross, 3-plus) of the near-field image (left) is shown as a function of the angle β in radians together with a fit to the measured data (colored lines) to extract the Stokes polarization parameters. The 2D Stokes polarization parameters distribution is calculated for each pixel using this procedure.

The extended experimental setup (Figure 5.1(left)) to uncover SPPs(x,y) is achieved via a CCD camera (Apogee AP1) with 768x512 pixels, a dynamic range of each pixel with respect to the measured intensity in arbitrary units between values of 0 and 16586 and a manually tunable exposure time between roughly 25ms up to several minutes. However, due to sufficient intensity of the VCSELs emitted light, the exposure time never exceeds one second to prevent repletion of the CCD chip of the camera. The spatially resolved nearfield images of the VCSELs emitting facet, recorded for different angles β of the quarter-wave plate have been exploited via a MatLab routine[7], thus determining the SPPs of each pixel, such that a multi-parameter fit is performed with respect to the detected intensity as a function of the rotation

---

[7] a modified version of the routine applied in chapter 4

angle β, depicted in Figure 5.1(right), for three representative sets of data of three different pixels (1-star, 2-cross and 3-plus). Recomposing the SPPs of each pixels to one image, provide spatially resolved SPPs that have been normalized to the maximum value of $S_0(x,y)$, representing the spatially resolved emission of the VCSEL or in other words, the nearfield image of the VCSELs emitting facet recorded without polarizing elements.
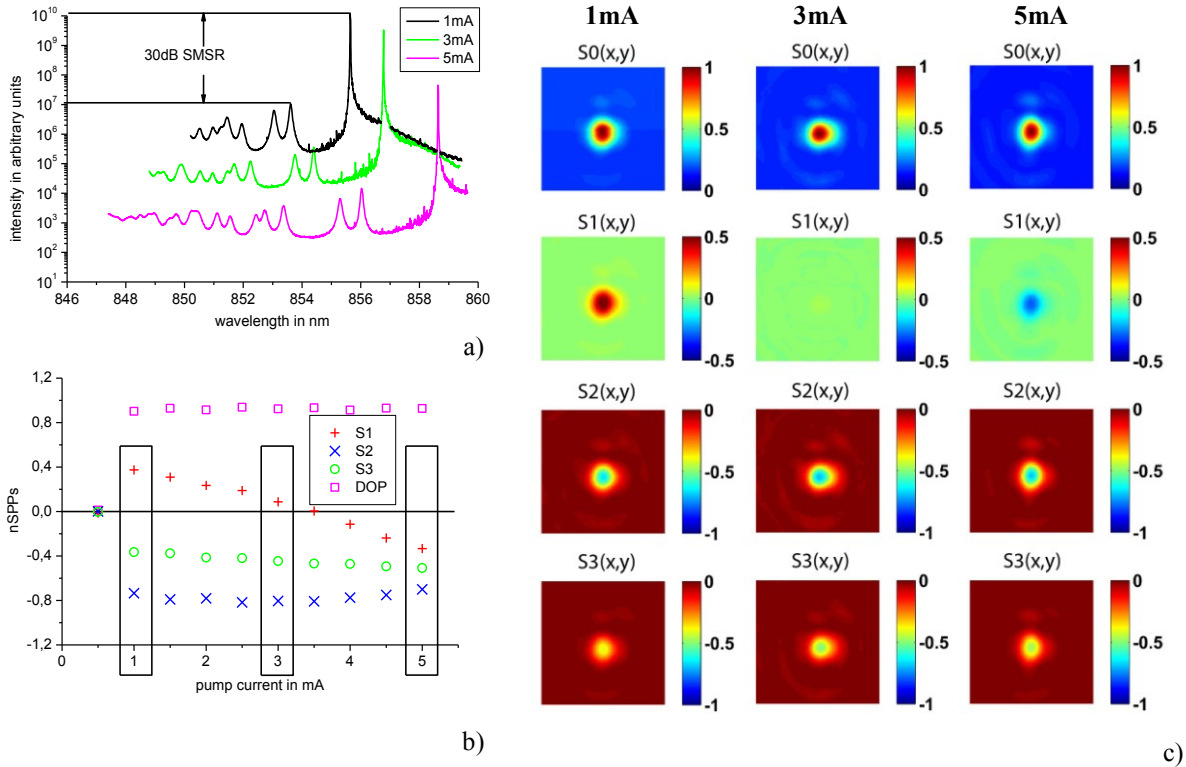

Figure 5.2 a) Optical spectra for 1mA (blue line), 3mA (green line) and 5mA (magenta line) demonstrating a transverse single-mode operation with a side-mode suppression ratio (SMSR) of 30dB of the investigated small-area VCSEL. b) Normalized Stokes polarization parameters S_1 (red plus), S_2 (blue cross), S_3 (green circle) and DOP (magenta squares) as a function of pump current (bottom). Spatially resolved normalized Stokes polarization parameters of a transverse single-mode VCSEL at pump current values of 1mA, 3mA and 5mA c).

To check the mode of operation of the CCD camera with respect to properly determine the spatially resolved SPPs, especially the correct DOP, we compare the experimentally obtained results of SPPs, using the experimental setup with a photo detector from the previous chapter with those of the above described extended version utilizing a CCD camera to realize spatially resolved measurements. The investigated VCSEL has an oxide aperture diameter of $2\mu m$ operating in a transverse single-mode regime only, clearly visible from Figure 5.2a) where optical spectra on a logarithmic scale at pump current values of 1mA (black line), 3mA (green line) and 5mA (magenta line) are shown. These optical spectra were measured via a grating spectrometer in Czerny-Turner configuration, realizing a high optical resolution of at least 10pm at a wavelength of 850nm, in combination with a photo multiplier tube in single photon counting operation mode with a dark count rate of less than 10 counts per 100ms, together with a maximal counting rate of 30.000 in combination with a variable attenuation wheel, enabling the measurement of the intensity of our optical spectra over 4 orders of magnitude very precisely. In Figure 5.2b) nSPPs S_1 (red plus), S_2 (blue cross), S_3 (green circle) together with the DOP (magenta square) all as a function of the pump current are depicted. Below the laser threshold slightly below 1mA all nSPPs as well as the DOP are close to zero due to the spontaneous character of the VCSEL´s emitted light. Above the laser threshold up to a pump current value of 5mA at the thermally induced rollover, the DOP (magenta squares), S_2 (blue cross) and S_3 (green circle) remain constant at values of 1, -0.4

and -0.8, respectively. However, the value of S_1 (red plus) gradually changes from +0.4 to -0.3 at pump current values of 1mA and 5mA, respectively. This reflects a rotation of the orientation of the linear polarization of about 25°, calculated from the nSPPs at 1mA and 5mA via $\psi = 0.5 \operatorname{atan}(S_2/S_1)$. Here ψ denotes the angle of the polarization ellipse with respect to the horizontal axis aligned with the crystalline axis [110]. This change of sign of the normalized Stokes polarization parameter S_1 is also clearly observable in Figure 5.2c), where spatially resolved nSPPs $S_0(x,y)$, $S_1(x,y)$, $S_2(x,y)$ and $S_3(x,y)$ in the 1st, 2nd, 3rd and 4th row for three selected pump current values of 1mA, 3mA and 5mA (left, middle and right columns) are respectively depicted. The Gaussian-shaped intensity distribution of $S_0(x,y)$ (reflecting the transverse nearfield image) is typical for the fundamental transverse mode of the VCSEL. The color coded values of the spatially resolved nSPP $S_1(x,y)$ depicted in the 1st row of Figure 5.2c) are in a range between -0.5 (blue) and +0.5 (red). This clearly reveals a transition from positive values ($S_1(x,y)$ at 1mA) over a zero contribution of $S_1(x,y)$ at 3mA, which cannot be distinguished from the background, to a negative value of $S_1(x,y)$ at 5mA. The color bars of $S_2(x,y)$ and $S_3(x,y)$ are in a range between 0 (red) and -1 (blue), which means that they are shifted to the negative about a value of 0.5, thus resulting in the fact that for $S_2(x,y)$ and $S_3(x,y)$ the unpolarized background with a value of zero is now represented by a red color. However, the constant contribution of $S_2(x,y)$ and $S_3(x,y)$ of values roughly between -0.5 and -1 as well as 0 and -0.5, respectively, are clearly observable.

Although, these preliminary results on nSPPs(x,y) show already a quite good coincidence with non-spatially resolved nSPPs, obtained using the experimental setup with a photo detector integrating the intensity over space, for full agreement we have to find out the correct exposure time of the CCD camera, such that the DOP and the nSPPs integrated over 11x11[8] pixels show the same values as their counterparts obtained via a photo detector. Therefore, we have checked this by considering a fully linearly polarized state of light with a DOP=1 as well as a large, dominant and positive contribution of S_1 together with negligible contributions of both S_2 and S_3.

In Figure 5.3a) nSPPs together with the DOP all as a function of the exposure time of the CCD camera, in the range between 25ms and 375ms reveal always the same, correct state of polarization. However, with a slight increase of the DOP value from 1 to 1.45 by decreasing the exposure time down to 25ms. Above 175ms the value of the DOP is very close to 1, whereas the nSPPs S_1, S_2 and S_3 remain constant with +1, 0 and a negligible negative amount, respectively. Additionally, the signal to noise ratio (black squares, right scale) or more precise the ratio of S_0 to the amount of dark counts of the CCD camera is also depicted as a function of exposure time, thus demonstrating on the one hand the good linearity of the camera and on the other hand giving a lowest limit for the signal to noise ratio (SNR>1) to obtain a reliable and correct value of the DOP.

---

[8] With an integration over 11x11 pixel we were able to cover the most of the Gaussian-shaped intensity distribution.
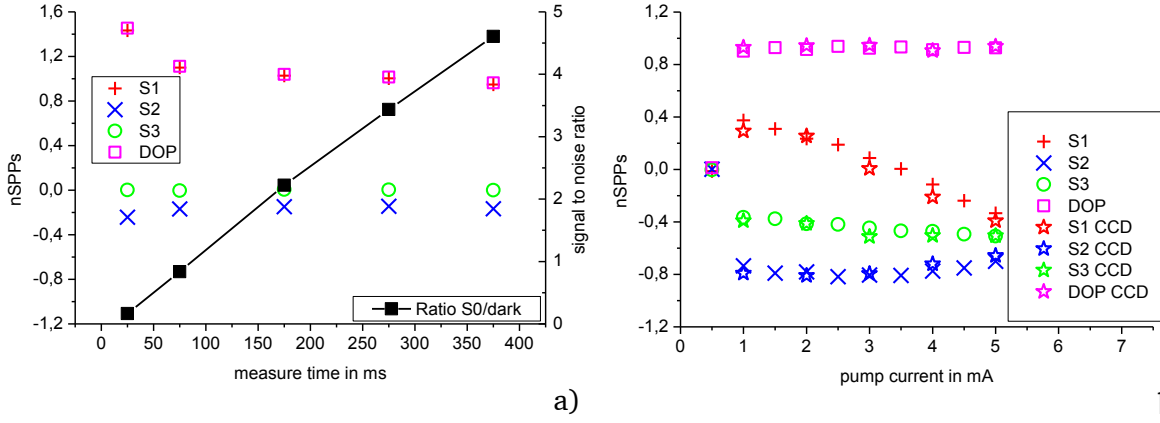
Figure 5.3 a) Normalized Stokes polarization parameters S_1 (red plus), S_2 (blue cross), S_3 (green circle) and DOP (magenta square) of a prepared linear state of polarization all as a function of exposure time of the CCD camera (left scale) together with the determined signal to noise ratio (SNR, black, right scale). Comparison of nSPPs obtained with a photo detector S_1 (red plus), S_2 (blue cross), S_3 (green circle) and DOP (magenta square) and the spatially resolved results integrated over an area of 11x11 pixel using a CCD camera S_1 (red star), S_2 (blue star), S_3 (green star) and DOP (magenta star), showing an excellent coincidence of the results b).

Therefore, we now keep the exposure time above 175ms for all spatially resolved measurements. For the comparison of the nSPPs of a small-area VCSEL using a photo detector (cf. chapter 4) and the here described extended version utilizing a CCD camera for spatially resolved measurements, we have to integrate the spatially resolved results over an area of 11x11 pixels to make these resulting values directly comparable. This comparison is depicted in Figure 5.3b) where nSPPs (photo detector) are represented by their in this thesis utilized symbols (red plus for S_1, blue cross for S_2, green circle for S_3 and magenta square for the DOP) in comparison with the nSPPs (CCD camera integrated over 11x11 pixels) presented by a color coded star with the corresponding color for S_1, S_2, S_3 and the DOP of red, blue, green and magenta, respectively. These results perfectly coincide such that the CCD camera measurements reproduce the correct nSPPs including the DOP, ensuring that this extended experimental setup is capable to measure spatial inhomogenous polarization distribution. This has been already reported and investigated in the past in [57] and [59] taken into account a linearly polarized beam of light with a Gaussian-shaped beam profile, however on a linear orthogonal polarization projection basis only. And we did indeed find a particular challenging VCSEL that´s special feature will be explained in the following, with which this device fulfills the above mentioned requirements.

In the following a full polarization analysis in terms of SPPs(x,y) is performed on a small-area VCSEL with a fixed linear polarization achieved via a monolithically integrated surface-grating on top of the VCSEL.
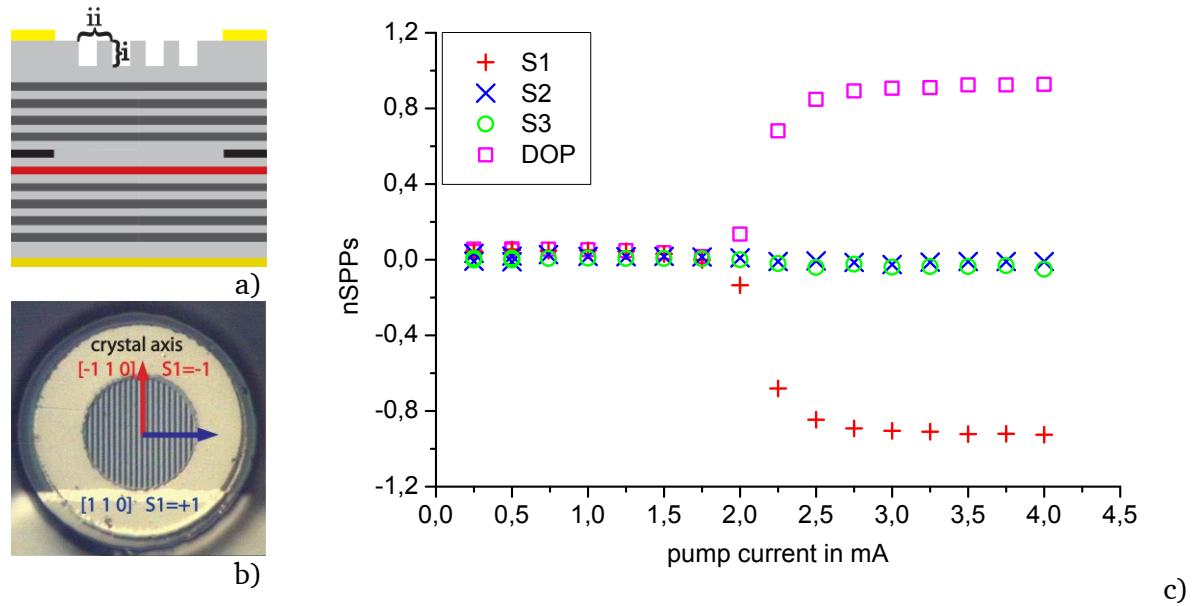
Figure 5.4 a) Schematic drawing of the VCSEL structure showing the active layer (red), the oxide aperture (black), the high reflecting DBR mirrors framed by the electrical contacts (yellow) and the surface-grating with its parameters etching depth (i) and grating period (ii) on top. A photographical picture of the top view of the VCSEL, showing the orientation of the grating grooves with respect to the crystal axis [-110] and [110] here depicted schematically with a red and a blue arrow, respectively b). Normalized Stokes polarization parameters as a function of pump current measured using a photo detector. The polarization control due to the surface-grating is clearly visible regarding the constant state of polarization represented by a dominant contribution of the negative value of S_1 (red plus) and small but non–zero contributions of S_3 (green circle) and S_2 (blue cross). Due to the transverse single-mode operation the VCSEL´s total emission is fully polarized reflected in the DOP value close to one above laser threshold at 2mA c).

Figure 5.4a) shows a schematic drawing of an investigated VCSEL (ULM Photonics Phillips) emitting at a central wavelength of 850nm. The investigated devices have been selected with respect to both the diameter of their oxide aperture of 3μm (black) and their surface-grating parameters, namely an etching depth of 52nm (i) and a grating period of 0.9μm (ii), therefore providing a reliable polarization control, such that neither a polarization switching nor a change of the orientation of the linear polarization is observable [60]. The orientation of the equidistant grating grooves has been thoughtfully selected to be aligned with the crystal axis [-110] of the semiconductor device, depicted in the photographic picture in Figure 5.4b), showing a top view of the VCSEL with its crystal axes and the surface-grating on top. This selected device is appropriate because of its small oxide aperture diameter: it emits transverse single-mode. Thus, the resulting weaker four-lobe component[9] can be analyzed experimentally via Stokes formalism, although its intensity is reduced by a factor in the range between 10^4-10^5 with respect to the intensity of the Gaussian-shaped component as it has been reported in [57]. The experimentally obtained spatially resolved Stokes polarization parameters $SPPs_{exp}(x,y)$ are compared with their numerically simulated counterparts $SPPs_{sim}(x,y)$ generated by VCSEL ELectroMagnetic (VELM) code [61] to understand the underlying mechanisms. The transverse single-mode operation of a small oxide aperture diameter VCSEL allows us to neglect transverse mode competition in the numerical simulations. Therefore, a simpler cold-cavity approach is appropriate for comparing experimentally and numerically obtained results of the spatially resolved Stokes polarization parameters. Before presenting these results we want to demonstrate the excellent functionality of the surface-grating, clearly visible from Figure 5.4c), where the nSPPs S_1 (red plus), S_2 (blue cross) and S_3 (green circle) as well as the degree of polarization (DOP,

---

[9] This component is predicted by theory with its linear polarization orthogonally oriented to the dominant Gaussian-shaped polarization component and can be observed in Figure 5.6.

magenta square) of the total emission are plotted as a function of pump current. Below the laser threshold at 2.0mA[10], all these values are very close to zero, representing an unpolarized state of light due to the spontaneous emission character of the emitted light. Above the laser threshold a sharp increase of the DOP (magenta square) from 0 to 1 and a sharp decrease of S_1 (red plus) from 0 to -1 are observable. The state of polarization of the fully polarized light (DOP=1) does not change with increasing pump current and is reflected in the dominant value of $S_1 \approx$-1 (red plus) representing a linear polarization oriented parallel to the crystal axis [-110] and the very small, negative and constant contributions of S_2 and S_3 (blue cross and green circle) demonstrating the polarization controlling functionality of the selected surface-grating [60]. These results are comparable with the results of SPPs of a stable transverse single-mode EEL with a ridge optical waveguide [62].

Now, for the first time both the experimentally obtained spatially resolved normalized[11] Stokes polarization parameters $nSPPs_{exp}(x,y)$ (Figure 5.5 top) as well as their numerically simulated counterparts $nSPPs_{sim}(x,y)$ for a small-area surface-grating VCSEL at a pump current of 3mA (Figure 5.5 bottom) are presented and will be discussed [63]. The $SPPs_{sim}(x,y)$ have been calculated using the following mathematical equations well known from chapter 3 containing the definition of the SPPs in terms of two Cartesian components E_x and E_y of the mode profile computed by VELM (the asterisk indicates the complex conjugate)

$$S_0 = E_x E_x^* + E_y E_y^* \tag{5.1}$$

$$S_1 = E_x E_x^* - E_y E_y^* \tag{5.2}$$

$$S_2 = E_x E_y^* + E_y E_x^* \tag{5.3}$$

$$S_3 = i\left(E_x E_y^* + E_y E_x^*\right). \tag{5.4}$$

In the top part of Figure 5.5 the first SPP $S_{0\_exp}(x,y)$ represents the total intensity of the incident light and is in good agreement with the nearfield image recorded without the combination of a linear polarizer and a quarter-wave plate (not depicted here). The minimal value of $S_{1\_exp}(x,y)$ of -1 reflects the linear vertical polarization of the dominant mode and coincides with the results depicted in Figure 5.4c) (red plus). Also a bracket shape framing the Gaussian-shaped central spot shows up, that has been reported also in [64] and which in the present case is attributed to an oblong shape of the oxide aperture, originating from manufacturing processes.

---

[10] The laser threshold is raised in comparison with the laser threshold of a small-area VCSEL with an oxide aperture of 3μm in chapter 3 of below 1mA, due to the monolithically integrated surface-grating [78]

[11] The SPPs(x,y) have been normalized to the maximum value of $S_0(x,y)$.
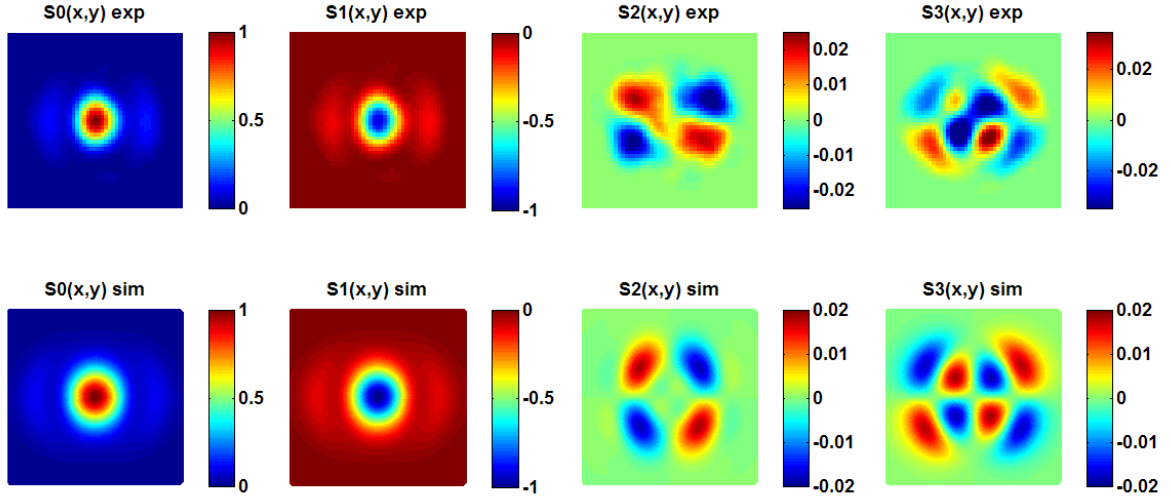
Figure 5.5 Spatially resolved normalized Stokes polarization parameters: experimentally obtained (top row) and numerically simulated (bottom row) results.

In a standard VCSEL without a surface-grating, an elliptically polarized beam of light is in general emitted as we have shown in chapter 4 and as it has been reported in [65]. In the present case, the surface-grating on top of our investigated device fixes the state of polarization such that a dominant linear polarization $S_{1\_exp}(x,y)$ with an orientation parallel to the grating grooves due to the induced dichroism is observable, however still a weak four-lobe pattern shows up in $S_{2\_exp}(x,y)$ (with a change of sign) and in $S_{3\_exp}(x,y)$ one even observes an eight-lobe distribution. Both $S_{2\_exp}(x,y)$ and $S_{3\_exp}(x,y)$ are showing an inner part with the same sign pattern, and additionally an outer part with a complementary sign pattern is observable for $S_{3\_exp}(x,y)$.

A four-lobe symmetry is also observable regarding the weak field component $I_{x\_exp}(x,y)$ depicted in Figure 5.6 together with the strong field component $I_{y\_exp}(x,y)$ and their simulated counterparts. These 2-dimensional intensity distributions on a linear projection basis only have been calculated from the experimentally obtained spatially resolved SPPs $S_{0\_exp}(x,y)$ and $S_{1\_exp}(x,y)$ using the following mathematical expression

$$I_x(x,y) = \frac{1}{2}(S_0(x,y) + S_1(x,y)) \tag{5.5}$$

$$I_y(x,y) = \frac{1}{2}(S_0(x,y) - S_1(x,y)) \tag{5.6}$$

The calculations have been performed on the one hand to visualize the four-lobe intensity distribution with polarization components in the x-direction only as it has been reported already in [59] and on the other hand to determine the ratio between the intensity of the dominant and the weak component to be $15*10^{-4}$, in order to be comparable with the theoretical findings (see Figure 5.6(right)).
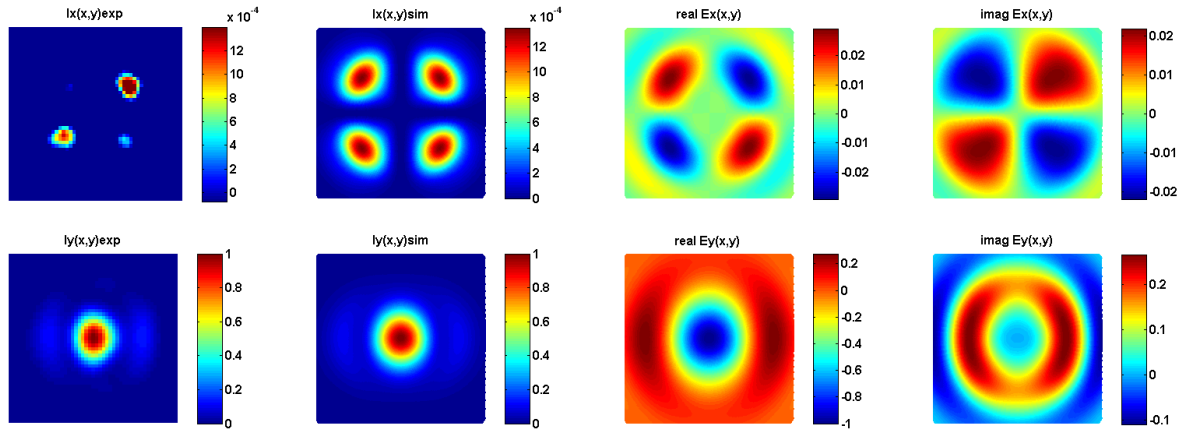
Figure 5.6. Spatially resolved $I_x(x,y)$ and $I_y(x,y)$ calculated from the experimentally obtained Stokes polarization parameters (left) in comparison with their numerically simulated counterparts (right).

Figure 5.7. Numerically simulated real and imaginary part of the $E_x(x,y)$ (top) and $E_y(x,y)$ (bottom) electromagnetic field components, illustrating the origin of the four lobe structure, clearly visible in the real and imaginary part of $E_x(x,y)$.

Coming back to the nSSPs(x,y), the maximal and minimal values of the simulated results (maximal value of $S_{0\_sim}(x,y)=1$; minimal value of $S_{1\_sim}(x,y)=-1$) are in excellent agreement with the experimentally obtained results confirming the dominant linear vertical polarization character of the emission. The patterns of $S_{2\_exp}(x,y)$ and $S_{3\_exp}(x,y)$ are also fully reproduced by the simulations. Also, the maximal and minimal values of $S_{2\_sim}(x,y)$ and $S_{3\_sim}(x,y)$ compare very well with their experimental counterparts, being in the range between -0.02 and 0.02 for both $S_2(x,y)$ and $S_3(x,y)$. As a consequence, also the weak mode component $I_{x\_exp}(x,y)$ and $I_{x\_sim}(x,y)$ compare very well.

By comparing the experimentally obtained and numerically simulated results generated by VELM code, we are able to prove that, in spite the fact that we have a polarization controlling surface-grating, a non-zero amount of

i) a linear polarization $S_2(x,y)$ and

ii) a circular polarization component $S_3(x,y)$, shows up.

The amount of $S_2(x,y)$ and $S_3(x,y)$ and their complex four-lobe and eight-lobe pattern in terms of change of sign, respectively, can be explained by the superposition of the two complex orthogonal linearly polarized electromagnetic field components, originating from the solution of Maxwell´s equations in our VCSEL structure. Indeed, the VELM code applied to a small-area surface-grating VCSEL with a slightly oblong shaped oxide aperture (which major axis is perpendicular to the field-brackets), excellently reproduces the bracket structure, the four- and eight-lobe pattern as well as their normalized values. The numerically simulated spatial distributions of the real and imaginary part of the complex electromagnetic field components E_x and E_y defined via

$$E_x = real(E_x) + i\,imag(E_x) \qquad\qquad (5.7)$$

$$E_y = real(E_y) + i\,imag(E_y) \qquad\qquad (5.8)$$

are depicted in Figure 5.7, thus clearly illustrating the four lobe structure visible in the real as well as the imaginary part of the weak electromagnetic field component E_x. Furthermore, the

bracket structure shows up even in the real part of the dominant E_y field component. These numerically simulated results of the contributing orthogonally linearly polarized electromagnetic field components together with the formulae explicitly given in (5.1) - (5.4) allow to derive the experimentally obtained four- and eight-lobe structure visible in $S_{2\_exp}(x,y)$ as well as $S_{3\_exp}(x,y)$, respectively.

In conclusion, we demonstrated a technique for measuring spatially resolved Stokes polarization parameters of VCSELs. Furthermore, we successfully compared our experimentally obtained results of $nSPPs_{exp}(x,y)$ of a small-area surface-grating VCSEL with their numerically simulated counterparts $nSPPs_{sim}(x,y)$.

This also confirms the rigorous functionality of the VELM code, also with respect to the spatial distribution of polarization in terms of the Stokes formalism. It demonstrates that the measured $\vec{S}(x,y)$ patterns are consequently caused by the modal features of the small-area VCSEL. This comparison and the following investigations on spatio-spectrally resolved Stokes polarization parameter measurements also of transverse multi-mode VCSELs will grant a complete insight into the complex polarization behavior of VCSELs.
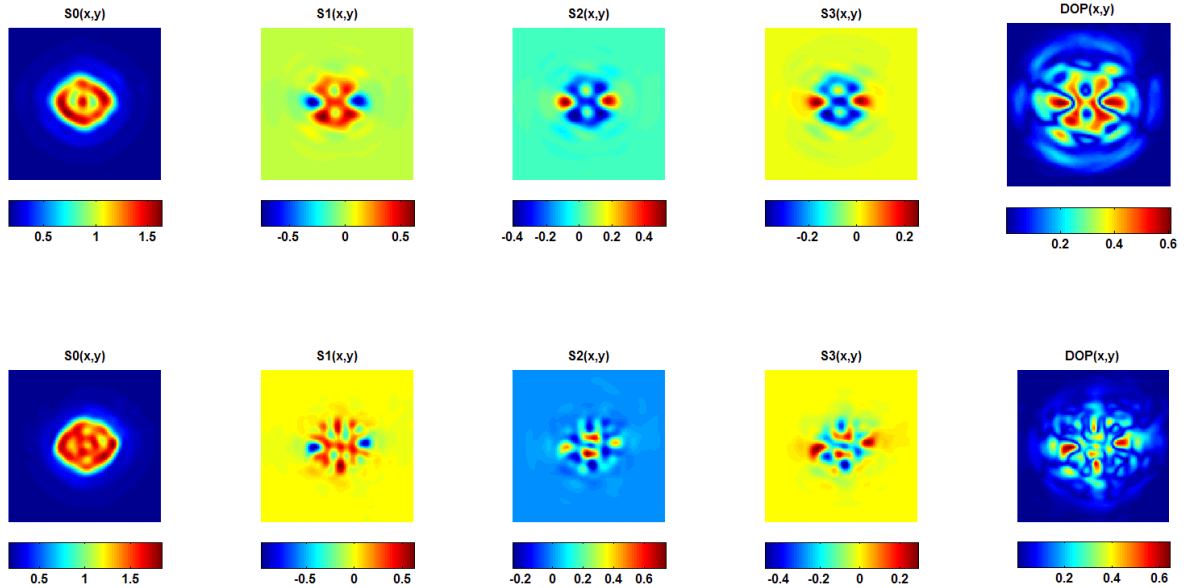

Figure 5.8. Spatially resolved normalized Stokes polarization parameters together with the DOP of a VCSEL with an oxide aperture diameter of 10µm at two selected pump current values of 5mA (top row) and 10mA (bottom row), illustrating a very complex spatial distribution

To motivate spatio-spectrally resolved Stokes polarization parameter measurements further, spatially resolved nSPPs of a large-area VCSEL with an oxide aperture diameter of $10\mu m$, resulting in an emission on multi-transverse modes are depicted in Figure 5.8. The experimentally obtained results of SPPs(x,y) for two different pump current values of 5mA (top) and 10mA (bottom) uncover a circular symmetry, however with a very complex $\vec{S}(x,y)$ pattern, reflected by changes of sign clearly observable in $S_1(x,y)$, $S_2(x,y)$ and $S_3(x,y)$. From these measurements only, one cannot clearly see whether these changes of sign originate from the intensity distribution of one transverse mode as it is the case in the four-lobe structure or rather from a spatial overlapping of higher order transverse modes.

To answer this question an extended experimental setup including a CCD camera, complemented by a monochromator to achieve the spectral resolution regarding the transverse modes, enables one to specifically identify their particular states of polarization together with the DOP.

6. Spatio-spectrally resolved Stokes polarization parameters SPPs(x,y,λ)

At the end of the previous chapter the motivation for spatio-spectrally resolved Stokes polarization parameters (SPPs(x,y,λ)) measurements has already been given, by showing spatially resolved nSPPs of a transverse multi-mode VCSEL, such that its transverse modes are overlapping in space, which prevents the assignment of the spatial distribution of the nSPPs of each individual transverse mode. This chapter is organized as follows; first, the completed experimental setup is explained on the basis of the setup for the spatially resolved measurements. Second, this extended experimental setup is characterized and applied to determine SPPs(x,y,λ) of a transverse multi-mode VCSEL. These results are presented, analyzed and discussed; finally, an explanation according to the reduced value of the DOP below 0.5 demonstrated in chapter 4 is given.
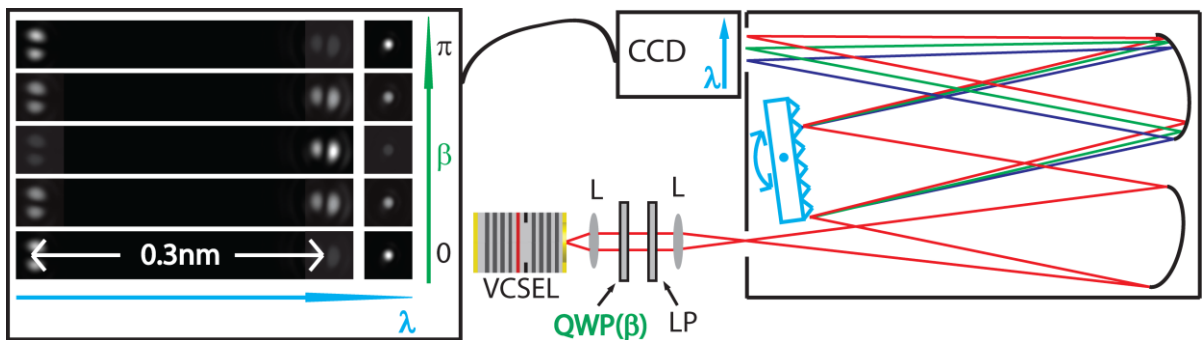
Figure 6.1 (middle) Schematic drawing of an experimental setup including the VCSEL together with polarization state measuring optics, as we already know from previous chapters. Now, in combination with a grating spectrometer (right) connected with a CCD camera to perform spatio-spectrally resolved measurements exemplarily depicted for the first three transverse modes, for five different adjustments of the rotation angle β (in the range between 0 and π) of the quarter-wave plate (left).

A schematic drawing of our experimental setup to determine SPPs(x,y,λ) is depicted in Figure 6.1 including the VCSEL a collimating lens (L) followed by a combination of a revolvable quarter-wave plate (QWP) and a fixed linear polarizer (LP) to perform the polarization analysis. The experimental setup is now complemented via a grating spectrometer in Czerny-Turner configuration (see Figure 6.1(right)), with a grating exhibiting 1800 grating grooves per mm, achieving a high spectral resolution of at least 10pm at a wavelength of 850nm in combination with a width of both entrance and exit slits of 20μm. However, for spatio-spectrally resolved measurements one has to remove both the slits to obtain an image of the light emitting facet of the VCSEL that is not affected by diffraction. This removal of the slits deteriorates the spectral resolution to a value of about 50pm at 850nm. However, this is already enough to clearly separate the intensity distributions of each transverse mode as it is evident from the left part of Figure 6.1, showing spatio-spectrally resolved intensity distributions of the first three transverse modes for five different rotation angles β, indicating a change of intensity of the spatio-spectrally resolved transverse modes as a function of β. One has to remark that this representation exhibits a break in wavelength due to the large gap in wavelength of roughly 1nm between the Gaussian-shaped fundamental mode and the second higher order transverse mode with two horizontally arranged intensity maxima.
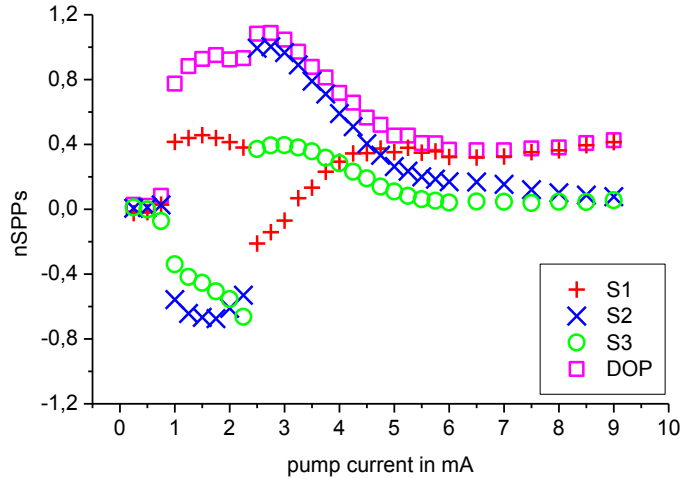
Figure 6.2 Normalized Stokes polarization parameters S_1 (red plus), S_2 (blue cross), S_3 (green circle) together with the DOP (magenta square) as a function of the pump current, uncovering the laser threshold slightly below 1mA, a polarization switch at 2.5mA as well as a reduction of the DOP (magenta square) above a pump current value of 3mA together with another polarization changing event reflected by gradual changes of mainly S_1 (red plus) and S_2 (blue cross).

The investigated standard VCSEL[12] (without surface-grating) with an oxide aperture diameter of 4μm shows a very complex polarization behavior in terms of its nSPPs S_1 (red plus), S_2 (blue cross) and S_3 (green circle) depicted together with the DOP (magenta square) all as a function of pump current in Figure 6.2. These results which are very similar to the results depicted in chapter 4 (cf. Figure 4.5), uncover a polarization switch and a gradual change of the state of polarization, together with a reduction of the DOP (magenta square) from 1 representing a fully polarized state of light to a value below 0.5 describing a predominantly unpolarized state of light. This complex polarization behavior is investigated in more detail regarding the spatio-spectrally resolved nSPPs of each contributing transverse mode. These results together with the DOP are depicted in Figure 6.3 and have been measured at a pump current value of 6mA, such that mostly the first three transverse modes (TM_1, TM_2 and TM_3) contribute to the total emission, clearly visible in an optical spectrum depicted in Figure 6.3(bottom). Here, the intensity, measured as a function of the wavelength utilizing a photo multiplier in single photon counting mode as described in the previous chapter, is depicted, thus uncovering a suppression ratio of the third to the fourth transverse mode of 30dB. The ratio of the maximum intensities of TM_1, TM_2 and TM_3 of 10:2.3:1 observable in the optical spectrum (Figure 6.3(bottom)) is also visible from the (not normalized) SPP $S_0(x,y,\lambda)$ depicted in the first row of Figure 6.3. These results clearly reveal the spatial distribution of the Gaussian-shaped fundamental transverse mode (TM_1) together with its $S_0(x,y,\lambda)$ counterpart of higher order transverse modes TM_2 and TM_3, which exhibit a Laguerre-Gaussian-shaped intensity distribution (middle and left), due to the cylindrical resonator shape of the VCSEL, thus exhibiting two intensity maxima horizontally and vertically aligned for TM_2 and TM_3, respectively. In the second, third and fourth row the spatio-spectrally resolved nSPPs are illustrated for the three contributing transverse modes TM_1, TM_2 and TM_3. The normalization to their individual maxima value of $S_0(x,y,\lambda)$ ensures a comparison of their states of polarization among each other, despite the fact of their very different intensities observable in $S_0(x,y,\lambda)$ for TM_k for k=1,2,3 also visible in the optical spectra below.

---

[12] The investigated VCSEL in this chapter has the same properties in terms of oxide aperture diameter as the VCSEL utilized in chapter 4 and is on the same wafer. We used a second device here to prove the general validity of our experimental findings.
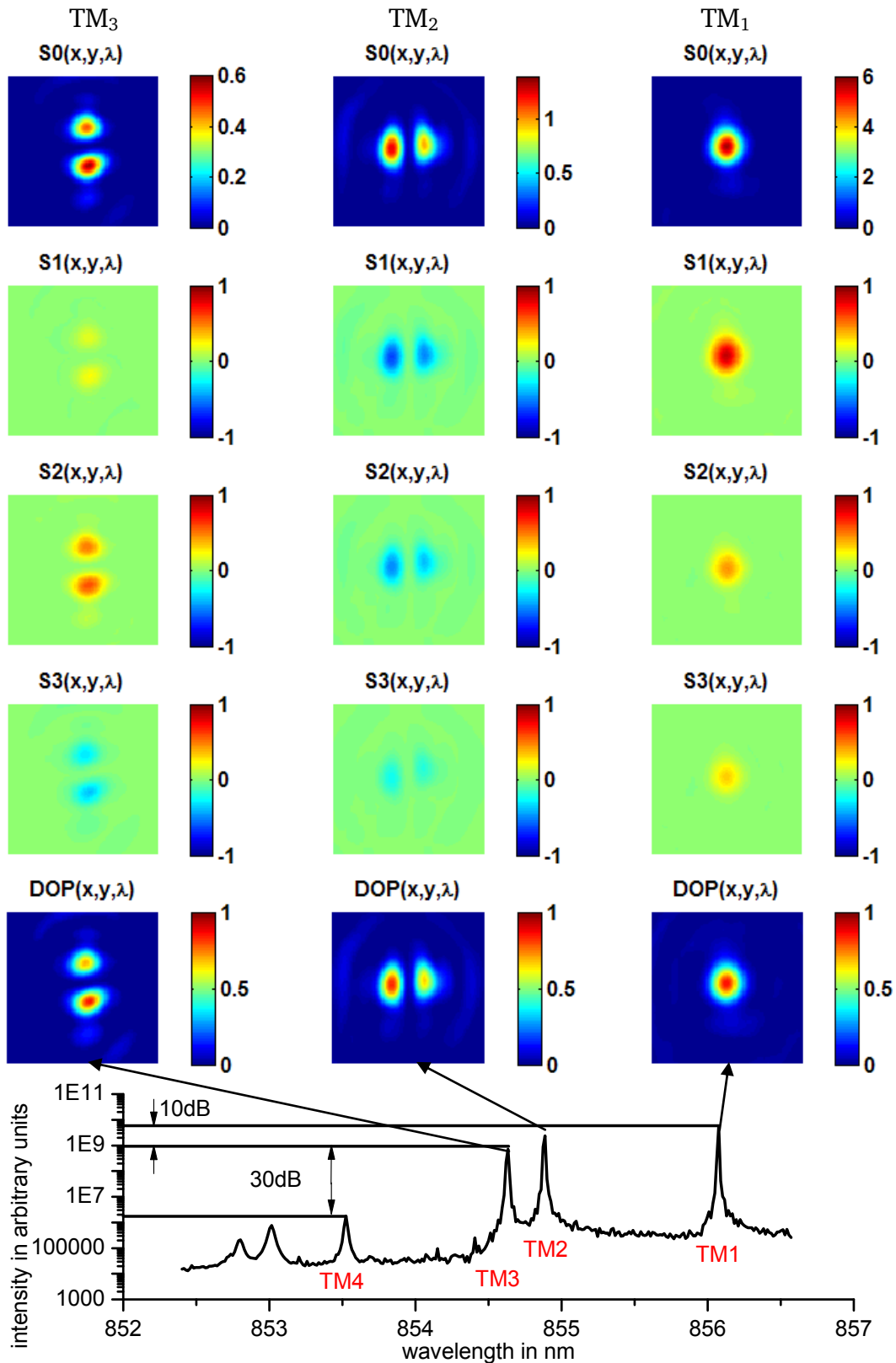
Figure 6.3 (top) Spatio-spectrally resolved normalized Stokes polarization parameters row 1 to 4 together with the DOP bottom row for the first three transverse modes TM$_1$, TM$_2$ and TM$_3$ at a pump current of 6mA; including the fundamental Gaussian-shaped transverse mode TM$_1$ (right) the second and third higher order Laguerre-Gaussian-shaped transverse mode TM$_2$ and TM$_3$ (middle and left), uncovering different states of polarization, regarding the signs of the nSPPs(x,y,λ) of each transverse mode. S_0(x,y,λ) in the 1st row is not normalized, which reflects the real intensity ratio as they are also visible from the optical spectrum at a pump current value of 6mA reflects the transverse multi-mode operation of the VCSEL with a dominant contribution of the first three transverse modes, showing a suppression ratio with respect to the next higher order transverse mode TM$_4$ of 30dB as well (bottom).

Spatio-spectrally resolved Stokes polarization parameters SPPs(x,y,λ)

From these nSPPs(x,y,λ) the complementary contributing transverse modes can be identified via their individual transverse mode profile reflected by the nSPP(x,y,λ) S_0 (1st row). Furthermore, their different nSPPs S_1 (2nd row), S_2 (3rd row) and S_3 (4th row) are clearly observable as well. In detail, in the second row on the right side the peak value of $S_1(x,y,\lambda)$ of TM_1 has a positive value close to 1, whereas the peak contribution of $S_1(x,y,\lambda)$ of TM_2 is negative and somewhere between -0.5 and -1, while the maximal value of the intensity distribution of $S_1(x,y,\lambda)$ of TM_3 is somewhere between 0 and +0.5. In combination with their peak values of $S_2(x,y,\lambda)$ between 0 and +0.5, roughly -0.5 and a rather large value between +0.5 and +1 for TM_1, TM_2 and TM_3, respectively. These findings uncover different orientations for the states of polarization ψ (calculated via $\psi = 0.5 \, atan(S_2/S_1)$), of TM_1 and TM_3 in comparison with TM_2, showing a change of sign regarding of $S_1(x,y,\lambda)$ and $S_2(x,y,\lambda)$ of TM_1 and TM_3 in comparison with $S_1(x,y,\lambda)$ and $S_2(x,y,\lambda)$ of TM_2. Furthermore, the difference in intensity with respect to $S_1(x,y,\lambda)$ and $S_2(x,y,\lambda)$ of TM_1 and TM_3 (TM_1: $S_{1\_max}(x,y,\lambda) \cong +1$, $S_{2\_max}(x,y,\lambda) \cong +0.25$ and TM_3: $S_{1\_max}(x,y,\lambda) \cong +0.25$, $S_{2\_max}(x,y,\lambda) \cong +0.5$) results in slightly different states of polarization. The spatio-spectrally resolved nSPP $S_3(x,y,\lambda)$ of each transverse mode complements the full polarization analysis in terms of nSPPs(x,y,λ): a positive value between 0 and +0.5 for TM_1, thus reflecting a right-handed circular polarization component, whereas both negative values of TM_2 and TM_3 reflect a left-handed circular polarization. This demonstrates completely different states of polarization of the first three transverse modes TM_1, TM_2 and TM_3 at a pump current of 6mA. Furthermore, no change of sign is observable within one individual transverse mode, as it has been observed already in the previous chapter for the four-lobe structure. Additionally, from the DOP distributions depicted in the bottom row one can clearly observe that the maximal values of the DOP(x,y,λ) of the first three transverse modes are almost close to one, denoting a fully polarized state of light for each transverse mode. These results provide fundamental insight into the polarization behavior of VCSELs namely the complementary and fully polarized states of polarization for each particular transverse mode, thus stimulating theoretical modelling further.

To compare the number values of these results with their corresponding counterparts obtained utilizing a photo detector without a spectrometer, we have spatially integrated the nSPPs(x,y,λ) for each transverse mode over an area of 11x11 pixels, thus providing a numerical value for the nSPPs for each transverse mode, which is comparable to the nSPPs(I_{pump}) obtained utilizing a photo detector only, as it has already been shown at the beginning of chapter 4 (cf. Figure 4.4). We performed SPP(x,y,λ) measurements for each of the first three transverse modes TM_1, TM_2 and TM_3 for eight different values of the injection current starting at 1mA and increase the pump current in steps of 1mA up to 8mA. The spatially integrated nSPPs(x,y,λ) for each of the first three transverse modes together with the DOP all as a function of the pump current are depicted in Figure 6.4a)-c), thus clearly demonstrating their individual emission threshold values of slightly below 1mA, 3mA and 5mA for TM_1, TM_2 and TM_3, respectively. In addition an abrupt rise of the values of the corresponding DOP from very close to zero up to a value of one is found, thus reflecting an unpolarized state of light due to spontaneous emission as well as a fully polarized state of light, respectively.

Furthermore, these results show, an unstable state of polarization in the transverse mode TM_1 as a function of pump current, as clearly indicated by a polarization switch (PS) reflected by a change of sign of the nSPPs S_1 (red plus), S_2 (blue cross) and S_3 (green circle) regarding the fundamental transverse mode when increasing the pump current value from 2mA to 3mA (Figure 6.4 a)). This PS is followed by a gradually change of the state of polarization, basically reflected by the behavior of the nSPPs S_1 (red plus) and S_2 (blue cross) changing their values from 0 up to 1 as well as a complementary behavior from +1 to 0, respectively.

Whereas the nSPP values of S_3 (green circle) remain quite constant only changing its values from +0.4 to +0.2.

A comparable change of the state of polarization is clearly observable in the 2nd order transverse mode TM_2 (Figure 6.4b)). Here, in a range of pump current values between 3mA and 8mA the value of S_3 (green circle) remains constant between -0.4 and -0.3. However, a dramatic change of both the values S_1 (red plus) and S_2 (blue cross) from roughly 0 to -1 as well as from -0.8 up to -0.2, respectively, reflects a change of the orientation of the polarization ellipse by 45°.
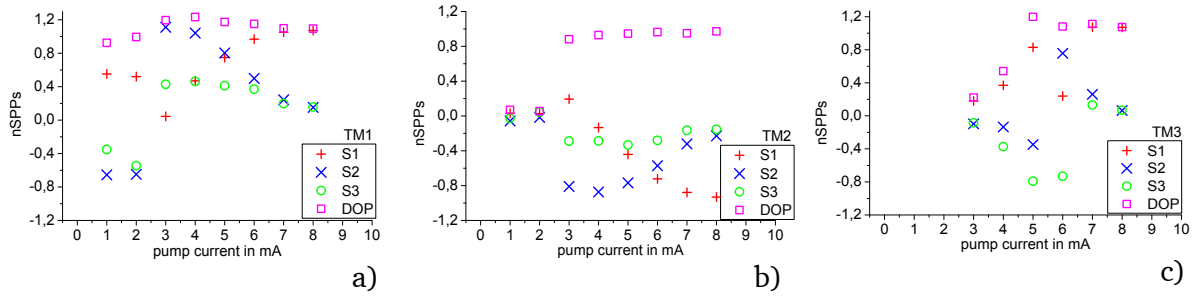
Figure 6.4 Normalized Stokes polarization parameters S_1 (red plus), S_2 (blue cross), S_3 (green circle) together with the DOP (magenta square) of the fundamental transverse mode TM_1 a) the second higher order transverse mode TM_2 b) and the third higher order transverse mode TM_3 c) all as a function of pump current.

The nSPPs(I_{pump}) of TM_3 depicted in Figure 6.4c) uncover a different behavior with two abrupt changes of S_1 (red plus) and S_2 (blue cross) when increasing the pump current value from 5mA to 7mA. Here, S_1 (red plus) and S_2 (blue cross) change their values from +0.8 to +0.2 and from -0.4 up to +0.8, respectively, whereas the nSPP S_3 (green circle) remains constant at a value of -0.8 in a range of the pump current values between 5mA and 6mA. Increasing the pump current value further from 6mA to 7mA the value of the nSPP S_1 (red plus) changes from +0.2 up to +1 and S_2 (blue cross) reduces its value from +0.8 to +0.2, reflecting another dramatic change of the orientation of the polarization. Furthermore, an abrupt reduction of S_3 (green circle) from -0.8, reflecting a large amount of left-handed circular polarization to a pure linear state of polarization with a value of S_3 (green circle) close to zero can be observed. This polarization state is mostly described by a large amount of S_1 (red plus) close to +1 together with a small amount of S_2 (blue cross) of approximately 0.2, thus reflecting a fully (DOP=1) linearly polarized state of light aligned with the horizontal axis.

These results of nSPPs together with the DOP (magenta square) all as a function of pump current regarding the first three transverse modes TM_k with k=1,2,3 show that their state of polarization is fully polarized above their individual thresholds. Furthermore, an individual polarization behavior reflected by a polarization switch and a gradual change of the polarization state as well as a more complex polarization behavior (cf. TM_3 in Figure 6.4c)) has been observed.

However, these results are a contradiction to the reduction of the DOP (magenta square) observable in Figure 6.2 regarding the nSPPs(I_{pump}) of the total emission above a pump current value of 3mA. Therefore, we have to undo the normalization[13] of the nSPPs(I_{pump}) of each transverse mode, thus enabling a reasonable incoherent superposition of each

---

[13] The normalization was performed to enable the comparison of the Stokes polarization parameters for different pump current values due to the different values of their total intensity S_0.

corresponding non-normalized SPPs(I_{pump}) of the first three contributing transverse modes. It is predicted by theory [39] that the Stokes polarization vector $\vec{S}=(S_0\ S_1\ S_2\ S_3)$ consisting of the four SPPs, can be mathematically expressed as the incoherent sum[14] of Stokes polarization vectors $\vec{S} = \sum_k \vec{S}^k$ with k = 1,2,3, ... for the in our case contributing transverse modes TM_k with k=1,2,3. In detail, one has to perform the following calculations with respect to each SPPs and each contributing transverse modes TM_k with k=1,2,3:

$$S_0^{total} = S_0^{TM_1} + S_0^{TM_2} + S_0^{TM_3} \tag{6.1}$$

$$S_1^{total} = S_1^{TM_1} + S_1^{TM_2} + S_1^{TM_3} \tag{6.2}$$

$$S_2^{total} = S_2^{TM_1} + S_2^{TM_2} + S_2^{TM_3} \tag{6.3}$$

$$S_3^{total} = S_3^{TM_1} + S_3^{TM_2} + S_3^{TM_3}. \tag{6.4}$$

These mathematical equations are visualized in Figure 6.5a)-d) showing the SPPs $S_0(I_{pump})$ (black a)), $S_1(I_{pump})$ (red b)), $S_2(I_{pump})$ (blue c)) and $S_3(I_{pump})$ (green d)) of each transverse mode TM_1 (line), TM_2 (dashed line) and TM_3 (dotted line) together with the calculated sum represented by the, in this thesis common, symbols of S_0 (black star), S_1 (red plus), S_2 (blue cross) and S_3 (green circle). These values have been obtained from spatio-spectrally resolved nSPPs representatively depicted in Figure 6.3 at a pump current value of 6mA.
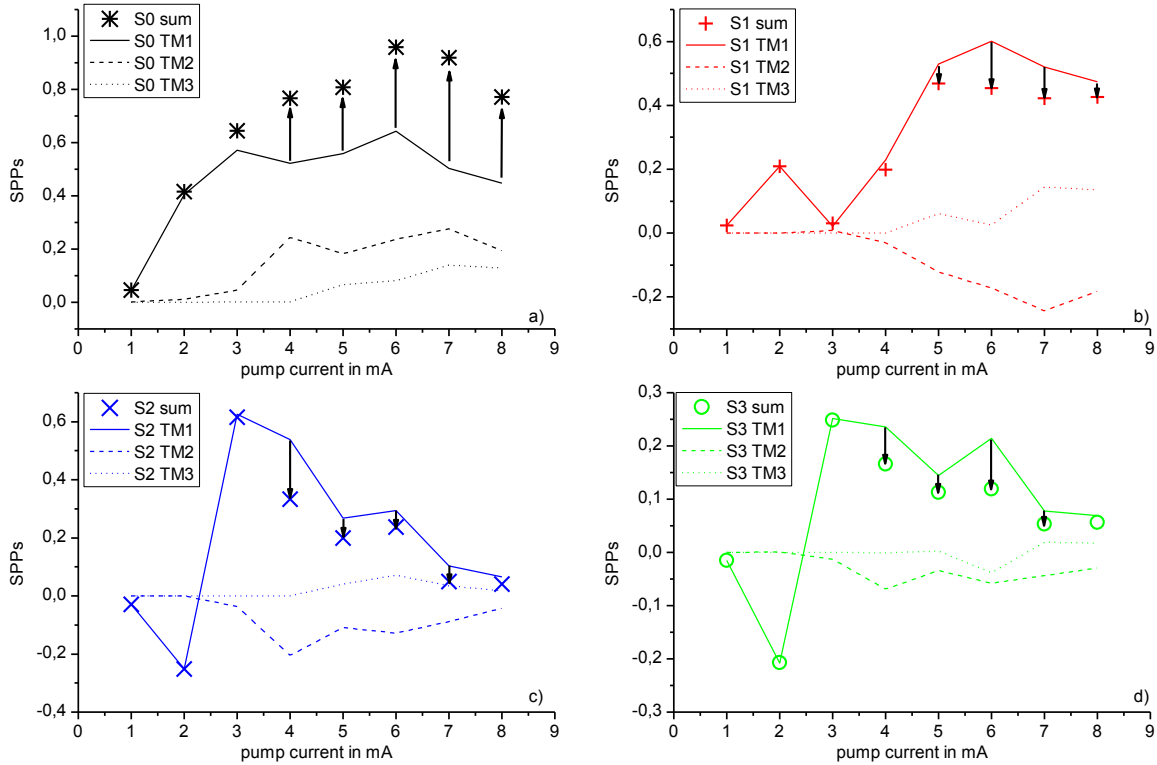

Figure 6.5 Non-normalized Stokes polarization parameters S_0 (black) a), S_1 (red) b), S_2 (blue) c) and S_3 (green) d) of the first three transverse modes TM_1 (full line), TM_2 (dashed line) and TM_3 (dotted line) together with their individual incoherent sum reflected by the color coded well known symbols. The arrows represent the difference of the dominant contribution of the fundamental transverse mode TM_1 (straight line) to the incoherent sum (symbols).

---

[14] Incoherent sum means, that the phase has not to be taken into account.

From these experimentally obtained results the SPP S_0 of TM_1, TM_2 and TM_3 (Figure 6.5 a)), qualitatively reflects their individual P-I characteristics, in arbitrary units including their individual threshold values of 1mA, 3mA and 4mA for TM_1, TM_2 and TM_3, respectively. Furthermore, the dominant contribution of TM_1 over the entire range of pump current values represents the total emitted optical power almost up to a pump current value of 3mA, where the 2nd order transverse mode TM_2 starts contributing to the total emission as well. In contrast to the non-negative values of S_0, the complementary contribution of the first three transverse modes are clearly visible regarding the SPPs S_1, S_2 and S_3 in Figure 6.5b)-d). Here, in a pump current range between 4mA and 8mA complementary contributions of TM_1 (line) and TM_2 (dashed line) (color coded with red, blue and green regarding S_1, S_2 and S_3, respectively) are clearly observable. This results in a reduction of the sum of the SPPs S_1, S_2 and S_3 in comparison with the dominant SPP contribution of TM_1, graphically illustrated by black arrows in Figure 6.5b)-d). The small amount of the SPPs of TM_3 is almost negligible; however, it has been taken into account, thus ensuring that the sum of the SPPs of each contributing transverse mode (symbols) is comparable with the SPPs of the total emission. To make these later results comparable with the obtained results utilizing a photo detector only (without grating spectrometer) a normalization now to the sum of the SPP S_0 (black star) is necessary. The resulting nSPPs (color coded lines) composite of the SPPs of each contributing transverse mode together with the nSPPs (color coded symbols) only obtained via photo detector, are depicted in Figure 6.6. From these results a good coincidence between nSPPs and DOP (measured spatio-spectrally integrated via photo detector) represented by color coded symbols and the nSPPs and DOP (first, spatio-spectrally resolved measured then spatially integrated and incoherently superimposed) represented by color coded lines is clearly visible. The PS at 2.5mA as well as the gradually change of the state of polarization is very well reproduced. Furthermore, the reduction of the DOP above a pump current value of 3mA is observable in the composite nSPPs ($S_i = \sum_{k=1}^{3} S_i^{TM_k}$) and is physically explained by an incoherent superposition of complementary SPPs of different transverse modes. These complementary characteristics have been shown regarding spatio-spectrally resolved nSPPs at a pump current of 6mA in Figure 6.3, nSPPs of each transverse mode as a function of pump current in Figure 6.4a)-c) and SPPs in Figure 6.5a)-d).
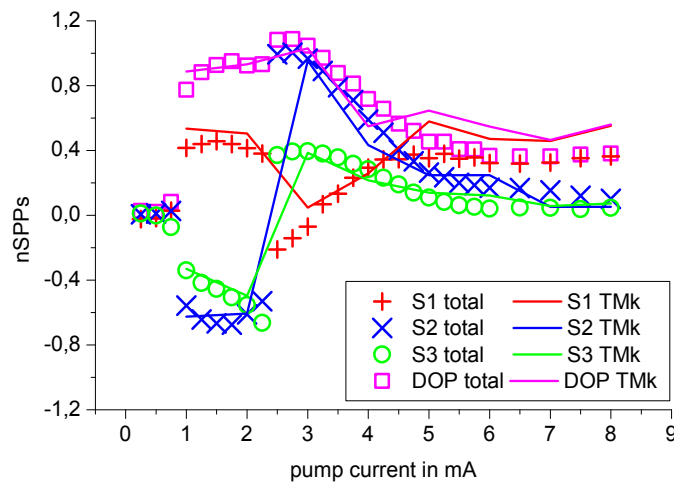

Figure 6.6 Normalized Stokes polarization parameters (color coded symbols) measured utilizing a photo detector only as they are depicted in Figure 6.2, however now in comparison with normalized Stokes polarization parameters determined via calculating the incoherent sum of the (not normalized) Stokes polarization parameters as they are explicitly given in Figure 6.5, normalized to the total emitted optical power (color coded line). These results show good coincidences, including a polarization switch at 2.5mA and a reduction of the DOP above a pump current value of 3mA.

Besides these interesting experimental findings, explaining and complementing the former presented results very well, the spectral resolution of this experimental setup of 50pm at a wavelength of 850nm can be improved even further utilizing a Fourier-Transform Infrared-spectrometer (FTIR-spectrometer) with a spectral resolution roughly 10 times better. This improvement enables even the resolution of polarization modes, which belong pairwise to one transverse mode, and which have been predicted by theory [66], showing the same intensity distributions only slightly shifted in wavelength due to birefringence of the complex VCSEL structure. These polarization modes have already been experimentally observed, however, on a linear polarization projection basis only. The high spectrally resolved Stokes polarization parameters of a transverse multi-mode VCSEL are presented in the next chapter and uncover interesting fundamental facts.

7. High spectrally resolved Stokes polarization parameters SPPs($1/\lambda$)

In the previous chapter spatio-spectrally resolved Stokes polarization parameters (SPPs(x,y,λ)) of a transverse multi-mode VCSEL were presented, uncovering a change of polarization as a function of pump current, both occuring as a polarization switch (PS) and as a gradual change of the state of polarization, observable already even in one particular transverse mode. Due to the restricted spectral resolution of 50pm at a wavelength of 850nm, thus even though enabling the resolution of each particular transverse mode, the polarization behavior of one polarization mode predicted in theory [66] could not be resolved. Therefore, in the present chapter an improved experimental setup is used, such that a grating spectrometer in combination with a CCD camera has been exchanged by a Fourier-Transform Infrared-spectrometer (FTIR-spectrometer), increasing the spectral resolution up to a value of 5pm at 850nm, thus achieving an improvement of the spectral resolution by a factor of 10. The CCD camera could have been removed due to the fact, that in the previous chapter spatial nSPP distributions of higher order transverse modes did not show any change of sign with respect to their different transverse intensity distributions (cf. Figure 6.3). Therefore, high spectrally resolved Stokes polarization parameters (SPPs($\frac{1}{\lambda} = \tilde{\lambda}$)[15]) of the total emission of the, in this chapter, investigated VCSEL (Infineon Technologies) with an oxide aperture diameter of 4μm will provide further insight into the polarization behavior of transverse multi-mode VCSELs, also enabling an improvement of existing theoretical models.
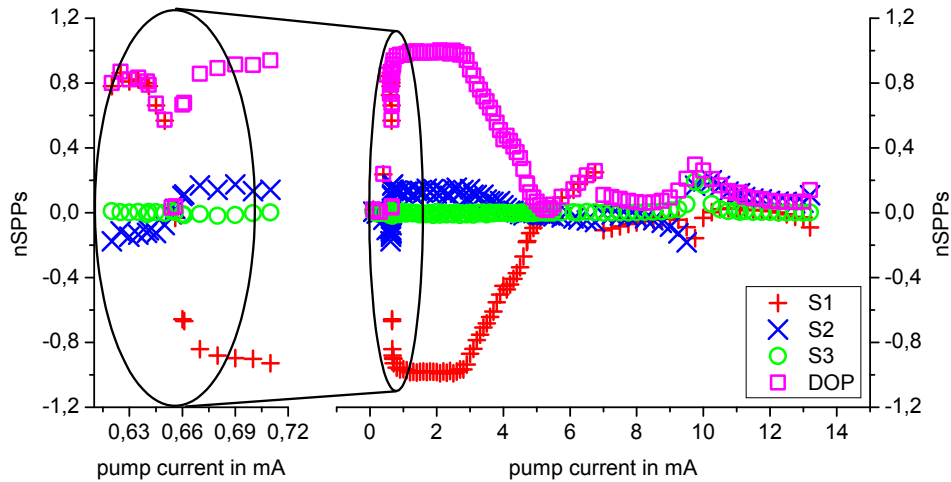

Figure 7.1 Normalized Stokes polarization parameters S_1 (red plus), S_2 (blue cross), S_3 (green circle) together with the DOP (magenta square) of a 4μm device as a function of the pump current, measured using a photo detector only, together with a zoom in, clearly demonstrating the polarization switch at a pump current value of 0.66mA, as well as a complex and interesting development of the nSPPs together with the DOP above 4mA (right).

The here investigated VCSEL (Infineon Technologies) from another company as the VCSELs presented in the previous chapters show very similar results of their nSPPs together with the DOP all as a function of pump current. The nSPPs(I_{pump}) are depicted in Figure 7.1 and have been determined utilizing a linear polarizer, a revolvable quarter-wave plate and a photo detector only. The nSPPs together with the DOP all as a function of pump current uncover a polarization switch below 1mA clearly observable on the left hand side presenting a zoom into

---

[15] ($\frac{1}{\lambda} = \tilde{\lambda}$) this illustrates the relation between the wavelength λ and the wave number $\tilde{\lambda}$.

an interesting pump current value range between 0.63mA and 0.72mA. Here a transition from a state of polarization of S_1=+1 (red plus), S_2=-0.1 (blue cross) and a negligible contribution of S_3 (green circle) of almost zero to S_1=-1, S_2=+0.1 and S_3 close to zero is visible, thus reflecting (due to a change of sign of S_1 and S_2) a rotation of the orientation of the polarization by about 90°. Additionally, a reduction of the value of the DOP (magenta square) from a high value above 0.8 down to a value close to 0 clearly visible at a pump current value of 0.66mA, followed by an increase to a value again of one is observable. In other words, the state of polarization changes from fully linearly polarized with an almost horizontal orientation (below 0.66mA) over a fully unpolarized state of light (at 0.66mA), to an again fully linearly polarized state of light, however now with an almost vertical orientation (above 0.66mA). This fully polarized state of light with an exclusive contribution of S_1=-1 (red plus) is observable up to a pump current value of 3mA in the right part of Figure 7.1. By increasing the pump current further, up to a value of 5mA, the nSPPs S_1 (red plus) and S_2 (blue cross) gradually change their values from -1 to 0 and from +0.1 to 0, respectively. Together with a still very close to zero value of S_3 (green circle) the resulting value of the DOP (magenta square) drops down to a value of zero as well, thus consistently reflecting an unpolarized state of light. In a pump current range between 5mA and 7mA an increase of both the nSPP S_1 (red plus) and the DOP (magenta square) from a value close to 0 up to +0.25 is clearly visible, whereas the nSPPs S_2 (blue cross) and S_3 (green circle) remain constant close to zero. A change of sign of S_1 from +0.25 to -0.1, reflects an abrupt change of polarization. By increasing the pump current up to a value of 10mA both S_1 (red plus) and S_2 (blue cross) decrease in their values from close to 0 to values close to -0.25, whereas the value of the DOP increases to +0.25. Moreover, for the first time a change of the value of S_3 (green circle) from 0 to +0.2 is observable reflecting a small circular component resulting in partially elliptically polarized light. Above a pump current value of 13mA above the thermal rollover, the nSPP values as well as the DOP show a reduction to negligible contributions, thus reflecting an unpolarized state of the VCSEL´s emitted light. From these results the complex polarization behavior of this device is obvious and basically comparable with the results depicted in previous chapters.
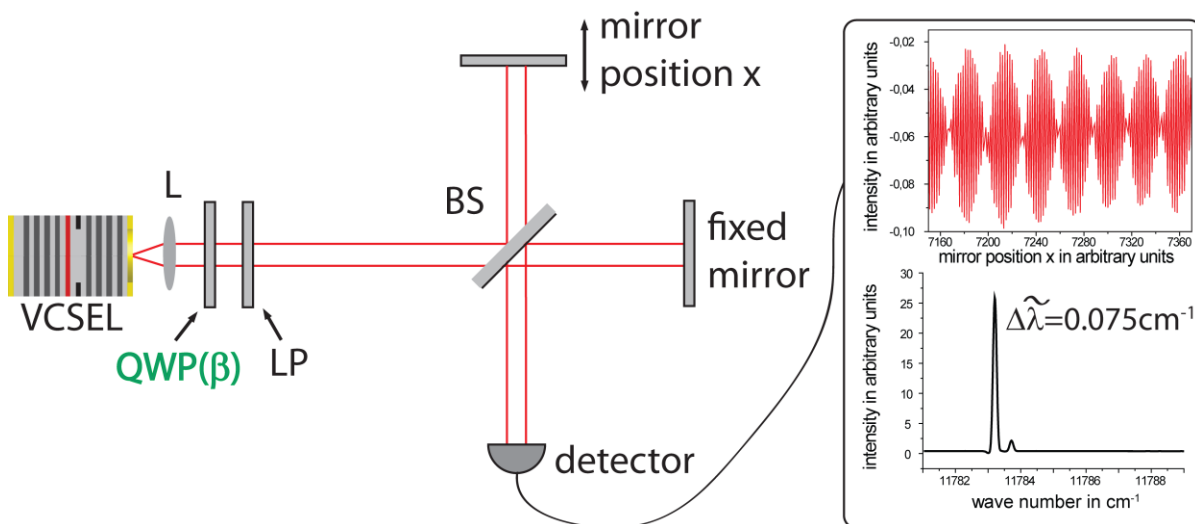

Figure 7.2 (left) Schematic drawing of the experimental setup to obtain high spectrally resolved Stokes polarization parameters. The VCSEL together with the polarization selective optics, flushed with a schematic of a Michelson-Interferometer, which rudimentary depicts the operating principle of a FTIR-spectrometer. Right: An experimentally obtained interferogram (red line, top) together with its Fourier-Transformation, the resulting optical spectra (black line, bottom) with a high optical resolution of 0.075cm^{-1} or 5.5pm at 850nm.

In the following high spectrally resolved nSPPs as a function of pump current are investigated in more detail. Before we start looking at these experimental results, the experimental setup

including the FTIR-spectrometer is presented followed by an announcement of some special features in particular with respect to results presented in posterior chapters of this thesis.

A schematic drawing of the experimental setup is depicted in Figure 7.2(left) with a basic schematic of the FTIR-spectrometer, being the only new component, besides the well known schematic drawing of the VCSEL and the polarization analysis components, thus being the combination of a revolvable quarter-wave plate (QWP) and a fixed linear polarizer (LP). The utilized FTIR-spectrometer (Bruker Vertex 80V) is a research spectrometer capable to cover the spectral range from the far infrared, or terahertz, through the mid and near infrared and visible additionally up to the ultraviolet spectral range by equipping it with corresponding optical components, such as beam splitters (BS) used in the included Michelson-Interferometer as well as detectors measuring the intensity as a function of the displacement of the movable mirror Δx to obtain an interferogram, that can be converted via a Fourier-Transformation into an optical spectrum (see Figure 7.2(right)). This technique, of measuring an interferogram, such that all the spectral components of our investigated light source were measured simultaneously, saves a lot of measurement time in comparison with dispersive or diffractive apparatus like a prism or grating spectrometer, respectively, furthermore providing a high spectral resolution of 0.075cm^{-1}. Additionally to this high spectral resolution, this research tool is capable to perform spectrally and temporally resolved measurements of pulsed light sources simultaneously. This so called step-scan mode enables one to measure spectro-temporally resolved intensity distributions, uncovering a spectral redshift of each particular transverse mode as a function of time. These results amongst others are presented in chapter 9 together with the relevant, more detailed description of the measurement technique.
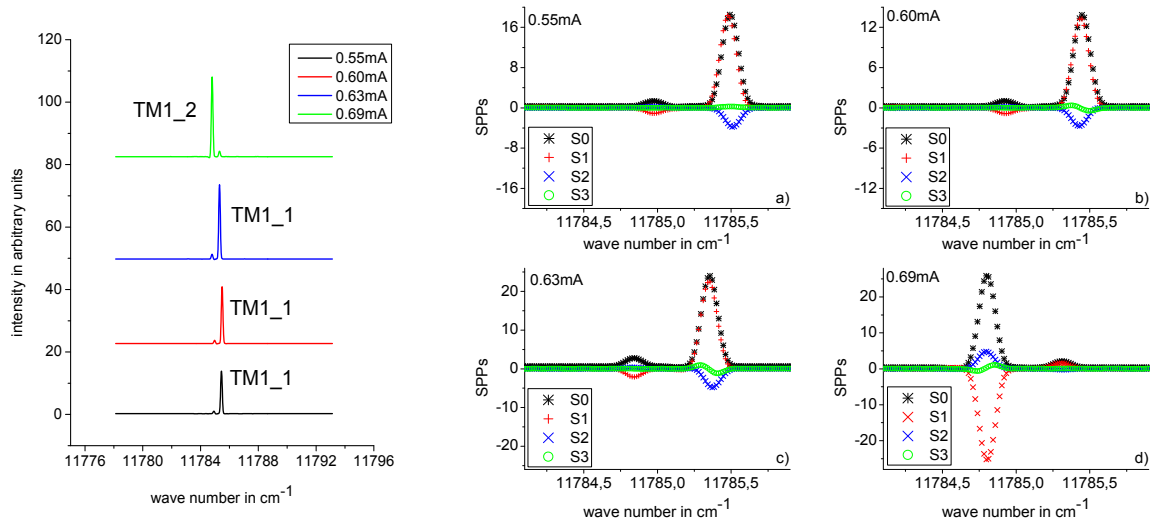

Figure 7.3 (left) Optical spectra of the investigated transverse multi-mode VCSEL at pump current values of 0.55mA (black), 0.60mA (red), 0.63mA (blue) and 0.69mA (green) clearly identifying a switching phenomenon from TM_{1_1} to TM_{1_2} by increasing the pump current value from 0.63mA to 0.69mA. Right: High spectrally resolved Stokes polarization parameters for the corresponding pump current values 0.55mA a), 0.60mA b), 0.63mA c) and 0.69mA d), uncovering the switching phenomenon as well, regarding the total optical power represented by S_0 (black star), however now in combination with a switching of the state of polarization of 90° reflected by the change of sign of S_1 (red plus) and S_2 (blue cross).

The FTIR-spectrometer is operated with a KaliumChlorid (KCl) beam splitter and a Germanium (Ge) detector. The resolution in wavenumber $\tilde{\lambda}$ of 0.075cm^{-1} can be converted into $\Delta\lambda$ via

$$\Delta\lambda = \lambda^2 \Delta\tilde{\lambda} \qquad \Delta\lambda = (850\text{nm})^2 0.075\text{cm}^{-1} \qquad \Delta\lambda = 0.0054\text{nm} = 5.4\text{pm}.$$

With this extremely high optical resolution it is possible, to resolve the two polarization modes within the fundamental Gaussian-shaped transverse mode, that have been camouflaged until now by the low optical resolution of the utilized experimental setup presented in chapter 6, consisting of a grating spectrometer in combination with a CCD camera achieving only an optical resolution of 50pm at 850nm.

The highly resolved optical spectra in a pump current range between 0.5mA and 0.7mA are depicted in Figure 7.3(left), showing the intensity in arbitrary units as a function of the wave number $\tilde{\lambda}$ in units of cm^{-1} at four different pump current values of 0.55mA (black line), 0.60mA (red line), 0.63mA (blue line) and 0.69mA (green line), each shifted by an individual intensity offset for the sake of clarity. The two polarization modes are denoted with TM_{1_1} and TM_{1_2} and well separated by a difference in wave number of $0.51cm^{-1}$ (in wavelength 37pm). The presented optical spectra reflect a mode switching by increasing the pump current above a value of 0.63mA, due to a shift of the gain curve of the VCSELs active zone specific material of GaAs with respect to the two polarization modes, thus leading to a PS type I as it has been explained in chapter 2 and [67]. To complement these findings high spectrally resolved SPPs $(SPPs(\tilde{\lambda}))$ are depicted in Figure 7.3(right) as a function of the wave number $\tilde{\lambda}$ and have been determined for the above mentioned pump current values. These $SPPs(\tilde{\lambda})$ have been obtained by measuring highly resolved optical spectra, such as they are depicted in Figure 7.3(left), for a complete set of the rotation angle β of the quarter-wave plate in combination with a fixed linear polarizer. From these results the $SPPs(\tilde{\lambda})$ have been extracted, performing a multi-parameter fit according to each data point with respect to the wave number. These results clearly show the linear polarization character of these two polarization modes TM_{1_1} and TM_{1_2}, with a negligible amount of $S_3(\tilde{\lambda})$ (green circle) very close to zero, however, with contributions of both $S_1(\tilde{\lambda})$ (red plus) and $S_2(\tilde{\lambda})$ (blue cross), reflecting a small misalignment of the orientation of the linear polarization with respect to the crystaline axis of the VCSEL. Moreover, the SPP $S_0(\tilde{\lambda})$ (black star) reflects the total emitted intensity, nicely reproducing the measured optical spectra depicted in Figure 7.3(left), including the switching phenomena observed by increasing the pump current value from 0.63mA up to 0.69mA. Furthermore, the state of polarization remains within each polarization mode (TM_{1_1} and TM_{1_2}) for different pump current values. This finding in combination with the spectral switching phenomena results in the polarization switch and is observable from Figure 7.1(left). To make these findings more obvious, the $nSPPs(\tilde{\lambda})$ of these two polarization modes TM_{1_1} and TM_{1_2}, together with the $nSPPs(\tilde{\lambda})$ obtained by calculating their incoherent sum, such as it has been done in the previous chapter, are depicted in Figure 7.4c) all as a function of pump current. These results clearly disclose that the state of polarization for each polarization mode TM_{1_1} and TM_{1_2} is conserved even when increasing the pump current. Moreover, the PS is clearly observable in Figure 7.4c) where the incoherent sum of the $SPPs(\tilde{\lambda})$ of TM_{1_1} and TM_{1_2}, is depicted.
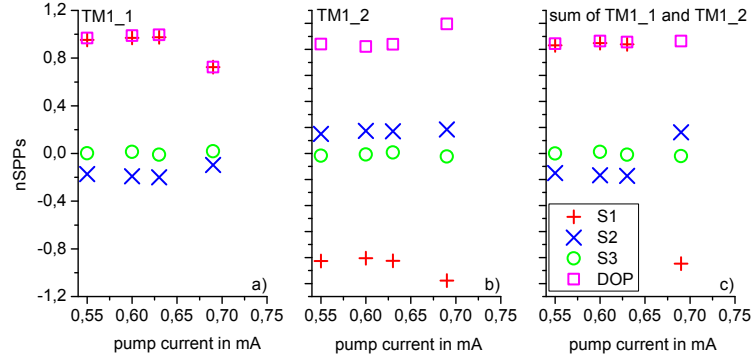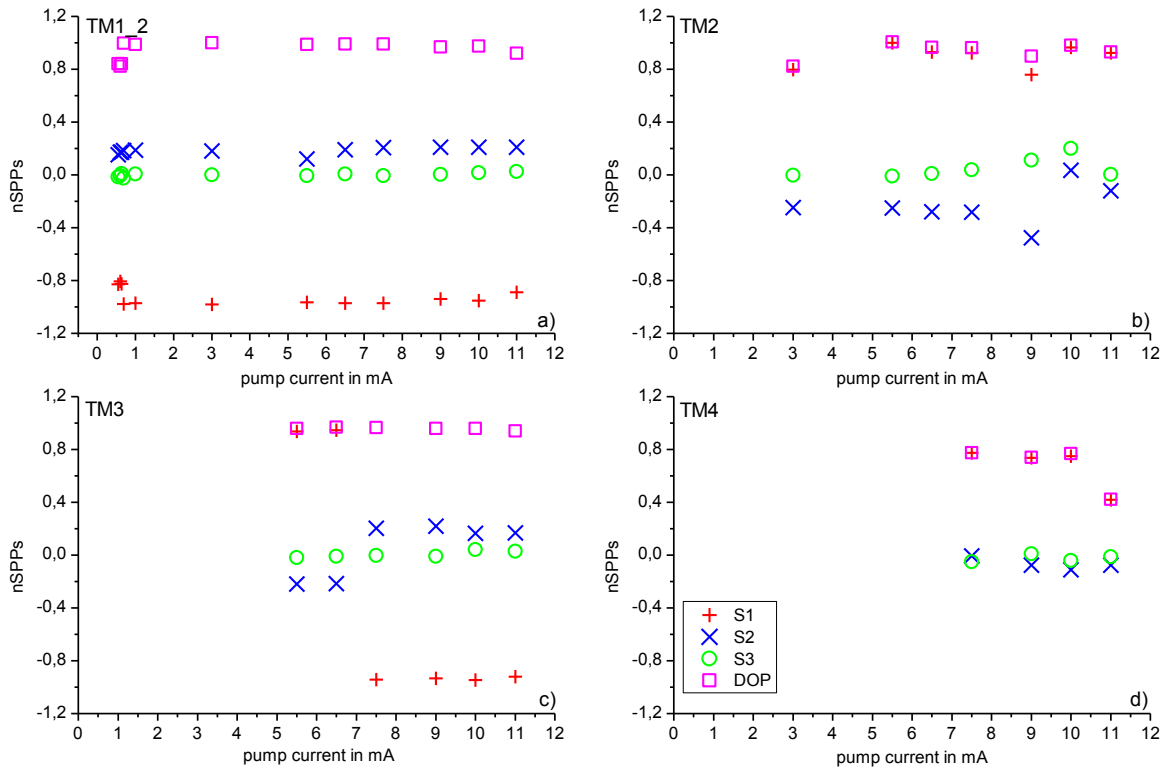
Figure 7.4 Normalized Stokes polarization parameters as a function of the pump current of TM_{1_1} a), TM_{1_2} b), taken from the maxima peak values of the spectrally resolved results from Figure 7.3, together with their incoherent sum c) uncovering the resulting polarization switch, reflected by the change of sign of S_1 (red plus) and S_2 (blue cross).

The experimental results of $nSPPs(\tilde{\lambda})$ on TM_{1_1} and TM_{1_2} (Figure 7.4a) and b)) uncover a well known (cf. Figure 7.3(right)) fixed linearly polarized state of light with a horizontal and a vertical orientation, respectively. With the resulting DOP values close to one, TM_{1_1} shows a fully polarized state of light, up to a pump current value of 0.63mA and dominates the emission. In contrast to this the DOP of the less contributing transverse mode TM_{1_2}, has a value of roughly 0.85. The DOP values of TM_{1_1} and TM_{1_2} are changing their values from 1 to 0.7 and from 0.85 to 1, reflecting the polarization switching event. The $nSPPs(\tilde{\lambda})$ of the incoherent sum of the $SPPs(\tilde{\lambda})$ of TM_{1_1} and TM_{1_2} are depicted in Figure 7.4c) and uncover a change of sign of S_1 and S_2, reflecting a PS as well. The value of the DOP of roughly 0.85 (slightly below 1) is in agreement with the DOP value experimentally obtained via a photo detector only, observable in Figure 7.1c). The reduction of the DOP at a pump current value of 0.66mA in Figure 7.1c) is due to the fact that both polarization modes TM_{1_1} and TM_{1_2} exhibit complementary states of polarization, in combination with an equal power contribution at a pump current of 0.66mA.

In the following the $nSPPs(I_{pump})$[16] of the first three mainly contributing transverse modes TM_{1_2}[17], TM_2 and TM_3 together with the less contributing TM_4 all as a function of pump current are discussed together with their individual peak intensities in arbitrary units. In Figure 7.5a) are depicted the $nSPPs$ of TM_{1_2}, thus showing a constant linearly polarized state of light with a vertical orientation of the polarization plane, reflected by a large amount of S_1 (red plus) in combination with a small amount of S_2 (blue cross) and a negligible contribution of S_3 (green circle) close to zero. Because of the constant contributions of S_1, S_2 and S_3 the resulting DOP (magenta square) remains constant as well, except at a pump current range below 1mA, where the DOP value is roughly 0.85 as it has been already shown in Figure 7.4b) and explicitly discussed above. The next graph in Figure 7.5b) exposes $nSPPs$ together with the DOP as a function of pump current for the second higher order transverse mode TM_2, showing a constant state of polarization up to the thermally induced rollover, reflected by nSPP values of $S_1 \approx +1$, $S_2 = -0.3$, $S_3 = 0$ as well as DOP > 0.9. However, at a pump current of 9mA the state of polarization changes abrupt in combination with a decrease of the value of S_1 from +1 to +0.8 and of S_2 from -0.3 to -0.5, reflecting a rotation of the orientation of the linear polarization. Furthermore, an increase of the value of S_3 is clearly observable with a maximum value of +0.2 at a pump current value of 10mA (rollover), followed by a change of

---

[16] In the following the notation (I_{pump}) is omitted for the sake of clarity.

[17] TM_{1_1} is essentially contributing to the total emission only up to 0.63mA. Above this pump current value we only take polarization mode TM_{1_2} into account and call it in the following transverse mode for the sake of clarity.

sign of S_2 from -0.5 to +0.1 and an decrease of the value of S_1 close to one representing the dominant contribution to a high linear degree of polarization. However, now a non-negligible amount of S_3 indicates a circular component, thus resulting in an elliptical state of polarization. In contrast to this, an abrupt change of sign of the nSPP values of TM_3 uncovering a PS as we have already seen, regarding the polarization behavior of the sum of TM_{1_1} and TM_{1_2} in Figure 7.4c). Here, in Figure 7.5c) the state of polarization changes from fully linearly almost horizontally polarized, reflected by S_1=+1 and S_2=-0.3, to a fully linearly almost vertically orientated polarization reflected by S_1=-1 and a small contributing value of S_2=+0.2, when increasing the pump current above 6.5mA. The last graph in this figure (Figure 7.5d)) showing the nSPPs of the fourth transverse mode TM_4, represent a constant state of linear polarization, aligned with the horizontal axis, represented by a dominant contribution of S_1 and negligible values of S_2 and S_3 being in the range between -0.1 and +0.1. In addition, a reduced value of the DOP of 0.8 at 7.5mA, 9mA and 10mA is clearly observable, complemented by a DOP value even below 0.5 at 11mA reflecting a predominantly unpolarized state of light, due to the very small contribution of TM_4, observable in Figure 7.6a), where the maximal peak intensities of each particular transverse mode as a function of pump current are depicted.

Figure 7.5 Normalized Stokes polarization parameters as a function of pump current of TM_{1_2} a), TM_2 b), TM_3 c) and TM_4 d) taken from the maxima peak values of their high spectrally resolved counterparts. These results uncover the individual polarization behavior of each particular transverse mode, including another polarization switching event regarding TM_3, as it is explained in the text.

Furthermore, individual threshold pump current values of each particular transverse mode TM_{1_2} (black), TM_2 (red), TM_3 (blue) and TM_4 (green) are clearly visible from Figure 7.6a), being roughly 1mA, 3mA, 4mA and 6.5mA, respectively. Moreover, two crossing points of the intensities as a function of pump current according to TM_{1_2}, TM_2 and TM_3 are clearly observable at pump current values of 8mA and 9mA. In addition, above a pump current value of 8mA the intensity of the dominant fundamental transverse mode TM_{1_2} (black line) is below the intensity of the second higher order transverse mode TM_2 (red line) and the peak intensity of TM_{1_2} (black line) is even below the intensity values of the third higher order

transverse mode TM_3 (blue line) above a pump current value of 9mA. This change of dominance of the fundamental transverse mode TM_{1_2} from being dominant up to a pump current value of 7mA to a weak contribution of even half the intensity of the dominant TM_2, results in transverse mode competition, which could be the reason for the abrupt change of the state of polarization of TM_2. Additionally, the almost negligible contribution of TM_4 (green line) is depicted in this graph and uncovers the transverse mode individual threshold of 6.5mA in combination with a very small value of intensity.

a)   b)
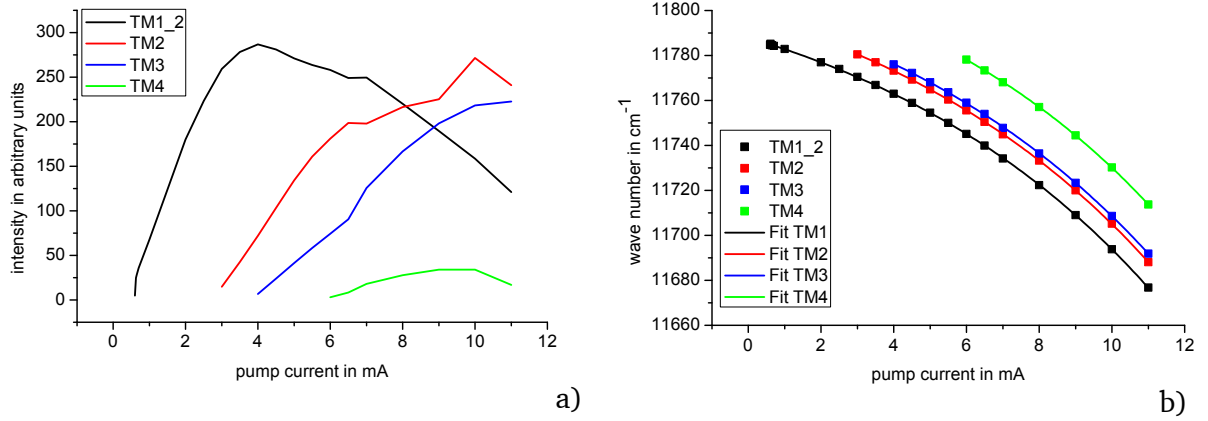
Figure 7.6 a) Maximum intensity of TM_{1_2} (black line), TM_2 (red line), TM_3 (blue line) and TM_4 (green line) as a function of pump current, identifying the threshold current values of each transverse modes and furthermore the dominant pump current regimes of TM_{1_2} up to 7mA followed by the dominant operation regime of TM_2 and TM_3 above 9mA. The wave number in cm^{-1} of the peak intensities as a function of the pump current of TM_{1_2}, TM_2, TM_3 and TM_4 (with the same color code) as a function of the pump current are depicted on the right side b). In addition a mathematical fit (color coded line) following the equation (7.1) uncovers similar behavior regarding the spectral redshift in wave number as a function of the pump current of the four contributing transverse modes.

Beside the intensity of each transverse mode, their individual position in wave number has been recorded and plotted as a function of pump current in Figure 7.6b), thus showing a redshift in wave number with increasing pump current. In addition equation (7.1) has been fitted to the experimentally obtained data of TM_{1_2} (black dot), TM_2 (red dot), TM_3 (blue dot) and TM_4 (green dot)

$$\tilde{\lambda}(I_{pump}) = \tilde{\lambda}_a * \exp\left(-\frac{I_{pump}}{I_{sp}}\right) + \tilde{\lambda}_f. \tag{7.1}$$

Here $\tilde{\lambda}(I_{pump})$ is the absolute wave number as a function of the pump current I_{pump}, $\tilde{\lambda}_a$ is a wave number quantifying the spectral redshift and finally $\tilde{\lambda}_f$ is a wave number offset. The parameter values obtained from the fitting routine are summarized in Table 7.1, showing of course a different wave number offset $\tilde{\lambda}_f$ with respect to the individual transverse modes TM_{1_2}, TM_2, TM_3 and TM_4, of 11829.17cm^{-1}, 11839.17cm^{-1}, 11842.74cm^{-1} and 11851.33cm^{-1}, respectively. However, the wave number $\tilde{\lambda}_a$ of the first three transverse modes is in the range between -41.15cm^{-1} and -41.65cm^{-1}, showing the same values within the given standard error. However, a small deviation of these results can be observed regarding the amplitude of TM_4 being -34.39cm^{-1} such that this value differs from the others by about 30%. In comparison to these values, the shift parameter I_{sp} is in the range between 8.4mA and 8.55mA for the first three transverse modes TM_{1_2}, TM_2, TM_3 and only reduced by approximately 15% regarding the fourth higher order transverse mode TM_4. At this point one cannot clearly say whether this value difference has a physical meaning or results from the limitation that we can only take a few data points into account performing the exponential decay fit. Still, the coincidence of the fitting parameters depicted in Table 7.1 for the first three transverse modes TM_{1_2}, TM_2 and TM_3, which means that one constant redshift parameter if valid for each particular

transverse mode, would simplify theoretical models with the aim to simulate transverse multi-mode VCSELs.

		TM_{1_2}	TM_2	TM_3	TM_4
$\tilde{\lambda}_f$	wave number offset	11829.17cm^{-1}	11839.17cm^{-1}	11842.74cm^{-1}	11851.33cm^{-1}
	standard error of $\tilde{\lambda}_f$	0.49cm^{-1}	0.66cm^{-1}	2.60cm^{-1}	2.31cm^{-1}
$\tilde{\lambda}_a$	amplitude	-41.17cm^{-1}	-41.14cm^{-1}	-41.65cm^{-1}	-34.39cm^{-1}
	standard error of $\tilde{\lambda}_a$	0.43cm^{-1}	0.54cm^{-1}	2.05cm^{-1}	1.65cm^{-1}
I_{sp}	shift parameter	-8.40mA	-8.46mA	-8.55mA	-7.93mA
	standard error of I_{sp}	0.05mA	0.06mA	0.22mA	0.18mA

Table 7.1 The obtained fitting parameter $\tilde{\lambda}_f$: wave number offset, $\tilde{\lambda}_a$: amplitude, and $\tilde{\lambda}_{sp}$: shift parameter together with their individual standard errors are given for TM_{1_2} (black), TM_2 (red), TM_3 (blue) and TM_4 (green).

The observed spectral redshift is depicted on a relative large scale in wave number of roughly 100cm^{-1} (in wavelength about 7.26nm), this kind of representation is improper to benefit from the high spectral resolution and to observe spectral shifts on small scales, as they have been observed already regarding the fundamental transverse mode, which performed a spectral jump in wave number of less than 1cm^{-1}. Therefore, the difference in wave number of the transverse modes TM_{1_2}, TM_2 and TM_3 as a function of pump current has been calculated from the values of Figure 7.6b) and is depicted in Figure 7.7a) on a smaller scale in wave number (10 times in comparison with Figure 7.6b)). The differences in wave number of TM_{1_2} and TM_2 (blue triangle), TM_2 and TM_3 (red dot) as well as TM_{1_2} and TM_3 (black squares) are showing a linear dependence on wave number difference. However, both the results of the differences of TM_{1_2} and TM_3 as well as TM_2 and TM_3 show a clearly observable kink at a pump current value between 6.5mA and 7mA. This observation in combination with the straight result of the differences of TM_{1_2} and TM_2 showing no kink, proposes a kink in wave number of TM_3 when increasing the pump current above 6.5mA. The size of the kinks regarding the differences of TM_{1_2} and TM_3 as well as TM_2 and TM_3 have been determined to be 0.36cm^{-1} and 0.54cm^{-1}, respectively, thus resulting in a shift in wavelength of 36pm, being in the same range as the amount of spectral polarization mode switch which has been observed for the two polarization modes TM_{1_1} and TM_{1_2} of the fundamental transverse mode TM_1 (cf. Figure 7.5). This abrupt change in wave number to a smaller value is the physical explanation of the PS of TM_3 clearly observable in Figure 7.5c), thus showing for the first time a PS type I even for a higher order transverse mode and confirms the existence of the polarization modes of TM_{3_1} and TM_{3_2}.
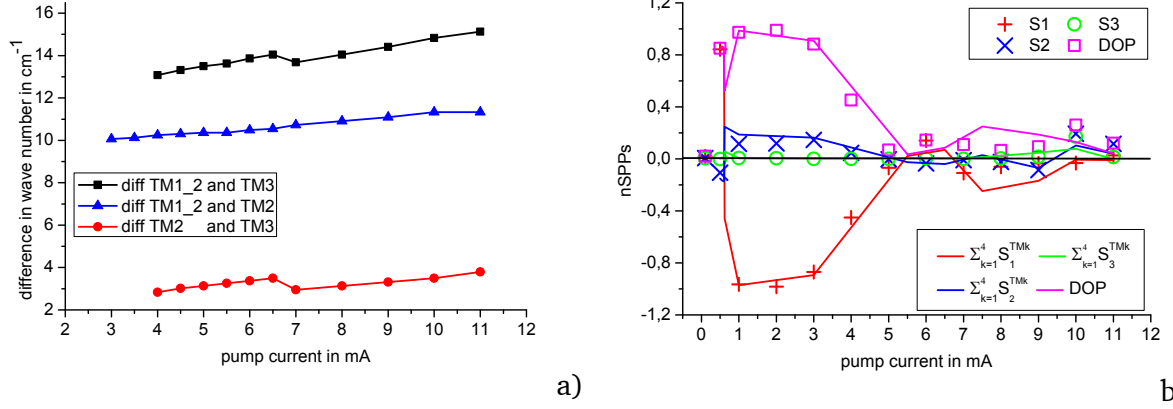
Figure 7.7 a) Wave number difference of TM_1 and TM_2 (blue triangle-line), TM_2 and TM_3 (red dot-line) as well as TM_1 and TM_3 (black squares-line), uncover the switch in wave number of TM_3 clearly visible from the black and the red color coded results at a pump current value of 7mA. b) Normalized Stokes polarization parameters (color coded symbols) measured utilizing a photo detector only as they are depicted in Figure 7.1, here in comparison with the normalized Stokes polarization parameters determined via calculating the incoherent sum of the Stokes polarization parameters of each particular transverse mode, normalized to the total emitted optical power (color coded line).

The resulting nSPPs (color coded lines) calculated via the incoherent sum of the SPP of each particular transverse mode TM_1, TM_2, TM_3 and TM_4 as it has been shown in chapter 6, are depicted in Figure 7.7b) in comparison with the nSPPs (color coded symbols) of the total emission (not spectrally resolved and recorded via a photo detector only). The PS at a pump current value below 1mA is nicely seen by the red line showing a change of sign of S_1 from +1 to -1. Furthermore, up to a pump current value of 5mA the nSPPs S_1, S_2 and S_3 together with the DOP are in good coincidence with the incoherent sum of the SPP of each individual transverse mode represented by the color coded lines. Above a value of 6mA the behaviour is basically described by the changes of sign of S_1 (red) in a pump current range between 5mA and 7mA as well as of S_2 (blue) from negative to positive at 10mA. Furthermore, an increase of the circular component is reflected by S_3 (green) at a pump current value of 11mA also visible from the green line showing its maximum positive value here. These results show a good coincidence of the nSPPs of the total emission and the reconstructed nSPPs calculated from the SPPs of each particular transverse mode, including the demonstration of the polarization switch below 1mA and the reduction of the DOP above a pump current value of 3mA, due to complementary SPP contributions, according to each particular transverse mode.

These results of high spectrally resolved Stokes polarization parameters uncover the states of polarization of each particular transverse mode and in addition their associated polarization modes, including the PS and the thermal effect at the VCSEL´s characteristic rollover. Furthermore, a rigorous analysis of the optical spectra with respect to the first four transverse modes reveals an equal transverse mode spacing together with a characteristic redshift in wave number as a function of pump current. These findings deliver fundamental information on the transverse mode behavior, thus improving theoretical modelling of transverse multi-mode VCSELs even further.

Up to now the results presented in this thesis have been measured, while the VCSELs were in continuous wave (CW) operation, however, for data communication applications, a pulsed operation mode is necessary, together with a reliable and stable performance of the polarization. Therefore, time-resolved Stokes polarization parameters of VCSELs are investigated in the next chapter. These time-resolved results on a microsecond timescale reveal very interesting coincidences between the pulsed and the continuous wave operation mode.

High spectrally resolved Stokes polarization parameters SPPs($1/\lambda$)

8. Time-resolved Stokes polarization parameters SPPs(t)

In contrast to the results presented in the previous chapters, where VCSELs have been driven by a continuous wave injection pump current, now we are turning to time-resolved polarization dynamics of pulsed VCSELs on a microsecond timescale. We are not interested in the turn-on dynamics, being on a sub-nanosecond timescale, but on time-resolved polarization behavior at the transition to quasi continuous wave (CW) operation, thus enabling a comparison of SPPs obtained via a slow photo detector (integrating the intensity over hundreds of milliseconds) uncovering constant SPP contributions only. In the present chapter, we utilize the same transverse multi-mode VCSEL as in the previous chapter, where high spectrally resolved Stokes polarization parameters have been presented, thus enabling a comparison of the polarization behavior in CW and pulsed operation. As it is well known from [19], VCSELs exhibit repetitive dynamics, thus enabling the applications of a simplified experimental setup.

This chapter is organized in the following way; first an experimental setup is presented utilizing a fast photo detector in combination with a broadband amplifier, thus enabling measurements of both CW as well as pulsed operation. After that, time-resolved Stokes polarization parameters (SPPs(t)) of the VCSEL under different pulse conditions are presented together with particular emphasis on time-resolved SPPs at a polarization switch, which has been intensively discussed in literature [68] [69] and in the previous chapter. Finally, a comparison of nSPPs as a function of pump current and nSPPs as a function of time, for a reasonable pumping voltage, will reveal interesting insights with the potential to extend theoretical modeling (valid on a picosecond timescale [70] and nanosecond timescale [71] [72]) on a larger timescale to explain phenomena on a microsecond timescale as well.
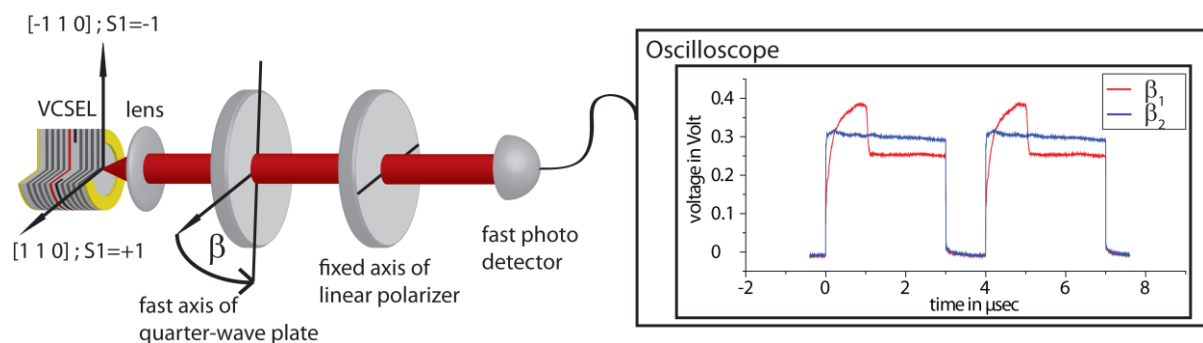
Figure 8.1 (left) Schematic drawing of an experimental setup including a VCSEL with the orientation of its crystaline axis, the collimation lens and the polarization selective optics to perform polarization analysis. The collimated beam of light is detected by a fast photo detector in combination with a signal amplifier, connected to an oscilloscope depicted on the right. The inset of the schematic of the oscilloscope (right) shows two representative sets of data (represented in blue and in red) for two different rotation angles β_1 and β_2 of the quarter-wave plate, respectively. These signals as a function of the pulse duration time t in microseconds give a first idea that the state of polarization changes as a function of time even on a microsecond timescale.

An experimental setup to perform time-resolved measurements is depicted in Figure 8.1. Instead of a continuous wave operating current source, we used a pulse generator (HP Pulse

Generator 8110 A) to induce short current pulses to the VCSEL. The fast photo detector (Hamamatsu S5972) with a high-speed response up to 500MHz placed subsequently to the polarization selective optics in combination with an appropriate amplifier with a frequency response from 0Hz up to 300MHz, and an oscilloscope (Tektronix TDS 3032) provides a sufficient time resolution of at least one nanosecond. The right part of Figure 8.1 illustrates the detected voltage[18] for two different rotation angles β_1 (red line) and β_2 (blue line), as a function of time on a microsecond scale. These two representative sets of data points with a constant contribution (blue line) and a in some sense modulated signal (red line), give a first hint that SPPs(t), obtained by performing the multi-parameter fit at each time step, will uncover a dynamic as a function of time.

However, before time-resolved results of a VCSEL in pulsed operation are presented, the results of continuous wave VCSELs, measured via the experimental setup depicted in Figure 8.1 are compared with the results that have been shown in the previous chapter using a slow photo detector (integrating over several hundred of milliseconds) only. Within this approach the new detection system, consisting of the fast photo detector in combination with a broadband amplifier connected to an oscilloscope, can be crosschecked by comparing the nSPPs for these two cases at a pump current of 2mA and 4mA, depicted in Figure 8.2a). Both time-resolved results, show a time-independent state of polarization, with nSPP values of $S_1=-1$ (red plus), $S_2=+0.2$ (blue cross), $S_3=0$ (green circle) and a DOP=1 (magenta square) at a pump current value of 2mA as well as $S_1=-0.45$ (red plus), $S_2=+0.1$ (blue cross), $S_3=0$ (green circle) and the DOP=0.45 (magenta square) at a pump current of 4mA. These experimental results are in excellent agreement with the results depicted in Figure 8.2b) regarding the same pump current values marked together with the nSPPs utilizing black frames. This comparison demonstrates the correct functionality of the new detection system, thus guaranteeing correct time-resolved investigations on VCSELs presented in the following.
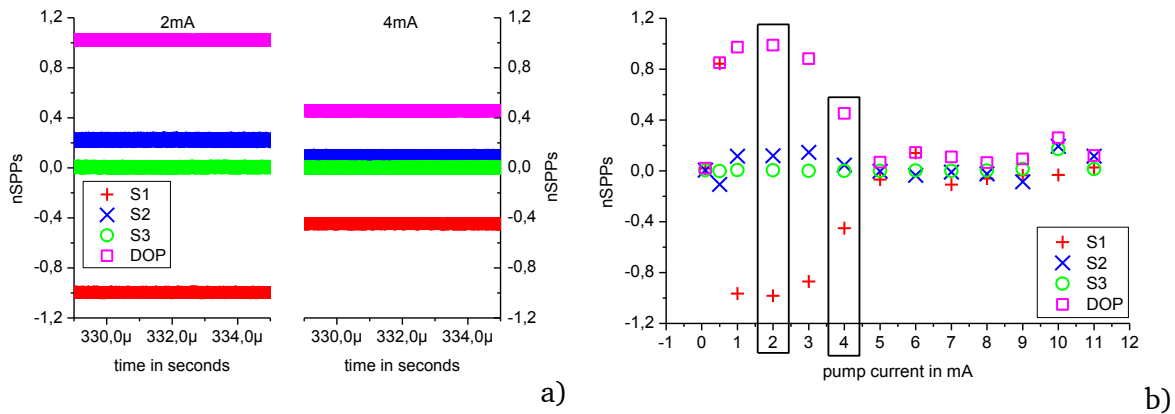

Figure 8.2 a) Normalized Stokes polarization parameters S_1 (red plus), S_2 (blue cross), S_3 (green circle) together with the DOP (magenta square) for two different continuous wave operation conditions with pump current values of 2mA (left) and 4mA (right) as a function of time, in comparison with the results of nSPPs S_1 (red plus), S_2 (blue cross), S_3 (green circle) together with the DOP (magenta square) obtained utilizing a slow photo detector (integrating over a microsecond timescale) depicted as a function of pump current b).

---

[18] It is shown later, that the detected voltage corresponds to the detected intensity.

Such a constant behavior of polarization (as a function of time) depicted in Figure 8.2a) is observable over the total pump current range, except for the pump current regime around a value of 0.66mA, where a PS has been observed. Here, the measured signal[19] randomly switches between 0V and 0.2V, as depicted in Figure 8.3. This non-repetitive signal prevents a time-resolved SPP(t) analysis under this pumping condition. However, a further analysis of these signals, by calculating their autocorrelation function will uncover the timescale on which a stable state of polarization is observable. A comparison of these results with existing results on time-resolved PS experiments on VCSELs in [69] and [73], the different states of polarization will be identified despite the non-repetitive character of the signal.
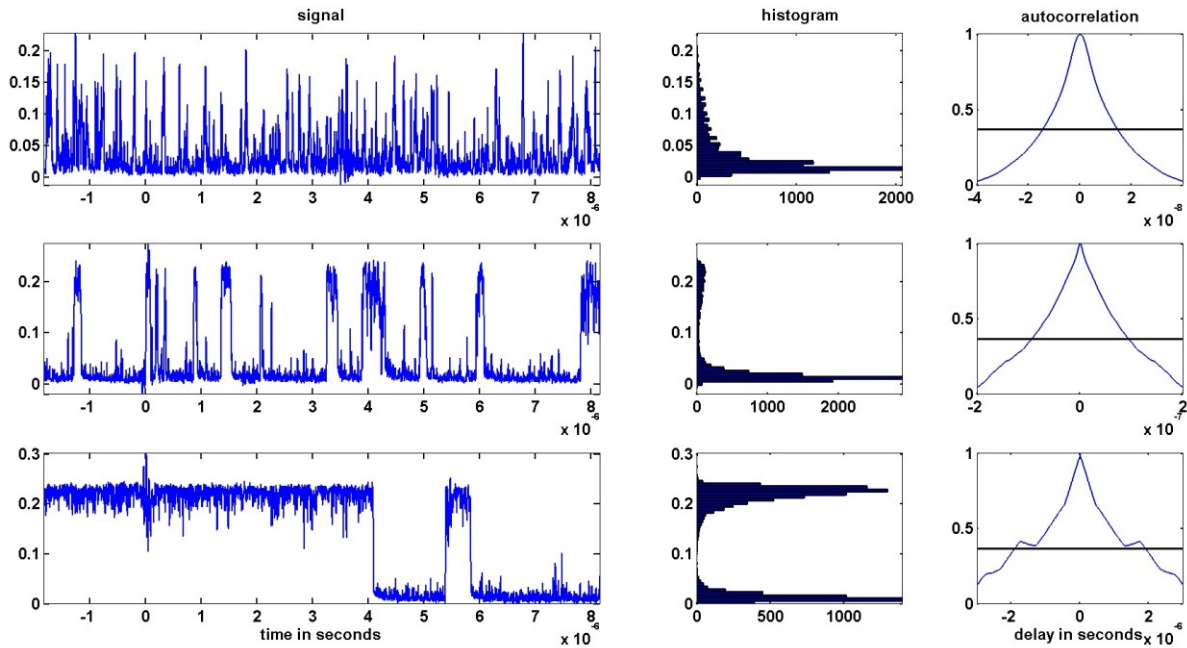
Figure 8.3 (left) Three single-shot measurements of an optical signal (blue line) as a function of time in microseconds, illustrating polarization switching events on different timescale. The histograms with respect to each signal are given in the middle of this figure, representing the voltage values of the signal as a function of the absolute frequency, giving a trend of how long the state of polarization takes one value or the other. The corresponding autocorrelation functions are depicted on the right hand side, reflecting their individual decay from 1 to a value below 1/e after different times, such as 20ns (top), 100ns (middle) and 1μs (bottom).

The non-repetitive time-resolved signals at the PS depicted in Figure 8.3(left) clearly demonstrates, that the PS could happen on different timescales, namely short (top), middle (middle) and long (bottom). These signals have been measured utilizing a fixed linear polarizer and a fixed quarter-wave plate as well. Additionally to the direct measured signals (left), corresponding histograms are depicted to the right and give the amount of data points representing a specific voltage value between 0V and 0.25V. This gives an idea of the ratio of the polarization state being in the one or in the other state of polarization, respectively. Furthermore, the autocorrelation functions of the three representative signals (top, middle and bottom) are depicted in the right part of Figure 8.3. They decay below a value of 1/e, represented by a horizontal black line, on different timescales of 20ns (top), 100ns (middle) and 1μs (bottom). These results are in line with [68], demonstrating that the time between polarization switching events can be found on timescales in a range as large as eight orders of magnitude. An exclusive theoretical ansatz in combination with coherency theory can be found in [74]. Moreover, these two coexisting polarization states can be controlled all-

---

[19] The signal represents a single-shot (without average) intensity measurement for one angle β of the revolvable quarter-wave plate.

optically by exposing the device to polarization selective feedback, to crossed polarization reinjection or by injecting external light pulses as it is reported in [75].
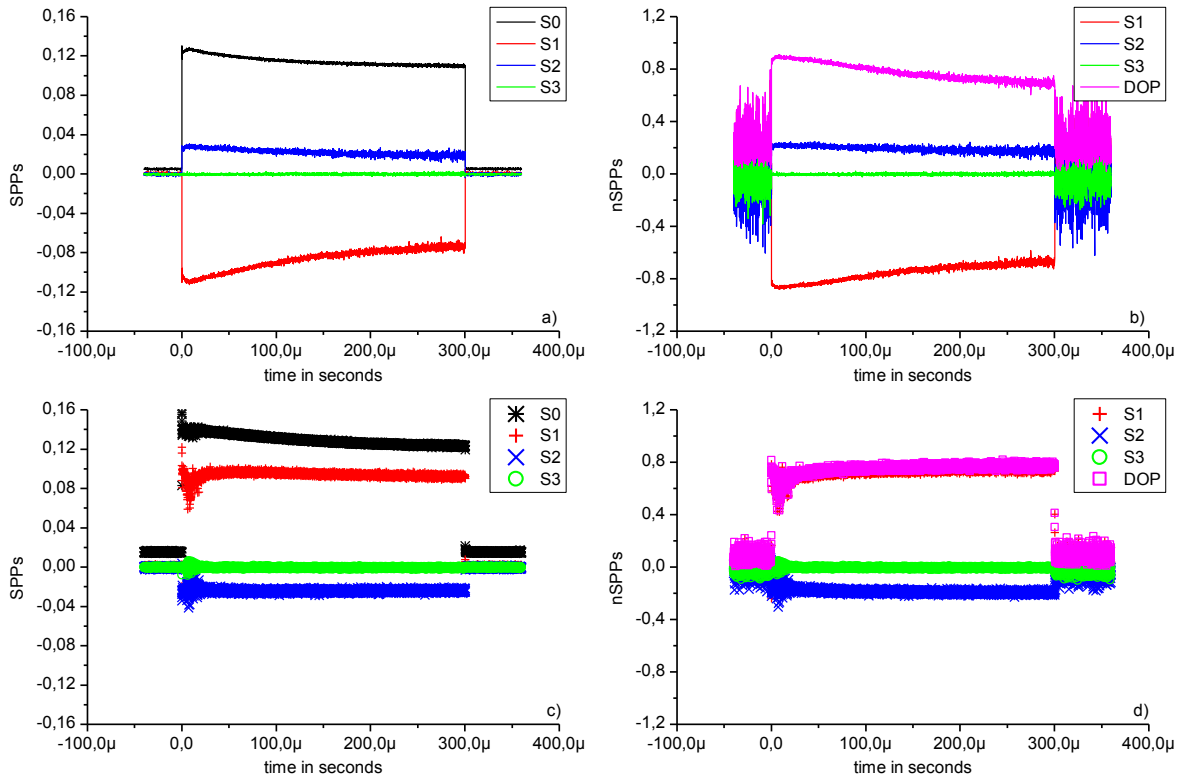

Figure 8.4 Stokes polarization parameters as a function of time of a 300μs pulse with a duty cycle of less than 1% and an applied voltage of 0.85V corresponding to a DC current of 0.66mA. (left) Color code as usual and visible in the legend for polarization mode 1 a) and 2 c). Right: Corresponding nSPP lines and symbols for polarization mode 1 b) and 2 d), respectively together with the DOP (magenta)

To identify the different states of polarization, the VCSEL has been operated under pulsed condition from now on. For the next investigations the pulse length T was set to be $300\mu s$ together with a pulse period P of 99ms, resulting in a duty cycle[20] D of less than 1%, which prevents excessive thermal heating, however, allowing comparable polarization fluctuations as in Figure 8.3. In contrast to the single shot measurements of Figure 8.3, time-traces for different rotation angles β of the quarter-wave plate have been measured and subsequently analyzed as follows: Due to the fact that the signals switch randomly between two values, these two extreme values have been recorded, via an envelope, averaged over 64 time traces, resulting in a repetitive measured time trace, containing the maxima and minima values now alternating from data point to data point. This exploited signal, recorded in the above mentioned manner is depicted in Figure 8.4a) and c) in terms of non-normalized SPPs as a function of time for the above described maxima and minima values, respectively. Two different resulting states of polarization 1 and 2 are distinguished by the well known symbols for the SPP $S_0(t)$ (black star), $S_1(t)$ (red plus), $S_2(t)$ (blue cross) and $S_3(t)$ (green circle) Figure 8.4a) as well as thin lines with corresponding color coding Figure 8.4c), respectively. These results clearly identify the orthogonality of the polarization states reflected by averaged values like $S_0=+0.11$, $S_1=-0.09$, $S_2=+0.025$ and $S_3=0$ for mode 1 and as $S_0=+0.125$,

---

[20] A duty cycle D is the percentage of one period P in which a signal T is active $D = \frac{T}{P} * 100\%$

$S_1=+0.1$, $S_2=-0.025$ and $S_3=0$ for mode 2, disclosing a change of sign within S_1 and S_2 whereas the values of S_3 remain the same at zero for both states. The corresponding nSPPs are depicted in Figure 8.4b) and d). They additionally show a large degree of polarization of roughly 0.8 for both polarization modes 1 and 2. These dynamic time-resolved nSPPs together with the DOP depicted in Figure 8.4b) and d) are in coincidence with high spectrally resolved SPPs under CW for small values around 0.66mA[21] depicted in Figure 7.4, complementing the experimental findings up to now.

In contrast to the random switching of the polarization of the VCSEL, occurring on timescales of many orders of magnitude and at low current values of 0.66mA, in the following time-resolved results of SPPs are presented for a fixed duty cycle D of 50%. The results on time-resolved SPPs are depicted on a linear timescale in Figure 8.5(top) obtained for $3\mu s$ pulse length and $6\mu s$ pulse period a), $30\mu s$ pulse length and $60\mu s$ pulse period b) and $120\mu s$ pulse length and $240\mu s$ pulse period c) and a pumping condition comparable to a pump current value of 11mA close to the thermal rollover.
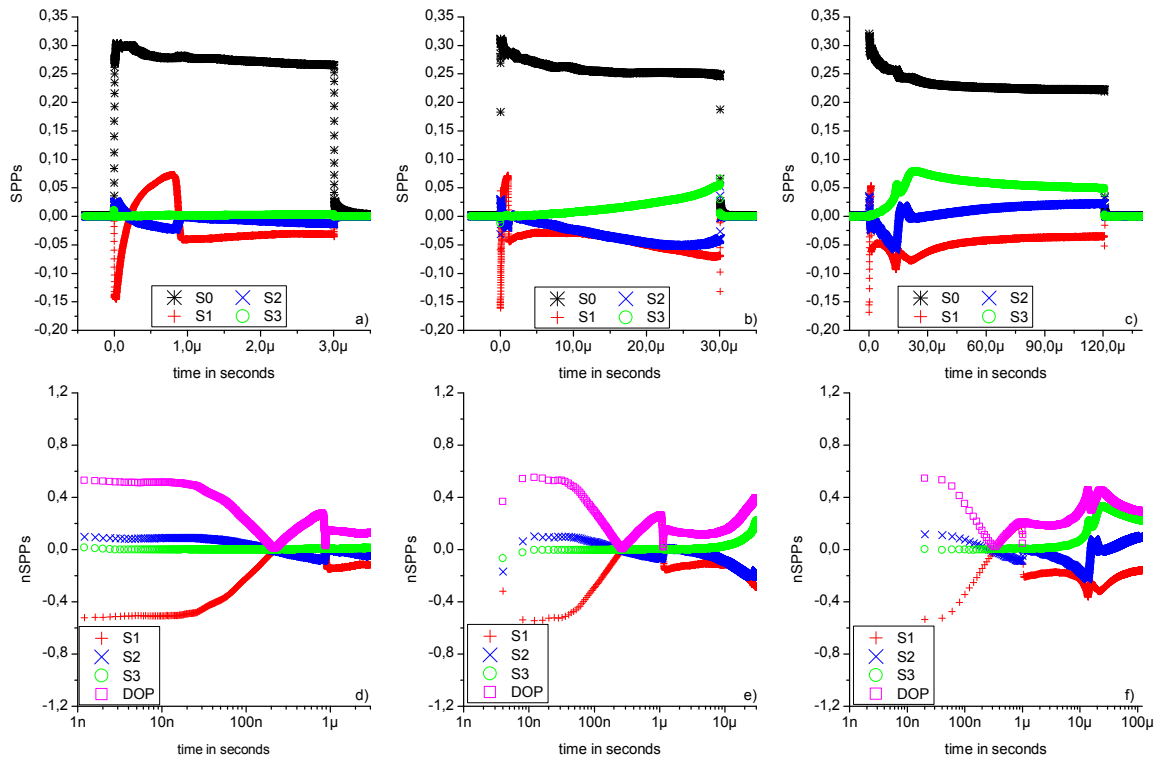
Figure 8.5 (top) Non-normalized Stokes polarization parameters S_0 (black star), S_1 (red plus), S_2 (blue cross) and S_3 (green circle) as a function of time of a VCSEL under pulsed condition with an applied voltage of 1.75V and different pulse duration times of $3\mu s$ a), $30\mu s$ b) and $120\mu s$ c). Bottom: nSPPs(t) S_1 (red plus), S_2 (blue cross) and S_3 (green circle) together with the DOP (magenta square) on a logarithmic timescale for the same applied voltage of 1.75V and the same pulse duration times of $3\mu s$ d), $30\mu s$ e) and $120\mu s$ f).

The non-normalized SPPs of the shortest pulse length of $3\mu s$ are depicted in Figure 8.5a) and show a polarization changing event between zero and slightly below $1\mu s$, reflected by a

---

[21] A pump current of 0.66mA is comparable with an applied bias voltage of 0.85V determined from the voltage-current curve not explicitly given here.

gradual change of sign of both SPPs $S_1(t)$ (red plus) and $S_2(t)$ (blue cross) from -0.15V to +0.07V and from +0.02V to -0.02V, respectively. Close to $1\mu s$ an abrupt change of the values of $S_1(t)$ and $S_2(t)$ is explicitly visible. $S_1(t)$ is changing its sign again by changing its value from +0.07V to -0.03V, whereas the value of $S_2(t)$ becomes zero. The further development of both time-resolved SPPs $S_1(t)$ and $S_2(t)$ is almost constant, however with a small reduction from 0V to -0.02V together with a small increase from -0.03V to -0.02V, respectively. The interesting behavior of $S_1(t)$ and $S_2(t)$ is accompanied by a constant negligible contribution of $S_3(t)$ of zero. Beside the SPPs $S_1(t)$, $S_2(t)$ and $S_3(t)$ the SPP $S_0(t)$ (black star) representing the total emitted power, has a value of 0.3V at the beginning of the pulse followed by a slight reduction down to a value of 0.26V, at the end of the pulse still with a trend towards smaller values. This leads to the assumption that we have not yet achieved a stationary state of polarization. Beside this almost linear reduction no further influences due to the dramatic polarization behavior, represented by the changes of sign of $S_1(t)$ and $S_2(t)$ are observable.

The results depicted in Figure 8.5b), represent the SPPs(t) for a pulse with a length of $30\mu s$, again with an applied voltage of 1.75V. Regarding the development of $S_0(t)$ (black star) in comparison with the former pulse length (10 times longer) a further decrease to a value of 0.25V is visible, together with a reduction of the negative slope at the end of the pulse, thus reflecting a transition into a constant state of polarization. In contrast to the result of the $3\mu s$ pulse, an increase of $S_3(t)$ up to a value of +0.05 is clearly observable at the end of the pulse, together with a reduction of both values of $S_1(t)$ and $S_2(t)$ being -0.07V and -0.06V, respectively. Due to the large timescale in this graph the polarization changing event at the beginning of the pulse is camouflaged, however, the change of sign of at least $S_1(t)$ can be supposed at the beginning of the pulse.

By increasing the pulse length even more by a factor of 4 resulting in a pulse length of $120\mu s$, leads to a constant contribution of $S_0(t)$ of 0.225V at the end of the pulse. This constant contribution of $S_0(t)$ above $50\mu s$ guarantees a stationary state of polarization, even demonstrated by the constant contributions of the nSPPs $S_1(t)$=-0.07V, $S_2(t)$=-0.02V and $S_3(t)$=+0.07V beyond a pulse duration time of $50\mu s$. The results of time-resolved SPPs investigated for three different pulse lengths of $3\mu s$, $30\mu s$ and $120\mu s$ with a constant voltage of 1.75V, showed a stationary polarization state of light emitted by the VCSEL beyond $50\mu s$ for a duty cycle of 50% and an applied voltage of 1.75V.

Below these results in Figure 8.5(bottom) their normalized counterparts are depicted on a logarithmic timescale, thus making these polarization dynamics comparable even for the three very different pulse lengths of $3\mu s$, $30\mu s$ and $120\mu s$. The nSPPs(t) together with the DOP(t) of the shortest pulse length of $3\mu s$ are depicted in Figure 8.5d). The complementary gradual change of sign of $S_1(t)$ and $S_2(t)$, followed by an abrupt change of sign of $S_1(t)$ together with a negligible contribution of $S_2(t)$ and $S_3(t)$ above $1\mu s$ of the pulse length, are clearly observable. Furthermore, the development of the DOP(t) (magenta squares) starting at a value of 0.55, shows a reduction down to a value of zero, representing a fully unpolarized state of light at $0.1\mu s$. This is followed by an increase of the DOP(t) up to a value of 0.3 at roughly $1\mu s$, followed by an abrupt reduction down to a value of 0.2, being constant up to the end of the pulse. A similar behavior is clearly visible in Figure 8.5e), presenting nSPPs(t) of a $30\mu s$ pulse on a logarithmic scale. The above discussed polarization dynamics of a $3\mu s$ pulse is completely

reflected at the beginning of the $30\mu s$ pulse. Furthermore, the behavior of polarization beyond a pulse length of $3\mu s$ is demonstrated, uncovering a slight increase of $S_3(t)$ as well as a reduction of both nSPPs $S_1(t)$ and $S_2(t)$. This change of the absolute values of $S_1(t)$, $S_2(t)$ and $S_3(t)$ results in an increase of the DOP(t) from a value of 0.2 at $3\mu s$ up to 0.4 at the end of the $30\mu s$ pulse. Finally, the nSPPs(t) on a logarithmic timescale of a pulse being as long as $120\mu s$, shows even more polarization dynamics. This dynamic is reflected by an abrupt change of sign of $S_2(t)$ from -0.2 to +0.1 together with a kink in the other nSPPs $S_1(t)$, $S_2(t)$ and the DOP(t) as well. However, after this point of discontinuity roughly around $1\mu s$, $S_1(t)$, $S_2(t)$ and $S_3(t)$ asymptotically reach their values of -0.1, +0.1 and +0.2, respectively. This results in a value of the DOP(t) of 0.25, representing an almost unpolarized state of light. These results demonstrate that the polarization dynamics of shorter pulses are clearly observable within longer pulses, when comparing these results on a logarithmic timescale. Furthermore, we have seen from these results that the dynamic is fully uncovered, which means that the state of polarization remains constant at the end of the $120\mu s$ pulse, together with a constant value of the total emitted intensity represented by the non-normalized SPP $S_0(t)$ (black star) in Figure 8.5c). These findings justify the use of pulses with a duration time of $120\mu s$ for the investigations of the behavior of the state of polarization for different applied voltages.
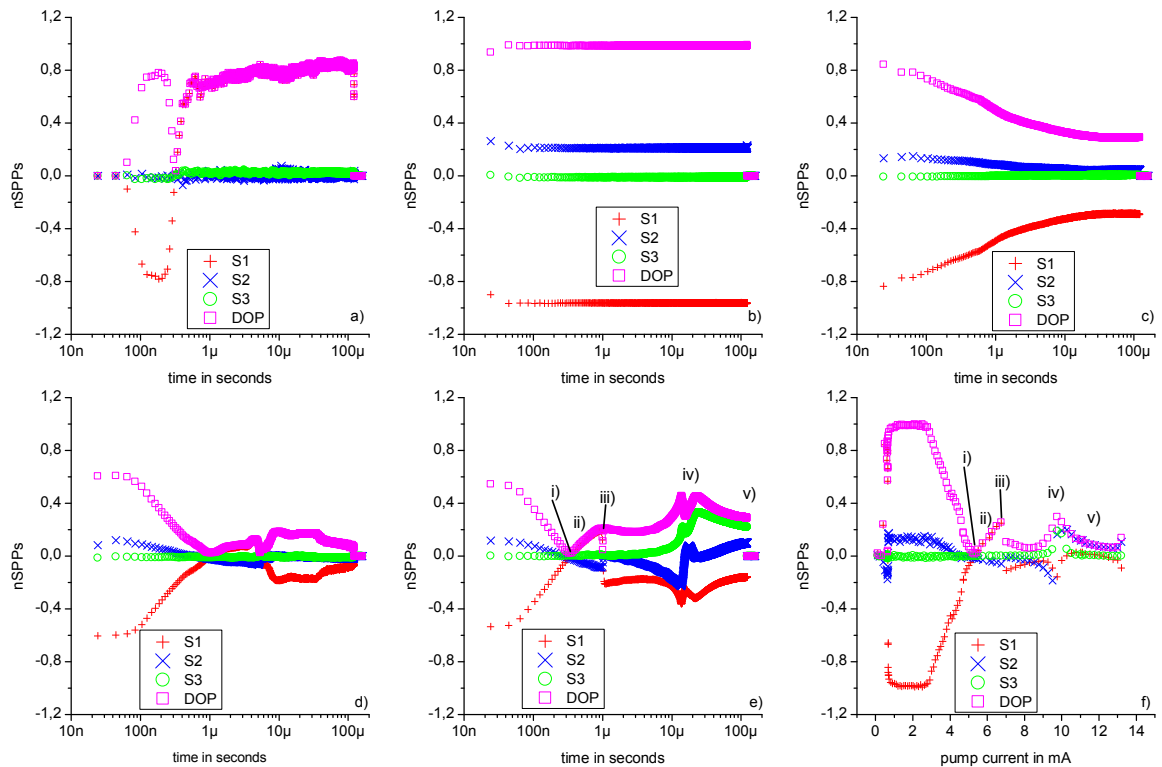
Figure 8.6 Normalized Stokes polarization parameters S_1 (red plus), S_2 (blue cross) and S_3 (green circle) together with the DOP (magenta square) all as a function of time on a logarithmic scale for a constant pulse duration time of 120µs, however, with different values of the applied voltage of 0.85V a), 1.00V b), 1.35 c), 1.55V d) and 1.75V e). These results in comparison with the nSPP and the DOP as a function of pump current on a linear scale f), clearly demonstrate the similar polarization behavior of a transverse multi-mode VCSEL under pulsed operation in comparison with continuous wave operation mode. The especially marked positions i)-v) in e) and in f) are explicitly explained in the text.

In Figure 8.6a)-e) nSPPs together with the DOP all as a function of time of $120\mu s$ pulses are depicted for applied voltages of 0.85V, 1.00V, 1.35V, 1.55V and 1.75V on a logarithmic

timescale. Additionally and for comparison, the nSPPs as a function of pump current together with the DOP(I_{pump}) (cf. Figure 8.2) are depicted in Figure 8.6f).

The time-resolved results depicted in Figure 8.6a)-e) have been obtained by averaging the time-resolved signals over 64 traces for each rotation angle β of the quarter-wave plate, thus resulting in smoothed sets of data. The trigger of the leading edge of the signals is roughly at a time of 10^{-8}seconds, reflected by a change of values of the nSPP $S_1(t)$ (red plus) and the DOP (magenta square) from zero to non-zero values. This is due to the fact that no light is emitted from the VCSEL, before the leading edge of the pulse. However, immediately after applying the voltage to the VCSEL, light is detected due to its fast turn-on dynamics on sub-nanoseconds [19], being larger, than our timing resolution on a nanosecond timescale. The dynamic of polarization is clearly visible on a microsecond timescale. First, the state of polarization is almost fully polarized with a value of the DOP(t) of almost 0.8 and linearly polarized with a vertical orientation reflected by a dominant value of $S_1(t)$ of -0.8 in the first 200ns roughly. After that, a transition to the orthogonally linearly polarized state of polarization is observed, reflected in a change of the value of $S_1(t)$ from -0.8 to +0.8 together with a reduction of the DOP to zero (here $S_1(t)$ is zero as well) followed by an increase up to a value of 0.8, reflecting an almost fully polarized state of light again. This state of polarization remains until the end of the pulse, then the values of $S_1(t)$ and the DOP(t) drop down to zero, representing the turn-off region together with the zero contributions of $S_2(t)$ and $S_3(t)$. This stable state of polarization at the almost end of the pulse is also visible in Figure 8.6f) at a pump current of 0.6mA below the previously in detail explained polarization switch.

By increasing the applied voltage from 0.85V in Figure 8.6a) to 1.00V in Figure 8.6b) a very constant state of polarization is clearly observable, reflecting above 10^{-8}seconds the beginning of the optical signal of the VCSEL. The constant fully linearly polarized state of light is represented by $S_1(t)=-1$, $S_2(t)=+0.2$ and $S_3(t)=0$, thus resulting in a value of the DOP(t)=1. This state of polarization can be identified in Figure 8.6f) in a pump current range between 1mA and 3mA.

A reduction of the values of the DOP(t) is visible in Figure 8.6c) when applying a voltage of 1.35V; hence the state of polarization changes as a function of the duration time t of the pulse as follows: at the beginning of the pulse the values of $S_1(t)$ and $S_2(t)$ are comparable with the constant state of polarization in Figure 8.6b) being -0.8 and +0.15, respectively, together with a resulting value of the DOP(t) above 0.8. These values $S_1(t)$, $S_2(t)$ and DOP(t) gradually change to -0.3, almost zero and 0.3, respectively. This reduction of the value of the DOP(t) has been explained in particular with the transverse multi-mode emission in combination with an incoherent superposition of their complementary states of polarization. However, this reduction of the DOP(t) down to a value of zero under pulsed condition for an applied voltage of 1.55V, as depicted in Figure 8.6d), is now clearly observable on a timescale of microseconds at a time of 10^{-6}seconds. In addition with a complex behavior of the DOP(t), mainly caused by a change of sign of $S_1(t)$ together with negligible contributions of $S_2(t)$ and $S_3(t)$.

In Figure 8.6e) time-resolved nSPPs are depicted together with the DOP(t) of the VCSEL for the highest applied voltage of 1.75V, comparable to a CW pump current of 13mA, thus being above the thermally induced rollover. These results are well known from Figure 8.6f) (cf. Figure 7.1) with its in particular explained polarization behavior earlier in this thesis and have been depicted here to uncover the following interesting coincidences and similarities:

i) a reduction of the DOP down to a value of zero

ii) an increase of the DOP mainly caused by an increase of the value of S_1

iii) an abrupt change of sign of S_1 together with a reduction of the DOP to zero

iv) an increase of the circular component S_3, together with a change of sign of S_2, thus resulting in an increase of the DOP at the almost end of the pulse and at a pump current value of 10mA (rollover)

v) at the end of the pulse the values of $S_1(t)$, $S_2(t)$ and $S_3(t)$ together with the DOP(t) trend towards zero in Figure 8.6e), also observable in Figure 8.6f) at pump current values above 10mA

In conclusion, the complex polarization behavior of a transverse multi-mode VCSEL with different threshold values for each transverse modes in combination with their individual relative contributions to the total emitted optical output power (cf. Figure 7.6a)) is also visible in the time-resolved normalized Stokes polarization parameter results.

The analogy between the nSPPs(t) on a logarithmic timescale (Figure 8.6e)) and the nSPPs(I_{pump}) (Figure 8.6f)) are presented for the first time, uncovering an interesting relation between time-resolved and pump current resolved SPPs, hence the polarization behavior. These experimental findings uncover that thermal heating inside the VCSEL mainly causes the complex polarization behavior. Whereas the pump current is gradually increased for the nSPPs(I_{pump}) the applied voltage hence the induced pump current have a constant value right after a few nanoseconds, resulting in a change of temperature inside the VCSEL only.

The combination of these two results namely high spectrally resolved Stokes polarization parameters (SPPs($\tilde{\lambda}$)) and time-resolved Stokes polarization parameters (SPPs(t)), result in spectro-temporally resolved Stokes polarization parameters (SPPs($\tilde{\lambda}$,t)), which will be presented in the next chapter.

Time-resolved Stokes polarization parameters SPPs(t)

9. Spectro-temporally resolved Stokes polarization parameters SPPs($1/\lambda$,t)

In this chapter experimentally obtained results of spectro-temporally resolved Stokes polarization parameters (SPPs($\frac{1}{\lambda} = \tilde{\lambda}$,t)) are presented and discussed. These experimental results combine and confirm the experimentally obtained results of high spectrally as well as time-resolved SPPs presented in chapter 7 and 8, respectively, resulting in new insights into polarization behavior of each particular transverse mode of transverse multi-mode VCSELs. Furthermore, the spectro-temporally resolved results uncover a drift in wave number as it has already been investigated for transverse single-mode VCSELs [76], however, here for the first time for each particular transverse mode. These findings can immediately be utilized to motivate theoretical modeling, thus providing a better understanding of transverse mode dynamics to improve the VCSELs performance technologically in a future step.

This chapter is organized as follows: first, a measurement technique, called step-scan time-resolved FTIR spectroscopy available with the utilized FTIR-spectrometer (Bruker Vertex 80V) is directly explained on the basis of spectro-temporally resolved measurements. They demonstrate the functionality of this experimental method as well as the potential to provide fundamental information on the dynamical behavior of each particular transverse mode. Experimental measurements for pulse duration times of $120\mu s$, chosen equally long as in the previous chapter and comparable with the former obtained results will be shown in the second part. After that, experimental results of spectro-temporally resolved SPPs for a short pulse with a duration time of $3\mu s$ and the maximum achievable time resolution of 5ns as well as pulses with $120\mu s$ duration time and a time resolution of 100ns, are presented using a spectral resolution of 0.1cm^{-1} for both pulse length. The latter result allows a comparison with continuous wave operation results which have been already discussed at the end of chapter 8, regarding time-resolved SPPs. At the end of this chapter, further experimental findings are shown as a function of both wave number and time simultaneously, resolved for each particular transverse mode. A comparison of these results for different applied voltages reveals an idea on which timescale thermal effects, manipulate the transverse mode dynamic.

The experimental setup is not depicted in this chapter, due to the fact, that it looks the same as in chapter 7, where high spectrally resolved SPPs have been obtained utilizing also a FTIR-spectrometer (Bruker Vertex 80V). With this apparatus it is possible to perform spectro-temporally resolved measurements, utilizing the step-scan mode. This concept is explained in the following on the basis of an exemplary measurement of a $1\mu s$ pulse, therefore utilizing no polarization selective optics such as quarter-wave plate or linear polarizer.

The step-scan time-resolved FTIR spectroscopy measurement technique is only applicable for repetitive processes. However, as we already know from literature [19] as well as from results presented in this thesis, the pulsed behavior of the VCSEL is repetitive, enabling investigations on spectro-temporally resolved SPPs of transverse multi-mode VCSELs via this method. The fundamental principle of the step-scan technique is to record the full optical signal of the pulsed VCSEL, as a function of time for each point of an interferogram. This stepwise scanning of interferograms, as a function of time t is exemplarily depicted in Figure 9.1a). Here, five interferograms are illustrated, together with two traces (left and right) with slightly varying intensity values very close to zero, reflecting the time region without bias applied to the VCSEL. As a guide to the eye this applied bias voltage is illustrated by the grey rectangular pulse in Figure 9.1a). The fringes due to destructive and constructive interferences as a function of the mirror position x are clearly visible from the five central interferograms. The

stepwise scanning technique, to obtain such a set of data, works as follows: For each mirror position x the intensities are recorded as a function of time, averaged over many pulses. After that, the mirror is moved one step further, in order to subsequently record interferogram points as a function of time, always beginning with at the same temporal position of the electrical pulse. Performing these measurements many times over, resulting in a set of interferograms (see Figure 9.1a)), allowing a reconstruction of optical spectra at the corresponding time via a Fouriertransformation. These resulting optical spectra as a function of time are depicted in Figure 9.1b). This image representation with the wave number $\tilde{\lambda}$ in cm^{-1} on the vertical axis and the time t in microseconds on the horizontal axis, shows an optical pulse of the VCSEL with a duration time of 1μs for an applied voltage of 0.88V. The selected optical resolution of 0.1cm^{-1} is on one hand sufficient to clearly separate the polarization modes of the fundamental transverse mode and uncovers a slight spectral redshift of both polarization modes of about 0.5cm^{-1}. On the other hand the time resolution of 5ns uncovers a switch between the two polarization modes from one mode to the other and back, clearly observable right at the beginning of the pulse. This first result measured without polarization selective optics, such as quarter-wave plate or linear polarizer, clearly demonstrates the potential of the step-scan method, to provide deeper knowledge of the dynamics of each particular transverse mode as a function of time and wave number simultaneously.

a)   b)
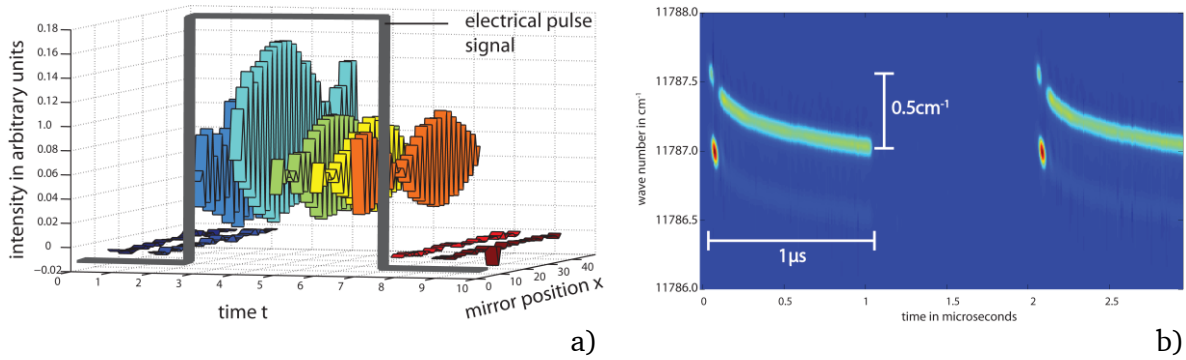
Figure 9.1 a) Exemplarily depicted set of data points both as a function of time t and mirror position x to explain the step-scan method. 1μs long pulse spectro-temporally resolved b).

In the following, experimental results of spectro-temporally resolved SPPs are presented for two different pulse length of 3μs and 120μs, both with a duty cycle of 50% and for an applied voltage of 1.75V, being comparable with a pump current roughly at the thermal rollover. The spectral resolution was adjusted to a value of 0.1cm^{-1} for both measurements, however with different time resolutions, being the maxima adjustable value of 5ns for the 3μs pulse and 100ns for the 120μs pulse. From the results of chapter 8 we know already, that the polarization dynamics should be even the same for the complete 3μs pulse and the first 3μs of the 120μs pulse. Therefore, the nSPPs($\tilde{\lambda}$,t) are pictured in Figure 9.2 and Figure 9.3 for two different pulse length of 3μs and 120μs, respectively. Whereas the results of $S_0(\tilde{\lambda},t)$ for both pulse length are presented as a function of wave number and time, the results of $S_1(\tilde{\lambda},t)$, $S_2(\tilde{\lambda},t)$, $S_3(\tilde{\lambda},t)$ and the DOP($\tilde{\lambda}$,t) are depicted in a simplified manner, namely as a function of time only, however still uncovering the full polarization dynamic of each particular transverse mode.

In Figure 9.2(top) color coded $S_0(\tilde{\lambda},t)$ representing the total intensities of the first four transverse modes TM_1, TM_1, TM_3 and TM_4 are shown, starting with the fundamental one at the lowest wave number, followed by the higher order transverse modes with even higher wave numbers, as a function of the wave number in cm^{-1} and time in microseconds, clearly illustrating, a pulse width of 3μs. Furthermore, an exponential behavior of the wave number

as a function of time is observable and is discussed later in more detail. An abrupt decrease followed by an increase of intensity of the third transverse mode TM$_3$ is clearly visible at $1\mu s$, together with a stepwise change in wave number, that has been observed already regarding the high spectrally resolved optical spectra under continuous wave condition (cf. Figure 7.7a)).
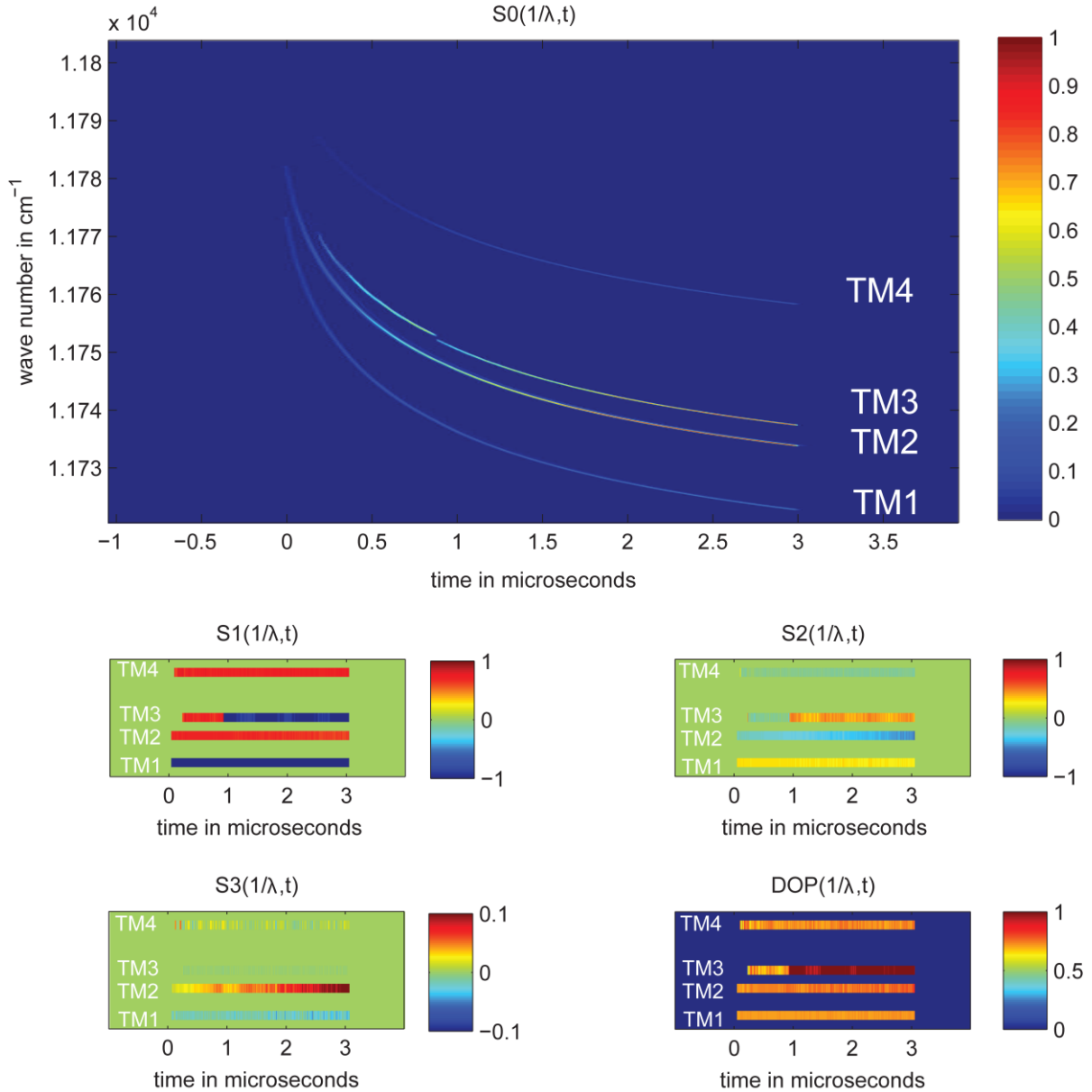

Figure 9.2 Spectro-temporally resolved normalized Stokes polarization parameter of a 3µs long pulse. (top) $S_0(\tilde{\lambda},t)$ as a function of both wave number (vertical axis) and time (horizontal axis). Bottom: $S_1(\tilde{\lambda},t)$, $S_2(\tilde{\lambda},t)$, $S_3(\tilde{\lambda},t)$ and DOP($\tilde{\lambda}$,t) in a simplified representation, therefore only as a function of time, however for each particular transverse mode.

Figure 9.2(bottom) shows a simplified representation of the nSPPs $S_1(\tilde{\lambda},t)$, $S_2(\tilde{\lambda},t)$, $S_3(\tilde{\lambda},t)$ and the DOP($\tilde{\lambda}$,t) of the 3µs pulse. This simplification means, that the redshift in wave number has been neglected, on the one hand due to the fact, that this redshift looks always the same for each nSPPs($\tilde{\lambda}$,t) and on the other hand for the sake of clarity. However, a change of sign is demonstrated regarding $S_1(\tilde{\lambda},t)$ changing its sign from positive to negative, below and above $1\mu s$ of the duration time of the pulse, respectively. Furthermore, the constant contribution of the first, second and fourth transverse mode each with different signs (TM$_1$ negative, TM$_2$

positive and TM_4 positive) can be observed. This behavior is also observable in Figure 9.2(S2) representing $S_2(\tilde{\lambda},t)$, however with complementary signs, thus being a change of sign of the third transverse mode TM_3 from negative to positive and constant negative contributions of TM_1 and TM_2 as well as positive values of the fundamental transverse mode TM_1.

In contrast to these experimental findings, such that the main contributions of $S_1(\tilde{\lambda},t)$ and $S_2(\tilde{\lambda},t)$ are visible right at the beginning of the pulse, the contribution of $S_3(\tilde{\lambda},t)$ reflecting the circularly polarized component depicted in Figure 9.2(S3), starts almost at the middle of the $3\mu s$ pulse with a small positive amount according to TM_2, together with complementary sign contributions with respect of TM_1 and TM_3. However, all these values in the range between - 0.1 and +0.1 are very small in comparison with their corresponding values of $S_1(\tilde{\lambda},t)$ and $S_2(\tilde{\lambda},t)$ both being in the range between -1 and +1.

The spectro-temporally resolved degree of polarization $DOP(\tilde{\lambda},t)$ of the four contributing transverse modes for the $3\mu s$ long pulse is depicted in Figure 9.2(DOP). This result uncovers, that besides their different intensities (clearly visible in the first row of Figure 9.2(S0)), they exhibit a very high DOP above a value of 0.7, reflecting an almost fully polarized state of light for all observed transverse modes almost over the full respective pulse duration times of $3\mu s$. Furthermore, an abrupt change of the wave number of the third transverse mode TM_3 is also clearly observable in the DOP (cf. Figure 9.2(DOP)), reflected by an abrupt increase from 0.7 to 1. After the detailed explanation and discussion of the spectro-temporally resolved nSPPs of the short pulse, in the following the experimentally obtained results of the longer pulse will be shown.

The $nSPPs(\tilde{\lambda},t)$ of the $120\mu s$ long pulse are depicted in Figure 9.3 (in the same manner regarding the simplified representation) disclosing an exponential behavior of the wave number with respect to the duration time as it has been observed for the $3\mu s$ pulse (cf. Figure 9.2(S0)). However with a quite constant wave number at the almost end of the pulse at least above $60\mu s$. The abrupt change of intensity and wave number of TM_3 is not visible here, due to the reduced temporal resolution and the linear time scale. The exponential behavior of each particular transverse mode will be discussed later, providing a closer insight into the thermal development of VCSELs.

The complementary contributions of each particular transverse mode regarding the sign of their $S_1(\tilde{\lambda},t)$ and $S_2(\tilde{\lambda},t)$ results are observable in Figure 9.3(S1) and Figure 9.3(S2), respectively. Furthermore, their dominant contribution to the total polarization state is reflected by the fact, that $S_1(\tilde{\lambda},t)$ and $S_2(\tilde{\lambda},t)$ are in the range between -1 and +1. The $S_3(\tilde{\lambda},t)$ of TM_2 depicted in Figure 9.3(S3) shows the dynamic of the circular component of this particular transverse mode. The DOP resulting from these values is depicted in Figure 9.3(DOP) and uncovers a high degree of polarization for all transverse modes on a large time scale of $120\mu s$ as well.

These results of the $nSPPs(\tilde{\lambda},t)$ of both the $3\mu s$ and the $120\mu s$ long pulse uncover the complex polarization behavior of each particular transverse mode as well as the polarization modes of TM_3. Whereas the contributions of $S_1(\tilde{\lambda},t)$ and $S_2(\tilde{\lambda},t)$ are almost constant as a function of time, the dynamic of $S_3(\tilde{\lambda},t)$ is clearly observable in both Figure 9.2(S3) and Figure 9.3(S3). Furthermore, the almost constant and large value of the $DOP(\tilde{\lambda},t)$ of each transverse mode has been uncovered as well and is in coincidence with the results obtained under CW operation.
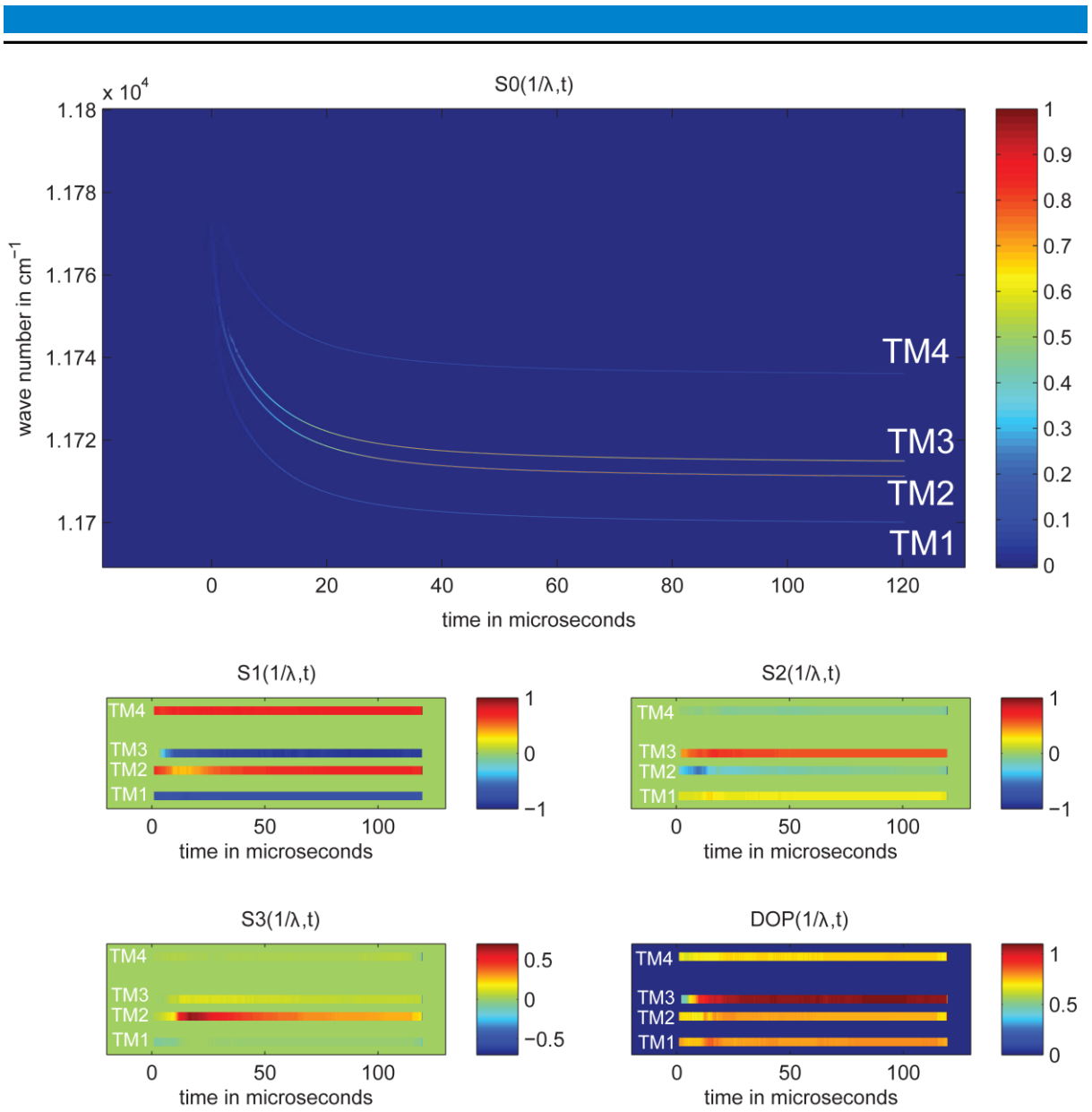
Figure 9.3 Spectro-temporally resolved normalized Stokes polarization parameter of a 120μs long pulse. (top) $S_0(\tilde{\lambda},t)$ as a function of both wave number (vertical axis) and time (horizontal axis). Bottom: $S_1(\tilde{\lambda},t)$, $S_2(\tilde{\lambda},t)$, $S_3(\tilde{\lambda},t)$ and DOP$(\tilde{\lambda},t)$ in a simplified representation, therefore only as a function of time, however for each particular transverse mode.

Additionally to these results in Figure 9.4, the sum over the recorded wave number as a function of time was executed for each of the non-normalized SPP $S_0(\tilde{\lambda},t)$, $S_1(\tilde{\lambda},t)$, $S_2(\tilde{\lambda},t)$ and $S_3(\tilde{\lambda},t)$. The sum of the SPPs can only be reasonable generated utilizing non-normalized SPPs. The results of the sum over all measured wave numbers as a function of time of S_0 (black line), S_1 (red line), S_2 (blue line) and S_3 (green line) are depicted in Figure 9.4 for both the 3μs a) as well as for the 120μs pulse b). These results are compared in the following with our previous time-resolved SPP measurements, depicted in Figure 9.4c) and d) for a 3μs and a 120μs long pulse, respectively.
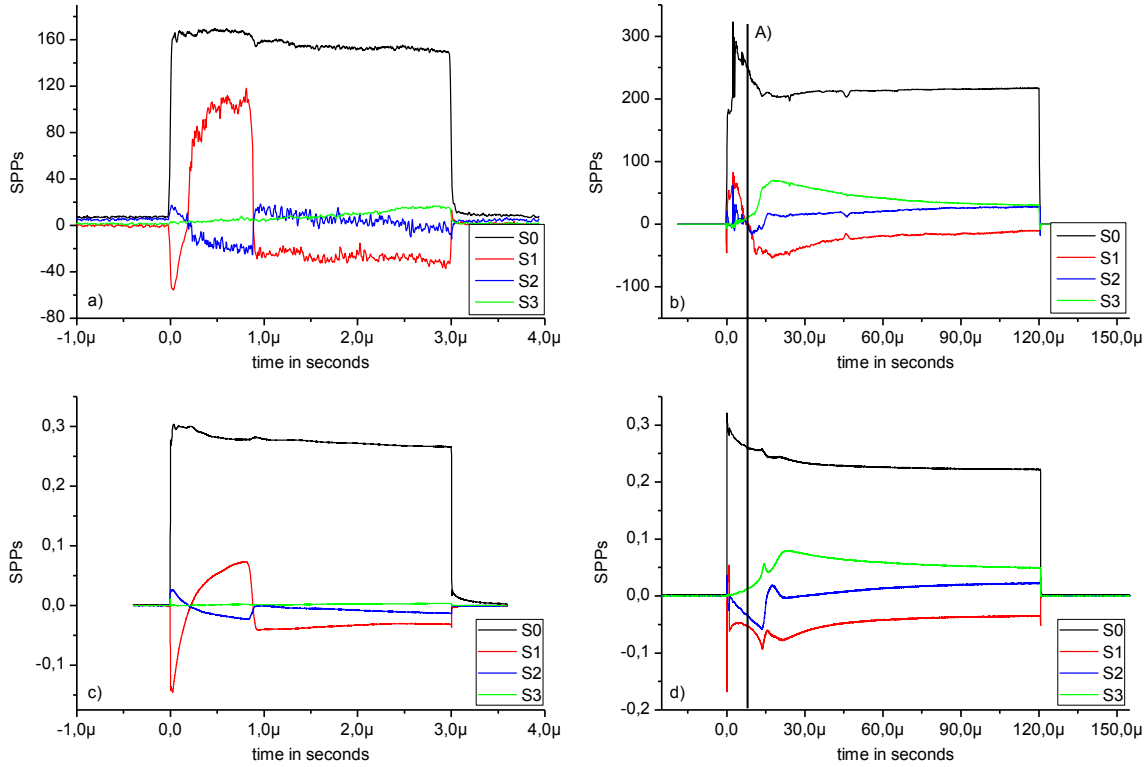
Figure 9.4 (top) Sum of the SPP over the wave number for the 3μs long pulse (left) and the 120μs long pulse (right). Bottom: Time-resolved SPP of the 3μs long pulse (left) and the 120μs long pulse (right) in direct comparison.

In Figure 9.4a) the total intensity of the pulse is represented by $S_0(t)$ (black line) reflecting a fast slope at the beginning of the pulse at a time of $0\mu s$ as well as at the end of the pulse at $3\mu s$, together with a higher value at the beginning of the pulse and a slight reduction as a function of time right up to the end of the pulse. The contribution of the circular polarization component, represented by $S_3(t)$ (green line) shows values very close to zero, however with a slight increase even still negligible and barely visible at the end of the pulse. In contrast to these almost constant contributions of $S_0(t)$ and $S_3(t)$, the behavior of $S_1(t)$ (red line) and $S_2(t)$ (blue line) uncovers dramatic changes in polarization, reflected by complementary changes of sign, observable twice during the duration time of the pulse. A dominant negative contribution of $S_1(t)$ together with an almost negligible positive contribution of $S_2(t)$ can be observed, followed by a gradual change of sign of both $S_1(t)$ and $S_2(t)$, thus resulting in positive and negative contributions of $S_1(t)$ and $S_2(t)$, respectively. The abrupt change of wave number of the third transverse mode TM$_3$ illustrated in Figure 9.2(S0) together with a change of sign of both $S_1(\tilde{\lambda},t)$ and $S_2(\tilde{\lambda},t)$ visible in Figure 9.2(S1) and Figure 9.2(S2) is the physical explanation of the abrupt polarization switching phenomenon reflected by a change of sign of $S_1(t)$ (red line) and $S_2(t)$ (blue line) in Figure 9.4a). These experimental findings together with the constant negative contributions of $S_1(t)$ and the almost negligible contribution of $S_2(t)$ however with a change of sign coincides very well with the experimental results utilizing a fast photo detector only (cf. chapter 8) and are depicted in Figure 9.4c).

To complete the analysis of these results, the preformed sum over wave numbers as a function of time of the $120\mu s$ pulse depicted in Figure 9.4b) is discussed and compared with its counterpart results depicted in Figure 9.4d). The changes of sign of $S_1(t)$ and $S_2(t)$ at the beginning of the pulse are clearly visible, however, due to the minor time resolution of 100ns one cannot resolve the results almost at the beginning of the pulse. However, the slight increase of $S_3(t)$ as well as the negative contribution of both $S_1(t)$ and $S_2(t)$ are clearly observable at a pulse duration time of $7\mu s$ denoted with an A). From this point proceeding in

time the state of polarization coincides very well with the results (cf. Figure 9.4b) and d)), such that a remarkable increase of the circular component reflected by the positive contribution of $S_3(t)$ is clearly observable. Furthermore, a gradual increase of both SPPs $S_1(t)$ and $S_2(t)$ is visible in both Figure 9.4b) and d), resulting in a change of sign of $S_2(t)$, such that the final state of polarization is reflected by $S_2(t)$ and $S_3(t)$ with respective positive values, in combination with a negative contribution of $S_1(t)$. For the sake of completeness the total intensity of the light emitted by the pulsed VCSEL, represented by $S_0(t)$ (black line), is reflecting a reduction from an intensity at the beginning of the pulse to a value that remains constant, thus being in good coincidence of $S_0(t)$ depicted below. This is in agreement with the step-scan results depicted in Figure 9.3(S0), showing a constant wave number beyond at least the half of the pulse duration time of about $60\mu s$. These constant contributions of the experimentally obtained spectro-temporally resolved SPPs at the almost end of the long pulse, are comparable with the results obtained utilizing the VCSEL in the continuous wave operation mode and are presented in the following.
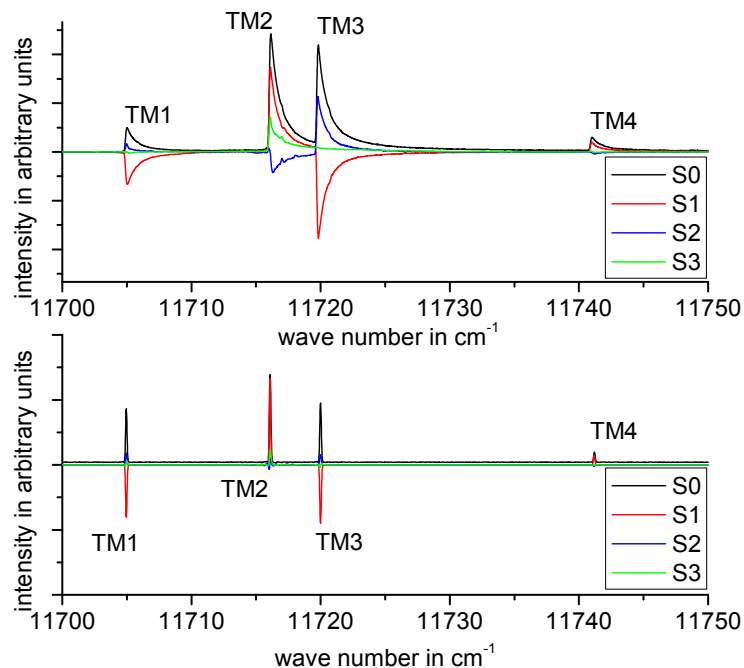
Figure 9.5 Step-scan results of Stokes polarization parameter S_0 (black line), S_1 (red line), S_2 (blue line) and S_3 (green line) summed over the pulse duration time and depicted as a function of wave number (top) in comparison with high spectrally resolved SPPs (same notation) of a VCSEL under CW operation (bottom)

Again, one has to perform a summation of the step-scan results, however now with respect to time, resulting in spectrally resolved SPPs which are depicted in Figure 9.5(top), together with the corresponding results of chapter 7 (bottom). This comparison regarding the qualitative behavior of the state of polarization only, should give an idea that also the spectrally resolved SPPs measured under continuous wave operation condition with a pump current of 10mA at the thermal rollover, coincide with the spectro-temporally resolved results, now integrated over the total duration time of the pulse of $120\mu s$. The time-integration and the spectral redshift of the transverse modes are the reasons for the asymmetric shape of the peaks observable in Figure 9.5(top) for $S_0(\tilde{\lambda})$, $S_1(\tilde{\lambda})$, $S_2(\tilde{\lambda})$ and $S_3(\tilde{\lambda})$. The complementary contributions of the SPPs of different transverse modes TM_1, $TM_{2,}$ TM_3 and TM_4 with respect to their signs are clearly visible in this illustration. Furthermore, the ratio of the intensities of the four transverse modes are observable, reflecting the dominant contribution of the second order transverse mode TM_2 at roughly $11715cm^{-1}$, followed by the third higher order transverse mode TM_3 around $11720cm^{-1}$ as well as a non-negligible contribution of the fundamental transverse mode TM_1 at the lowest wave number about $11705cm^{-1}$ and finally

with a very weak intensity of the fourth transverse mode TM_4 slightly above $11740 cm^{-1}$. This comparison in combination with the discussion above regarding the time-resolved results, both obtained from the spectro-temporally resolved results, via the corresponding summation over wave number (see Figure 9.4) and time (see Figure 9.5), respectively, demonstrates another cross-link among the achieved experimental results presented in this work.

Furthermore, from $S_0(\tilde{\lambda},t)$ representing the total intensity of each particular transverse mode as a function of wave number and time simultaneously (Figure 9.2 and Figure 9.3) one can extract a characteristic thermal time constant τ_{th}, reflecting the thermal behavior inside the VCSEL. This thermal constant is estimated for different biased voltages in combination with a $120\mu s$ pulse at a duty cycle of 50%, in the following.

It has been shown already in [76] that for a square pulse voltage, the active region temperature T_{act} exponentially approaches a steady-state temperature as

$$T_{act}(t) = T_{sub} + \Delta T(P_{dis}) \left(1 - \exp\left(-\frac{t - t_0}{\tau_{th}} \right) \right) \tag{9.1}$$

where T_{act} is the temperature of the active region of the VCSEL, T_{sub} is the temperature of the substrate, P_{dis} the dissipated power due to joule heating with respect to the voltage modulation, ΔT is the temperature increase corresponding to the power dissipated by the pulse, t_0 is the pulse switch-on time and τ_{th} is known as the thermal time constant. By taking advantage of the fact, that the emission wave number depends linearly on the temperature of the active layer [67], one can estimate the characteristic thermal time constant τ_{th} of the VCSEL via the following formula, thus illustrating that the emission wave number $\tilde{\lambda}(t)$ changes in time as an exponential decay as

$$\tilde{\lambda}(t) = \tilde{\lambda}_f - \Delta\tilde{\lambda} \exp\left(-\frac{t - t_0}{\tau_{th}} \right). \tag{9.2}$$

Where $\Delta\tilde{\lambda}$ is the redshift of the emission wave number due to the active layer temperature raise and $\tilde{\lambda}_f$ is the steady-state emission wave number and t_0 is the starting time of the pulse and can be equal to zero.
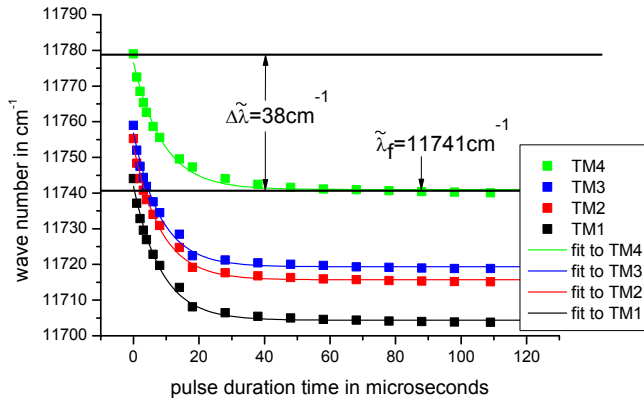
Figure 9.6 Peak values of each particular transverse mode TM$_1$ (black squares), TM$_2$ (red squares), TM$_3$ (blue squares) and TM$_4$ (green squares) as a function of both time and wave number together with their corresponding fits (line) with the same color code

Table 9.1 Extracted fit parameters color coded for each particular transverse mode TM$_1$, TM$_2$, TM$_3$ and TM$_4$

		$\tilde{\lambda}(t) = \tilde{\lambda}_f - \Delta\tilde{\lambda}\exp(-\frac{t-t_0}{\tau_{th}})$	
		Value	Standard Error
TM$_4$	$\tilde{\lambda}_f$	11740.99cm^{-1}	0.36cm^{-1}
	$\Delta\tilde{\lambda}$	37.54cm^{-1}	0.78cm^{-1}
	τ_{th}	8.99μs	0.51μs
TM$_3$	$\tilde{\lambda}_f$	11719.35cm^{-1}	0.34cm^{-1}
	$\Delta\tilde{\lambda}$	37.48cm^{-1}	0.76cm^{-1}
	τ_{th}	8.30μs	0.42μs
TM$_2$	$\tilde{\lambda}_f$	11715.69cm^{-1}	0.32cm^{-1}
	$\Delta\tilde{\lambda}$	37.43cm^{-1}	0.71cm^{-1}
	τ_{th}	8.39μs	0.41μs
TM$_1$	$\tilde{\lambda}_f$	11704.36cm^{-1}	0.32cm^{-1}
	$\Delta\tilde{\lambda}$	37.50cm^{-1}	0.71cm^{-1}
	τ_{th}	8.47μs	0.41μs

In Figure 9.6 the wave number of the maximal peak values of each particular transverse mode, namely the fundamental TM$_1$ (green squares), second TM$_2$ (blue squares), third TM$_3$ (red squares) and fourth TM$_4$ (black squares) higher order transverse mode are depicted as a function of time, together with exponential decay fits, following equation (9.2) represented by corresponding color coded lines. The fit parameters $\Delta\tilde{\lambda}$ and $\tilde{\lambda}_f$ are schematically depicted in Figure 9.6 for the sake of explanation. Furthermore, the number values of these fit parameters, together with the characteristic thermal time constant τ_{th} are explicitly given in Table 9.1 for each particular transverse mode. The fit parameter $\Delta\tilde{\lambda}$ depicted for the fourth transverse mode TM$_4$ (green squares) reflects the redshift of the transverse mode from 11779cm^{-1} at the beginning of the pulse at t=0s to a wave number of roughly 11741cm^{-1}, thus being the steady-state wave number $\tilde{\lambda}_f$ almost already reached at the middle of the pulse duration time at t=60μs. The resulting characteristic thermal time constant τ_{th} is about 8.9μs. This thermal time constant values τ_{th} as well as the redshift parameter $\Delta\tilde{\lambda}$ coincides with that of the other transverse modes within the given standard deviation. These high values of τ_{th} in the range between 8.3μs and 8.9μs in comparison with values reported in [76] of about 1.12μs, reflect a non-negligible variation of temperature of the active region of the investigated VCSEL. This thermal effect is of course on the one hand due to the fact that the biased voltage is comparable to a pump current at the thermal rollover under continuous wave pumping conditions. On the other hand the high duty cycle of about 50% is responsible too, since the above mentioned value of τ_{th}=1.12μs has been observed for pulsing a comparable VCSEL with an oxide confined structure as well, however with a 5μs long square pulse with 1Hz repetition rate, thus resulting in a very low duty cycle of less then 1‰.

These experimental results demonstrate that the spectral redshift due to thermal heating of the VCSEL´s active region is the same for each particular transverse mode. On a basis of these findings a thermal time constant τ_{th} as a function of the bias voltage in combination with a fixed 120μs long square pulse for a fixed duty cycle of 50% will be derived by taken into account only one transverse mode in a particular step-scan measurement.
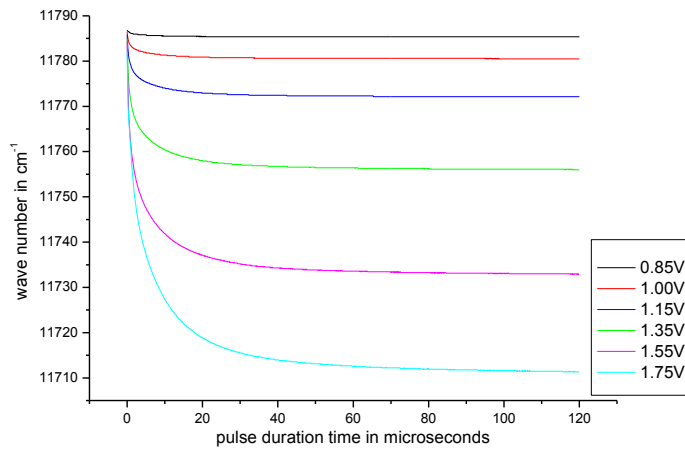
Figure 9.7 Maxima peak power values of one transverse mode for various applied voltages between 0.85V and 1.75V

		$\tilde{\lambda}(t) = \tilde{\lambda}_f - \Delta\tilde{\lambda} \exp\left(-\dfrac{t}{\tau_{th}}\right)$	
		Value	Standard Error
0.85V	$\tilde{\lambda}_f$	11785.36cm^{-1}	0.11cm^{-1}
	$\Delta\tilde{\lambda}$	0.99cm^{-1}	0.94cm^{-1}
	τ_{th}	5.74μs	0.81μs
1.00V	$\tilde{\lambda}_f$	11780.60cm^{-1}	0.46cm^{-1}
	$\Delta\tilde{\lambda}$	3.42cm^{-1}	0.36cm^{-1}
	τ_{th}	5.96μs	0.96μs
1.15V	$\tilde{\lambda}_f$	11772.28cm^{-1}	0.10cm^{-1}
	$\Delta\tilde{\lambda}$	8.09cm^{-1}	0.77cm^{-1}
	τ_{th}	6.12μs	0.89μs
1.35V	$\tilde{\lambda}_f$	11756.42cm^{-1}	0.21cm^{-1}
	$\Delta\tilde{\lambda}$	17.30cm^{-1}	0.15cm^{-1}
	τ_{th}	6.54μs	0.90μs
1.55V	$\tilde{\lambda}_f$	11733.60cm^{-1}	0.38cm^{-1}
	$\Delta\tilde{\lambda}$	31.45cm^{-1}	0.26cm^{-1}
	τ_{th}	7.47μs	0.95μs
1.75V	$\tilde{\lambda}_f$	11712.42cm^{-1}	0.48cm^{-1}
	$\Delta\tilde{\lambda}$	49.98cm^{-1}	0.30cm^{-1}
	τ_{th}	8.62μs	0.81μs

Table 9.2 Extracted fit parameter for different voltages

In Figure 9.7 the maximum peak values of the intensity of the representative dominant transverse mode as a function of time are depicted. Six different curves for applied voltages of 0.85V (black), 1.00V (red), 1.15V (blue), 1.35V (green), 1.55V (magenta) and 1.75V (turquoise) of each particular step-scan measurement are shown. These data have been obtained, utilizing no polarization selective optics, thus guaranteeing the detection of the particularly selected transverse mode. At a first glance, the different spectral redshift due to varying applied voltages are clearly visible. While the redshift is barely observable for the 0.85V square pulse, thus being in the range of 1cm^{-1} or 2cm^{-1}, the redshift becomes more obvious by increasing the applied voltage up to a value of 1.75V represented by turquoise data points. Here, an enormous redshift is observable and will be quantified via an exponential decay fit as it has been performed for the experimental data presented in Figure 9.6. The results of the redshift parameter $\Delta\tilde{\lambda}$ are depicted in Table 9.2 together with the other fitting parameter values, i.e. the steady state wave number $\tilde{\lambda}_f$ as well as the thermal time constant τ_{th}, which is the parameter of most interest. This thermal time constant τ_{th} has been estimated to be 8.6μs, thus being in good agreement with the above mentioned value, originating from a separate different measurement. However, the value of this thermal time constant τ_{th} decreases from 8.6μs down to 5.7μs by decreasing the applied voltage from 1.75V down to 0.85V. This value is already five times the value of 1.12μs obtained for a 5μs long square pulse with 1Hz repetition rate (duty cycle less then 1‰) [76], such that thermal effects of a 120μs long square pulse with a duty cycle of 50% cannot by neglected anymore.

In this final chapter of the experimental results, the step-scan technique was utilized to perform spectro-temporally resolved measurements of SPPs as well as to derive from them the fundamental thermal time constant τ_{th} of VCSELs. The results of SPPs($\tilde{\lambda}$,t) demonstrate a polarization switch determined by the polarization modes of the third transverse mode TM$_3$ that has never been experimentally observed before. Furthermore, a change of the polarization state as a function of time of the dominant second order transverse mode TM$_2$ was observed, reflected by a significant positive circular component. Moreover, it is found, that after a certain time the spectral redshift as well as the change of the polarization state of

each particular transverse mode reaches a steady state, such that these results are comparable with those obtained for continuous pumping condition.

In the following chapter all relevant experimental results of this thesis together with their cross-links as well as their physical explanations are summarized.

In this thesis the complex polarization behavior of VCSELs has been completely quantified via Stokes polarization parameters (SPPs). The manifold experimental investigations on pump current, spatially, spectrally, spatio-spectrally, time- and spectro-temporally resolved SPPs are abstractly illustrated in the pictogram below this passage. The green lines illustrate the crosscheck of results obtained via different experimental methods, thus making these findings even more reliable. These comprehensive investigations break down the complex polarization behavior of the total emission chapter by chapter into the rigorous decomposition of each particular transverse mode and in a further step even into their polarization mode components, both under continuous wave and pulsed operation.
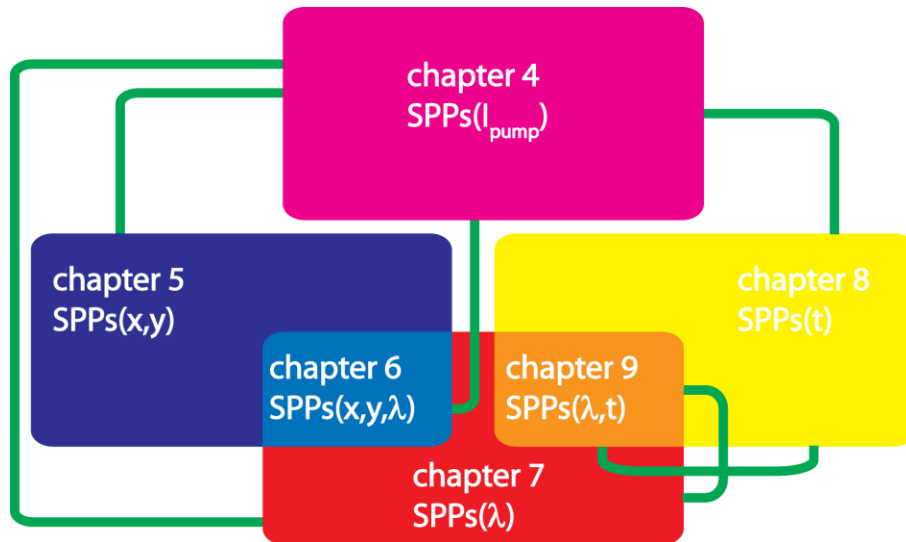
As a starting point, the polarization state of the total emission of VCSELs with different oxide aperture diameters, resulting in transverse single- and multi-mode emission, has been completely analyzed as a function of pump current in terms of SPPs. Beside polarization switching (PS) and polarization changing events that have already been observed by analyzing the polarization utilizing a linear polarizer only, a polarization analysis via Stokes formalism uncovers and quantifies additionally

1) the amount and orientation of the circular polarization component

2) the amount and orientation of the linear polarization component

3) and the degree of polarization (DOP).

In detail, we uncovered a large amount of the expected circular polarization component and quite surprisingly, we found a reduction of the DOP from 1 representing a fully polarized state of light, down to almost 0 reflecting an unpolarized state of light. The latter has been observed when increasing the oxide aperture diameter above 8μm which means that the

amount of emitting transverse modes significantly increases as well. This unpolarized state of light should be interesting for applications containing polarization selective optics. Here, some sort of polarization insensitivity of the divided intensity is realized. The important outcome is that experiments based only on a linear polarization projection, camouflage the full polarization state knowledge. Using SPPs, however, the full information about the polarization state of light is clearly visible, motivating spatially, spectrally and time-resolved measurements.

We have demonstrated that spatially resolved SPPs of a well-selected small-area transverse single-mode VCSEL with a monolithically integrated surface-grating on top to technologically control the polarization, show an inhomogeneous spatial distribution of the polarization. This has been predicted by theory and has even been experimentally demonstrated, however on a linear polarization projection basis only. We provide additional information to these preceding investigations, namely the spatially resolved SPPs uncover a four-lobe structure for $S_2(x,y)$ and even an eight-lobe structure for $S_3(x,y)$ both with characteristic change of sign patterns. These observed inhomogenous spatial polarization distributions in terms of SPPs(x,y) have been numerically simulated via the well-proven 3D VCSEL ELectroMagnetic (VELM) code. By utilizing this theoretical model, we have calculated the electromagnetic field of VCSELs including a monolithically integrated, circular symmetry breaking and polarization selective surface-grating. From the resulting complex electric field components, the SPPs(x,y) have been calculated and are in excellent agreement with their experimentally obtained counterparts. Beside the well reproduced change of sign pattern according to $S_2(x,y)$ and $S_3(x,y)$, the relative peak value of each SPP distribution has also been reproduced correctly. This agreement between experimentally obtained and numerically simulated spatially resolved SPPs, confirms the rigorous functionality of the 3D-VELM code with respect to the spatial distribution of polarization in terms of Stokes formalism and demonstrates that the measured SPP(x,y) patterns are consequently caused by the modal feature of the small-area VCSEL.

We have shown in detail that, by enlarging the diameter of the oxide aperture exceeding $3\mu m$, acts on the DOP such that its value differs significantly from 1, reflecting a transition from fully polarized to partially polarized light down to even unpolarized states of light for oxide aperture diameters exceeding $8\mu m$. To understand the physics behind the reduction of the DOP, a VCSEL with an oxide aperture diameter of $4\mu m$ has been investigated in more detail, where we have spectrally decomposed the SPPs to gain information about each particular transverse mode as a function of pump current. Whereas for all transverse modes the DOP shows a constant value very close to 1, independent of the pump current, the states of polarization turned out to be very different from each other, reflected by complementary signs according to their individual SPPs. Additionally, they exhibit changes of their values, when increasing the pump current. These different states of polarization, in detail their complementary sign for each SPP, result in the polarization state of the total emission and can be interpreted as the incoherent superposition of the SPPs of the individual transverse modes. This provides the explanation for the reduction of the DOP as it has been shown.

The spectral resolution of these spatio-spectrally resolved measurements was about 50pm at a wavelength of 850nm. We have deliberately enhanced this spectral resolution by utilizing a

FTIR-spectrometer instead of a grating spectrometer. Additionally, we have disclaimed the spatial resolution for the benefit of higher spectral resolution of about 5pm at 850nm, thus reflecting an improvement of a factor of 10. With this high spectral resolution we were able to resolve SPPs of polarization modes (belonging pairwise to one transverse mode), uncovering a constant state of polarization as a function of pump current. These constant contributions of the SPPs of the polarization modes in combination with the thermally induced spectral gain switching, results in polarization switching (PS) of some of the transverse modes. The change of the state of polarization of another transverse mode, especially its non-negligible amount of circular polarization at the thermally induced rollover, still has to be answered. Due to the fact, that from the measurements under continuous wave operation one cannot differentiate if this polarization dynamics is caused by applying different voltages or by thermal heating itself, we have performed time-resolved SPPs measurements of VCSELs under pulsed condition.

Unexpectedly, we have uncovered that time-resolved SPPs on a microsecond timescale of a VCSEL are in excellent correspondence with its pump current resolved SPPs. This coincidence allows us to forecast that thermal heating mainly causes the change of the state of polarization. We could exclude the influence of charge carrier dynamics by the selected voltage, which is completely applied to the VCSEL right after a few nanoseconds beyond the leading edge of the electrical pulse. In contrast to this fast rise time of the electrical pulse, the process of thermal heating is much slower and occurs on larger timescales, thus resulting in the complex polarization behavior observable on a microsecond timescale.

Finally we succeeded in determining time-resolved SPPs of each particular transverse mode exploiting the step-scan mode of the FTIR-spectrometer. Here, we were able to reveal complex polarization dynamics of individual transverse modes. In detail, this dynamics can strongly vary for various transverse modes. Additionally, the spectro-temporally resolved DOP is in agreement with the measurements of VCSELs under CW operation, such that its value for each particular transverse mode is above 0.7, close to an almost fully polarized state of light. Furthermore, the high spectral resolution of the step-scan method enables the observation of single polarization modes, uncovering a PS together with a spectral redshift in wave number both as a function of time. This spectral redshift has been quantified via an exponential decay fit to the spectro-temporally resolved peak intensity of each particular transverse mode determining a characteristic thermal time constant τ_{th} in the order of $9\mu s$. These numbers exceed other experimentally determined thermal time constant values ($\tau_{th}=1\mu s$) by almost an order of magnitude, which means that thermal heating cannot be neglected.

These comprehensively performed polarization analyses in terms of Stokes polarization parameters provide a basis of knowledge to support theoretical modelling. Even numerically simulated time- and spectro-temporally resolved SPPs would be of great interest to further investigate the influence of thermal heating on the polarization behavior. In addition to this, experimental investigations i.e. of the turn-on dynamics which is observable on a picosecond timescale, would provide an insight into the polarization dynamics, where thermal heating could be negligible and the influence of different voltages can be investigated. From the pump current resolved SPPs of the total emission we conclude that VCSELs with a well-selected oxide aperture diameter represent opto-electronic devices, with an intrinsically varying DOP,

which means that only by increasing the pump current the DOP can be continuously changed from 1 to 0 and vice versa, thus reflecting fully polarized and completely unpolarized light, respectively. This special feature enables VCSELs to be appropriate to further investigate the existing correlation between polarization and coherence.

11. Zusammenfassung

In dieser Arbeit wurde das komplexe Polarisationsverhalten von oberflächenemittierenden Halbleiterlasern mit Vertikalresonator (engl.: Vertical-Cavity Surface-Emitting Lasers, kurz: VCSELs) mittels Stokes-Formalismus umfassend untersucht. Dazu wurden eine Vielzahl diverser Untersuchungen zu Pumpstrom, räumlich-, spektral-, räumlich-spektral-, zeit- und spektral-zeitlich aufgelösten Stokes-Polarisations-Parametern (SPPn) durchgeführt und sind hier in einem Piktogram schematisch dargestellt. Die grünen Linien weisen hierbei auf eine Verifizierung der Messmethoden untereinander hin, was für eine starke Vernetzung und eine hohe Glaubwürdigkeit der in dieser Arbeit erzielten Ergebnisse spricht. Mittels dieser umfangreichen Untersuchungen war es möglich das komplexe Polarisationverhalten der Gesamtemission von VCSELn schrittweise von Kapitel zu Kapitel immer weiter aufzuschlüsseln und somit nicht nur jede einzelnen Transversalmode sondern auch die elementaren Polarisationsmoden quantitative zu untersuchen. Dieses Konzept fand Anwendung sowohl für Untersuchungen, unter Dauerstrich- als auch im gepulsten Betrieb.
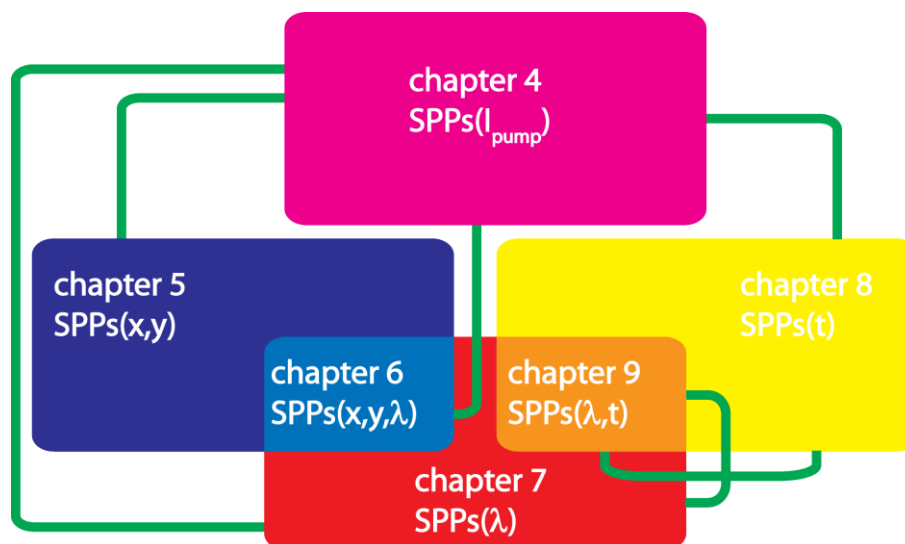
Zu Beginn der Ergebniskapitel wurden Polarisationszustände von VCSELn mit unterschiedlichen Oxidaperturdurchmessern zwischen 2μm und 10μm mit resultirendem transversal einmodigen und transversal mehrmodigen Emissionsverhalten vollständig mittels SPP analysiert und als Funktion des Pumpstroms aufgetragen. Neben den, bereits auf einer linearen Projektionsbasis beobachteten, Polarisationssprüngen (PS) lassen sich darüberhinaus die folgenden Polarisationseigenschaften quantifizieren:

1) Anteil und Orientierung der zirkularen Polarisation

2) Anteil und Orientierung der linearen Polarisation

3) Grad der Polarisation (engl.: degree of polarization, kurz: DOP).

Der hohe zirkular polarisierte Anteil mit S3≈-0.8 des vom VCSEL emittierten Lichts wurde auf Grund seiner zirkularen Resonatorgeometrie sowie des isotropen Gewinnmediums erwartet. Zusätzlich wurden linear polarisierter Anteile beobachtet, die sowohl durch eine leicht ovale, dem Herstellungsprozess geschuldeten, Resonatorform als auch durch Doppelbrechung der Multi-Halbleiterschichten entstehen. Etwas unerwartet zeigten die Ergebnisse eine Reduktion des DOP von 1 (vollständig polarisiertes Licht) auf fast 0 (unpolarisiertes Licht), wenn der Oxidaperturdurchmesser von 3μm auf 10μm vergrößert wird. Diese Vergrößerung hat darüber hinaus einen Übergang von transversal einmodiger zu transversal mehrmodiger Emission zur Folge. Das emittierte Licht von VCSELn mit Oxidaperturdurchmesser größer als 8μm ist unpolarisiert und für Anwendungen mit polarisations-selektiven Optiken insofern interessant, als dass unpolarisiertes Licht bis auf einen bestimmbaren Intensitätsverlust nicht wesentlich und vor allem nicht unvorhersagbar beeinflusst wird. Das wichtige Ergebnis ist, dass polarisationsaufgelöste Messungen die ausschließlich mittels Linearpolarisator durchgeführt werden, den komplexen Polarisationzustand von VCSELn nicht vollständig beschreiben. Im Gegensatz dazu wird mittels Stokes-Formalismus der Polarisationszustand vollständig quantifiziert und stellt somit eine Möglichkeit dar im Folgenden das komplexe Polarisationsverhalten der Gesamtemission weiter aufzuschlüsseln, was räumlich-, spektral- sowie zeitaufgelöste Messungen motiviert.

Räumlich aufgelöste SPP (SPP(x,y)) wurden an einem speziell ausgewählten, transversal einmodigen VCSEL mit monolitisch integriertem Oberflächengitter untersucht. Mittels Oberflächengitter ist es technologisch möglich, die Polarisation des VCSELs auf einen linear polarisierten Zustand zu fixieren. Trotzdem wurde hier eine räumlich inhomogene Polarisationsverteilung beobachtet, die theoretisch verhergesagt und bereits auf einer linear Projektionsbasis experimentell untersucht wurde. Die im Rahmen dieser Arbeit durchgeführten SPP(x,y) Messungen vervollständigen diese vorangegangenen Untersuchungen und konnten zusätzlich sowohl eine vier-Spot Struktur in $S_2(x,y)$ als auch eine acht-Spot Struktur in $S_3(x,y)$, beide charakterisiert durch einen Vorzeichenwechsel, erkennen. Diese experimentell bestimmten $SPP_{exp}(x,y)$ wurden mittels 3D-VCSEL ELectroMagnetic (VELM) Kode numerisch simuliert. Zunächst wurde hierzu das VELM Model an die entsprechende VCSEL Struktur angepasst wobei speziell das monolitisch integrierte und die zirkulare Symmetry brechende Oberflächengitter berücksichtig werden konnte. Ausgehend von den resultierenden komplexen elektrischen Feld Komponenten konnten die SPP berechnet und direkt mit den $SPP_{exp}(x,y)$ verglichen werden. Die korrespondieren SPP(x,y) zeigen eine gute Übereinstimmung und geben neben den experimentell beobachteten vier- und acht-Spot Strukturen zusätzlich das Verhältnis der Extremwerte der jeweiligen SPP(x,y) korrekt wieder. Diese Übereinstimmung zwischen experimentell bestimmten und numerisch simulierten SPPn bestätigt die rigorose Funktionalität des 3D-VELM Models in Bezug auf die vollständige Beschreibung der Polarisation. Darüber hinaus konnte erklärt werden, dass die Strukturen der SPP(x,y) durch die kurze (in longitudinaler Richtung) sowie leicht ovale (in transversaler Richtung) Resonatorgeometrie des transversal einmodigen VCSELs mit Oberflächengitter bestimmt werden.

Die im ersten Ergebniskapitel präsentierten SPP(I_{pump}) haben gezeigt, dass sich der Wert des DOP, bei Vergrößerung des Oxidaperturdurchmessers von 3μm auf 10μm, von 1 auf fast 0 reduziert. Um diese Reduktion des DOP physikalisch zu erklären, wurde das

Polarisationverhalten jeder einzelnen Transversalmode eines VCSELs mit $4\mu m$ Oxidaperturdurchmesser als Funktion des Pumpstroms untersucht. Hierzu wurden räumlich aufgelöste SPP sowie der DOP für jede einzelne Transversalmode als Funktion des Pumpstroms gemessen bzw. bestimmt. Diese räumlich-spektral aufgelösten Messungen (SPP(x,y,λ)) zeigen auf der einen Seite, dass der DOP bei allen Transversalmoden unabhängig vom Pumpstrom ist und einen Werte nahe bei 1 annimmt. Auf der anderen Seite ist das komplexe und von Transversalmode zu Transversalmode unterschiedliche Polarisationsverhalten zu beobachten und lässt sich wie folgt zusammenfassen. Zum einen fällt die ausgeprägte Dynamik der SPP als Funktion des Pumpstroms jeder einzelnen Transversalmode auf. Zum anderen zeigt sich zusätzlich das komplementäre Vorzeichen der jeweils gleichen SPP für unterschidliche Transversalmoden. Der Polarisationszustand der Gesamtemission resultiert aus den unterschiedlichen und vor allem komplementären SPP der einzelnen Transversalmoden und kann als deren inkohärente Superposition interpretiert werden. Dieses Ergebnis liefert die physikalische Erklärung für die experimentell beobachtete Reduktion des DOP.

Die spektrale Auflösung der oben beschriebenen räumlich-spekral aufgelösten SPPn beträgt 50pm bei einer Wellenlänge von 850nm. Diese Auflösung konnte erheblich verbessert werden indem ein FTIR-Spektrometer anstelle eines Gitterspektrometers verwendet wurde. Zusätzlich wurde bewußt auf die räumliche Auflösung verzichtet, um im Vergleich zur vorherigen Messung eine 10-fach höhere spektrale Auflösung von 5pm bei 850nm zu erreichen. Mit dieser hohen spektralen Auflösung war es möglich die SPP der Polarisationsmoden, welche paarweise zu einer Transversalmode gehören, spektral aufzulösen. Daher konnte beobachtet werden, dass Polarisationsmoden konstante sowie orthogonal zueinander orientierte Polarisationszustände als Funktion des Pumpstroms zeigen. Die konstanten Beiträge der SPP mit komplementären Vorzeichen in Kombination mit thermisch bedingtem Gewinnschalten in Bezug auf die Polarisationsmoden, resultiert in den beobachtbaren sprunghaften Polarisationsveränderungen (PS) einiger Transversalmoden. Das Ansteigen des zirkularen Anteils der Polarisation einer anderen Transversalmode am Rollover bleibt bis hier unbeantwortet. Da es nicht möglich war im Dauerstrichbetrieb zu unterscheiden ob sich die beobachtete Polarisationsdynamik aus den variierenden angelegten Spannungen oder der Thermik im VCSEL ergibt, wurden zeitaufgelöste Messungen auf Mikrosekunden Zeitskalen durchgeführt.

Überraschenderweise zeigen sowohl die im Pulsbetrieb gemessenen zeitaufgelösten SPP als auch die im Dauerstrichbetrieb experimentell bestimmten Pumpstrom aufgelösten SPP eine gute Übereinstimmung. Diese legt die Vermutung nahe, dass ausschließlich die Thermik für das komplexe Polarisationsverhalten verantwortlich ist und somit der Einfluß von Ladungsträgerdynamik ausgeschlossen werden kann. Im gepulsten Betrieb liegt die elektrische Spannung bei jedem Puls innerhalb weniger Nanosekunden vollständig an, während das thermische Aufheizen des VCSELs auf größeren Zeitskalen stattfindet und somit die Polarisationsdynamik auf Mikrosekunden Zeitskalen maßgeblich beinflusst.

Unter Verwendung des Step-Scan Modus des FTIR-Spektrometers konnte abschließend die komplexe Polarisationsdynamik der einzelnen Transversalmoden mittels SPP quantifiziert werden. Die Polarisationsdynamik ist für jede Transversalmode unterschiedlich stark

ausgeprägt und reicht von konstanten Beiträgen bis hin zur Veränderung einzelner SPP über die gesamte Pulslänge. Zusätzlich wurde anhand dieser Ergebnisse für alle Transversalmoden ein DOP von über 0.7 festgestellt, was mit den im Dauerstrich Modus spektral aufgelösten Ergebnissen übereinstimmt. Darüberhinaus, war es auf Grund der hohen spektralen Auflösung möglich das Verhalten der Polarisationsmoden spektral aufzulösen. Hierbei konnte sehr eindruckvoll sowohl der PS als Funktion der Zeit als auch die thermisch bedingte spektrale Rotverschiebung beobachtet werden. Diese Verschiebung wurde quantifiziert indem ein exponentieller Zerfall-Fit an die spektral-zeitlich aufgelösten Intensitätsmaxima der einzelnen Transversalmoden gelegt wurde. Die hieraus resultierende thermische Konstante τ_{th} beträgt ungefähr $9\mu s$ und ist im Vergleich zu bekannten Werten von $\tau_{th}=1\mu s$ um ein vielfaches erhöht. Diese Erhöhung weist daraufhin, das wie schon vorher vermutet das thermische Heizen des VCSELs nun nicht mehr vernachlässigt werden kann, sondern maßgeblich die Polarisationsdynamik auf den hier untersuchten Mikrosekunden Zeitskalen beeinflusst.

Die in dieser Arbeit erzielten umfangreiche Ergebnisse zu SPPn von VCSELn liefern zum einen physikalische Erklärungen für beobachtete Polarisationsphänomene. Zum anderen stellen diese umfangreichen Charakterisierungen des Polarisationsverhaltens, aufgeschlüsselt bis auf die elementaren Polarisationsmoden im Dauerstrich- sowie im gepulsten Betrieb eine fundamentale Basis und einen direkten Ansatzpunkt dar um bereits bestehende theoretische Modelle zu erweitern. Mittels numerischer Simulationen zu zeit- und spektral-zeitlich aufgelöster SPPn wäre es möglich den Einfluß des thermischen Heizens auf die Polarisationseigenschaften näher zu untersuchen. Zusätzlich würden experimentell bestimmte, auf Pikosekunden Zeitskalen aufgelöste SPP das Polarisationverhalten des Einschaltverhaltens vollständig beschreiben, wobei auf diesen Zeitskalen die Thermik vernächlässigt werden kann und nur der Einfluß der Ladungsträger im Modell berücksichtigt werden muss.

Es wurde gezeigt, dass bei VCSELn, je nach induziertem Pumpstrom und Größe ihres Oxidaperturdurchmessers, der DOP zwischen 1 und 0 maßgeschneidert werden kann. Diese intrinsische Eigenschaft von VCSELn, sowohl vollständig polarisiertes als auch unpolarisiertes Licht zu emittieren, ermöglicht es den fundamentalen Zusammenhang zwischen Polarisation und Kohärenz näher zu untersuchen.

Appendix

The experimental results on SPPs of MEMS tunable VCSELs, surface-grating VCSELs and standard VCSELs under mechanical stress together with spatially resolved SPPs below laser threshold are presented in appendix A, B and C, respectively. These results are a little out of thread regarding the main text; however, they are very interesting and worth being shown.

A.   Stokes polarization parameters of VCSELs with additional features

In appendix A experimental results on injection current resolved SPPs are presented for VCSELs with different additional structures, such as surface-gratings for polarization stabilization [60] as well as a micro-electro-mechanical-systems (MEMS) tunable mirror instead of the top DBR mirror for wide range tuneability in wavelength of more than 100nm [77].

Figure 0.1 shows representative nSPPs of VCSELs with an oxide aperture diameter of 10μm, thus resulting in transverse multi-mode emission. Moreover, two of these investigated devices have a monolithically integrated surface-grating on top to control the polarization technologically. As we have observed in chapter 4, a standard VCSEL, without surface-grating, together with a diameter of the oxide aperture of 10μm, shows an almost unpolarized state of light due to complementary contributions of each particular transverse mode. In addition to these results, the functionality of the surface-grating is clearly observable, which means that the state of polarization is fixed and stable, even when increasing the pump current up to the thermal rollover.

The difference between the investigated surface-grating VCSELs, which nSPPs are depicted in Figure 0.1b) and c) as a function of pump current is, that the orientations of their grating grooves are orthogonal to each other. This is visible from the sketches in Figure 0.1b) and c), where the orientation of the crystalline axes are additionally depicted.
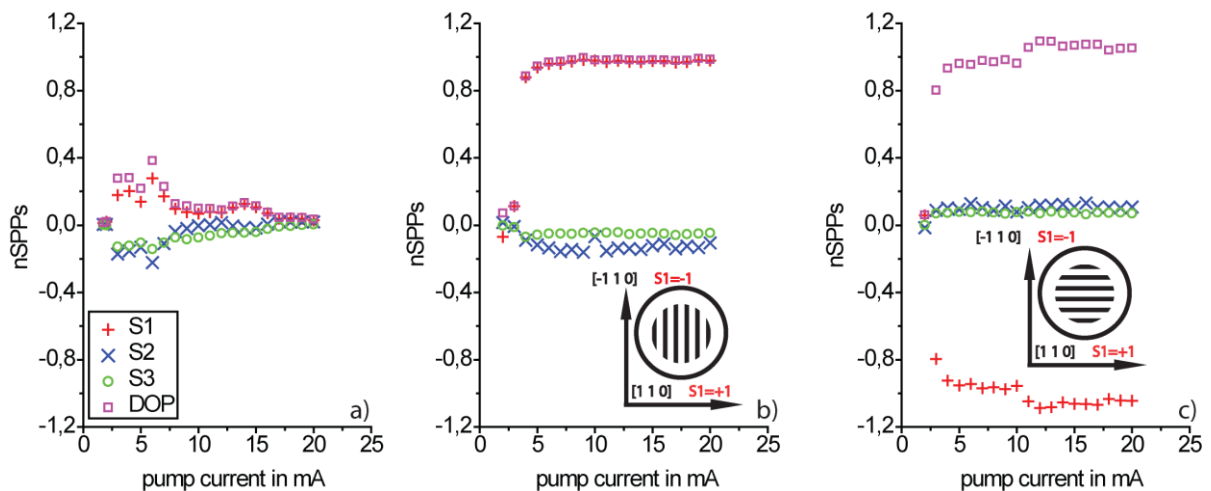
Figure 0.1 Normalized Stokes polarization parameters S_1 (red plus), S_2 (blue cross) and S_3 (green circle) together with the DOP (magenta square) as a function of pump current for a standard VCSEL without surface-grating a), a surface-grating VCSEL with grating grooves oriented along [-110] b) as well as oriented along [110] c), thus demonstrating the polarization controlling functionality of these surface-gratings.

The nSPPs(I_{pump}) of these three different devices, clearly demonstrate the functionality of these surface-gratings, as it has been already comprehensively investigated in [78]. Being in-line with a large amount of $S_1=1$ (red plus) and $S_1=-1$ (red plus) see Figure 0.1b) and c), respectively, together with almost negligible contributions of both S_2 (blue cross) and S_3 (green circle). Furthermore, the value of the DOP (magenta squares) is close to one for both surface-grating devices, which means that, in contrast to the unpolarized state of light, exhibited by the standard VCSEL (without surface-grating), the surface-grating controls the polarization and additionally leads to a fully polarized state of light.

A stable linear polarization together with a resulting high value of the DOP has also been observed for MEMS tunable VCSELs, exhibiting a tuning range of 80nm. These devices, emitting at a central wavelength of 1550nm, consist in principle of an active region, realized via a buried tunnel junction [79] which is typical for an emitting wavelength of 1550nm. The top DBR mirror is replaced by a MEMS tunable mirror, which enables a wide range tuneability of up to 100nm [77] [80] by inducing a certain current to the MEMS, resulting either in an enlargement or in a reduction of the optical cavity length.

As mentioned above, the tuneability of the investigated device is at least 80nm, clearly visible from Figure 0.2(left), where optical spectra at different MEMS current values are depicted, together with an envelope (black line) that has been recorded while the MEMS VCSEL was completely tuned. The optical spectra depicted in Figure 0.2(left) for six representative MEMS current values of 25.9mA, 30mA, 33mA, 35mA, 0mA and 18mA exhibit a central wavelength of the fundamental transverse mode of 1530nm (blue line), 1544nm (turquoise line), 1555nm (magenta line), 1565nm (yellow line), 1590nm (red line) and 1605nm (green line), respectively. From these results, the transverse single-mode operation of the MEMS tunable VCSEL is demonstrated over the entire tuning range of 80nm.
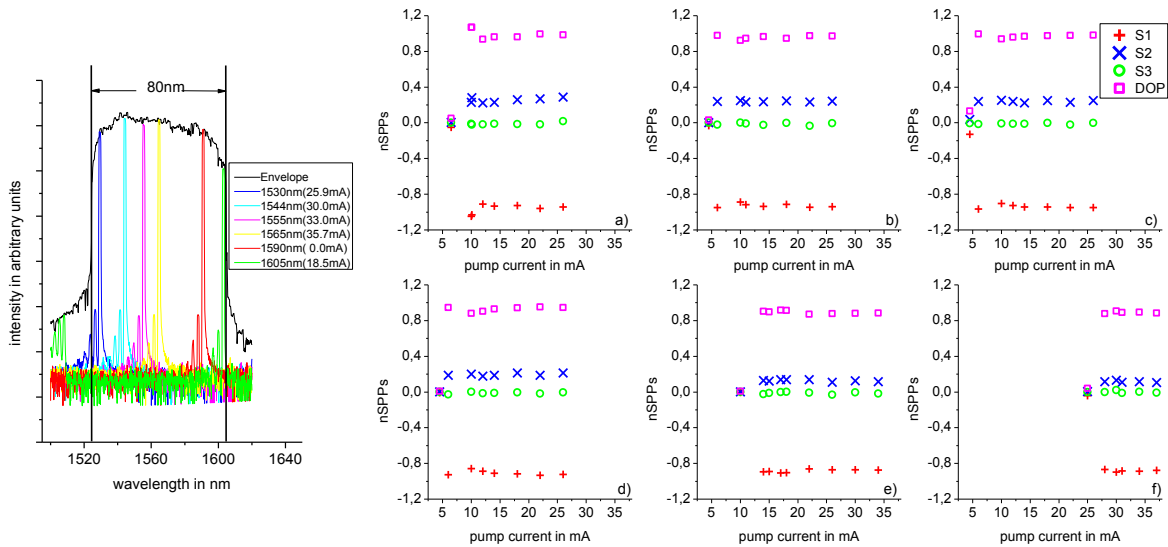
Figure 0.2 (left) Optical spectra of a MEMS tunable VCSEL are depicted for various MEMS current values (color coded) and explicitly given in the legend, demonstrating the tuneability of about 80nm. Right: Normalized Stokes polarization parameters S_1 (red plus), S_2 (blue cross) and S_3 (green circle) together with the DOP (magenta square) as a function of pump current a)—f) recorded according to six operating conditions, comparable to the results presented on the left. The results uncover a stable linear polarization together with an increase of the laser threshold observable in f).

The injection current resolved nSPPs, measured at these particular MEMS current values are depicted in Figure 0.2(right)a)-f). Here, the state of polarization is constant, represented by a dominant contribution of $S_1=-1$ (red plus), together with a small amount of S_2 of $+0.2$ (blue

cross) reflecting a small misalignment with respect to the crystaline axis of the MEMS VCSEL and a negligible value of S_3 (green circle). From these values the resulting values of the DOP (magenta squares) are close to one, reflecting a fully polarized state of light. For all different MEMS current values (25.9mA, 30mA, 33mA, 35mA, 0mA and 18mA) a polarization analysis right below the laser threshold has been performed. This uncovers an unpolarized state of light, due to spontaneous emission. Furthermore, a shift of the laser threshold to larger pump current values is clearly visible when comparing Figure 0.2(right) part d) and part f). Here the laser threshold shifts above a value of 25mA, due to a large spectral detuning between 1525nm and 1605nm with respect to the active material characteristic gain curve, nicely illustrated by the green curve in Figure 0.2(right)a) at the long-wavelength edge of the envelope (black line).

In conclusion, both additional features, namely the surface-grating on the one hand as well as the MEMS tunable mirror on the other hand, are controlling the polarization technologically. Furthermore, the wavelength can be tuned, additionally in a range of at least 80nm via a MEMS tunable mirror.

B. Tailored polarization states via mechanically induced stress on VCSELs

The influence of mechanical stress on the polarization behavior of VCSELs has already been investigated in [34] and [78], however, on a linear polarization projection basis only. The following results uncover that the two polarization modes of the fundamental transverse mode of a small-area VCSEL can exhibit a dominant circular polarization component.

The mechanical stress was induced via an especially for this measurement manufactured mount as it is observable in the photographical picture depicted in Figure 0.3(right). The VCSEL is glued to a common TO46 header. This header is positioned into the center hole and is fixed by utilizing a plastic pad. This can be accomplished with up to eight screws arranged in the periphery of a square around the VCSEL. Tightening or loosening screws in different holes leads to mechanical stress as bending the VCSEL with respect to different crystaline axis. With this method it is not possible to quantify the amount of mechanical stress applied to such a degree. However, a strong influence on the polarization behavior is clearly visible, regarding the SPPs S_0 (black star), S_1 (red plus), S_2 (blue cross) and S_3 (green circle) in μW, depicted in Figure 0.3(left) as a function of the mechanical stress in arbitrary units. The quantity we used here to evaluate the mechanically induced stress on the VCSEL is the detected optical output power of light $S_0^{'}(\beta = 0)$[22] after passing the combination of a quarter-wave plate and a linear polarizer. By tightening the screws the state of polarization continuously changes, as it is obvious from Figure 0.3(left). Furthermore, the total intensity represented by S_0 (black stars) remains constant at 800μW, which demonstrates, that the change in optical power of $S_0^{'}(\beta = 0)$, passing the quarter-wave plate and the linear polarizer, is only caused by a change of the state of polarization.
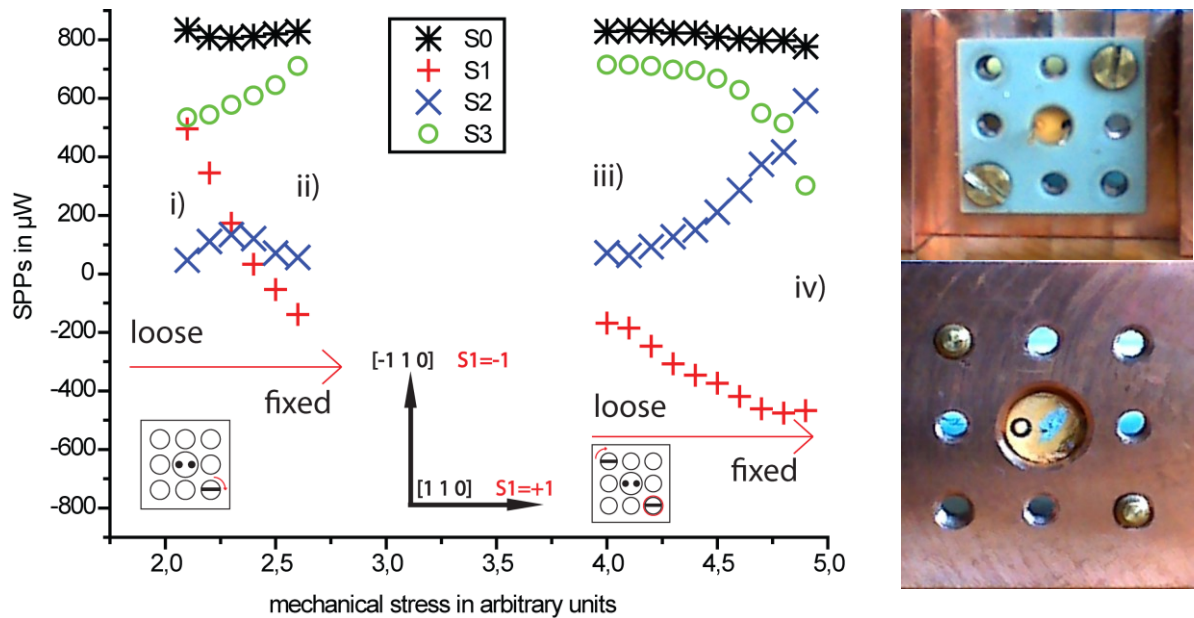
Figure 0.3 (left) Stokes polarization parameters S_0 (black star), S_1 (red plus), S_2 (blue cross) and S_3 (green circle), of a VCSEL at a constant pump current value of 2mA under various mechanical stress conditions, denoted by the sketches (insets). (right) Photographical pictures of the backside (top) and the front (bottom) of the real mount which enables to induce mechanical stress to the VCSEL via the screws.

---

[22] This value $S_0^{'}(\beta = 0)$ measured only at one angle β=0 of the quarter-wave plate has not to be distinguished with the determined total intensity S_0 of the VCSELs emitted light.

The transformation of the polarization state of light is depicted in Figure 0.3(left), represented by the non-normalized SPPs. The position of the screws is depicted as a sketch from the backside of the VCSEL´s mount, with the fixed screws represented by a red ring and the stepwise tightened screw with a red bended arrow together with the two connection pins of the VCSEL in the middle hole represented by two black dots. First, we use only one screw, put into the lower right hole and tighten it only so far, that the VCSEL just remains in the mount. In this position and with a pump current of 2mA (this pump current was used for all the measurements in this section) the state of polarization is elliptical, represented by almost the same contributions of S_1 (red plus) and S_3 (green circle) of 500μW as well as a negligible contribution of S_2 (blue cross) of almost 0μW together with S_0 (black star), representing the total emitted optical power of 800μW (Figure 0.3(left)i)). This value of S_0 (black star) remains constant, thus demonstrating that only the state of polarization is changed and nothing else.

By tightening the screw further, up to a point where it is really fixed, the state of polarization changes due to a dramatic gradual change of S_1 (red plus) from 500μW to -150μW, together with a small increase of S_3 (green circle) from 500μW up to 700μW and with an almost constant contribution of S_2 (blue cross) of below 100μW, clearly visible in Figure 0.3(left)ii). This state of polarization, with a dominant contribution of S_3 (green circle) is almost fully circular, together with small contributions of S_2 (blue cross) and S_1 (red plus).

By utilizing a second screw, the state of polarization can be even further tuned. Regarding the development of the SPPs from Figure 0.3(left)iii) to Figure 0.3(left)iv) here the states of polarization at ii) and iii) are almost identical, due to the negligible influence of the loose second screw, positioned in the upper left hole. That state of polarization gradually changes to a completely different state of polarization, by tightening the second crew, represented by a large amount of S_2 (blue cross) of 600μW as well as a large negative contributing value of S_1 (red plus) of -500μW together with a strongly reduced circular polarization component S_3 (green circle) of 300μW. In conclusion, the dominant circularly polarized state of light was transformed to an elliptical state of polarization, expressed by a characteristic contribution of the SPPs S_1 (red plus), S_2 (plus cross) and S3 (green circle).

This result clearly reveals that the amount of circular polarization can be increased, not only by optical injection of already circularly polarized light, as it has been demonstrated in [54] and [81], especially via electrical pumping [55] or utilizing an additional structure like a cholesteric liquid crystal (CLC-VCSEL) as it is reported in [82], but also by inducing mechanical stress. Attention should also be paid to the enormous tuneability of the state of polarization, which is demonstrated here for the first time.

Not only gradual changes of the state of polarization are observable. Furthermore, polarization switches both of type I and type II can be generated by mechanical stress as it has been reported in [34] and as it is illustrated in terms of nSPPs in Figure 0.4b). Moreover, the spatio-spectrally resolved SPPs depicted in Figure 0.4a) were measured right at the PS point at a pump current around 0.66mA, where an equal optical output power condition of both polarization modes can be observed in $S_0(x,y,\lambda)$. The complementary sign of S_1 and S_2 are clearly observable together with a large amount of circular polarization (S_3) above 0.6. Moreover, the DOP shows, that each polarization mode pm_left and pm_right are almost fully polarized reflected by their peak values above 0.7. These spatio-spectrally resolved results of the SPPs unambiguous reveal that each polarization mode of the fundamental transverse mode exhibits a large amount of circular polarization (S_3) by itself. $S_0(x,y,\lambda)$ nicely illustrates the quasi equal power condition of each polarization mode pm_left and pm_right. The complementary contributions of $S_1(x,y,\lambda)$ and $S_2(x,y,\lambda)$ in terms of negative values of $S_1(x,y,\lambda)$ and $S_2(x,y,\lambda)$ as well as the positive values of $S_1(x,y,\lambda)$ and $S_2(x,y,\lambda)$ of pm_left and

pm_right respectively, are explicitly observable together with a large amount of $S_3(x,y,\lambda)$, having a positive sign for both polarization modes. The resulting $DOP(x,y,\lambda)$ is depicted in Figure 0.4a), reflecting an almost fully polarized character of each particular polarization mode.
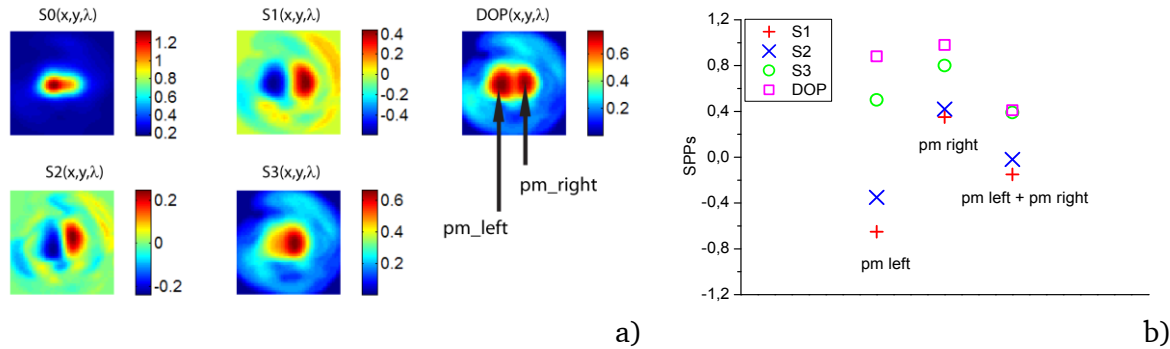

a)

b)

Figure 0.4 a) Spatio-spectrally resolved Stokes polarization parameters together with the DOP of the two polarization modes pm_left and pm_right. b) Normalized Stokes polarization parameters S_1 (red plus), S_2 (blue cross) and S_3 (green circle) together with the DOP (magenta square) for mechanical stress conditions with a dominant longer wavelength polarization mode (pm_left), a dominant shorter wavelength polarization mode (pm_right) and a condition where both polarization modes emit the same power (pm_left + pm_right).

In addition, the nSPPs of the total single-mode emission are shown in Figure 0.4b) taking into account both polarization modes. Here, the nSPPs of pm_left reveal a negative contribution of S_1 (red plus) and S_2 (blue cross) together with a positive contribution of S_3 (green circle), thus resulting in a value of the DOP (magenta square) of about 0.8. In contrast to these values, the nSPPs of pm_right exhibit by positive values of S_1, S_2 and S_3, together with a value of the DOP above 0.8. Moreover, the nSPPs of the state of polarization at equal power condition is visible, resulting in negligible contribution of S_2 and a small negative contribution of S_1. In combination with a large amount of S_3, the resulting value of the DOP is reduced to a value of 0.4 due to a incoherent superposition of the complementary contributing polarization modes. These results clearly demonstrate that even the polarization modes of the fundamental transverse mode exhibit a dominant amount of circular polarization.

C.   Spatially resolved Stokes polarization parameters below the laser threshold

The experimental results presented in the following, show spatially resolved SPPs of a standard VCSEL with an oxide aperture diameter of 10μm at a pump current value of 1mA, i.e. below the laser threshold such that only spontaneous emission is detected and analyzed. A photographic picture of a part of the wafer with the VCSELs is depicted in Figure 0.5(bottom right), showing the emitting VCSEL in the middle and two barely visible contact needles, necessary due to the flip chip wafer[23]. Beside the circular symmetry of the emitting facet with a Gaussian-shaped intensity distribution in transverse direction, a bright shining arc is observable above the emitting facet.

The spatially resolved Stokes polarization parameters $S_i(x,y)$ together with the DOP(x, y) are shown in Figure 0.5(left). The spontaneous emission directly in the middle of the emitting facet is characterized by a value of zero of $S_1(x,y)$, $S_2(x,y)$ and $S_3(x,y)$, together with a resulting DOP(x,y) of zero.
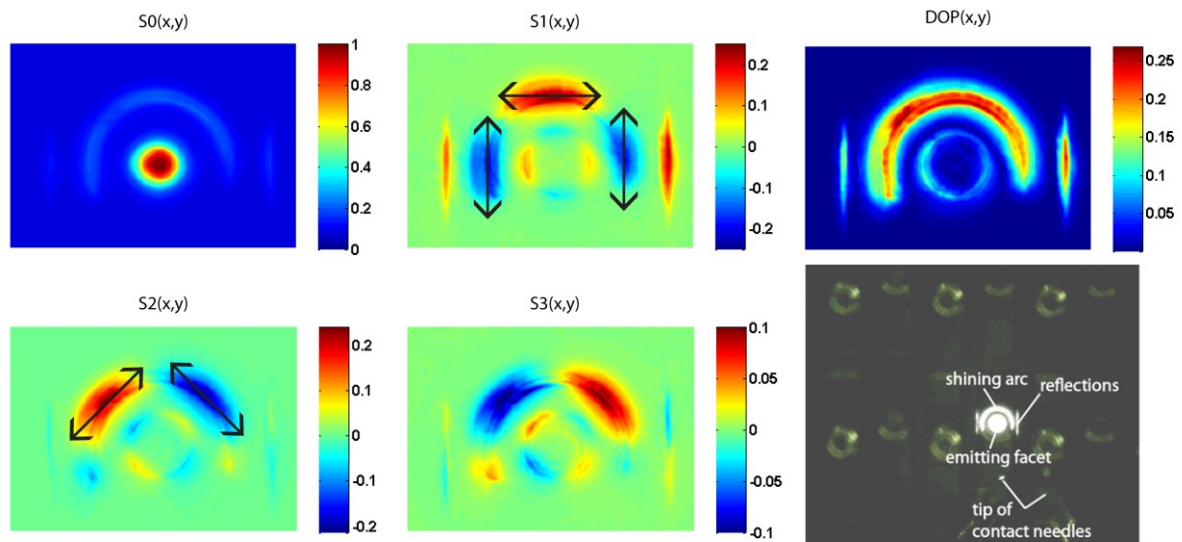
Figure 0.5 Spatially resolved normalized Stokes polarization parameters together with the DOP. Bottom right: Photographic picture of the wafer, showing the emitting facet and the contact needles.

Furthermore, an interesting pattern is visible, regarding the nSPPs(x,y), reflecting the orientation of the linear polarization being radially oriented according to the circular symmetry of the VCSEL. However, these nSPPs(x,y) have only a very small contribution in comparison to the total intensity. Moreover, the above mentioned arc has a change of sign pattern with respect to the nSPPs(x,y) and exhibit complementary signs in combination with larger values (range between -0.2 and +0.2) resulting in a DOP of roughly 0.25 for the entire arc. These interesting patterns arise from the reflection of the in-plane emission of the VCSEL as it is schematically depicted in Figure 0.6. This emission is linearly polarized caused by the geometry of the active layer in the longitudinal direction and with an orientation parallel to the semiconductor layers. This assumption explains the azimuthally oriented polarization, schematically suggested by black arrows visible in Figure 0.5.

---

[23] flip chip means, that both the n- as well as the p-contact pad are on top of the wafer
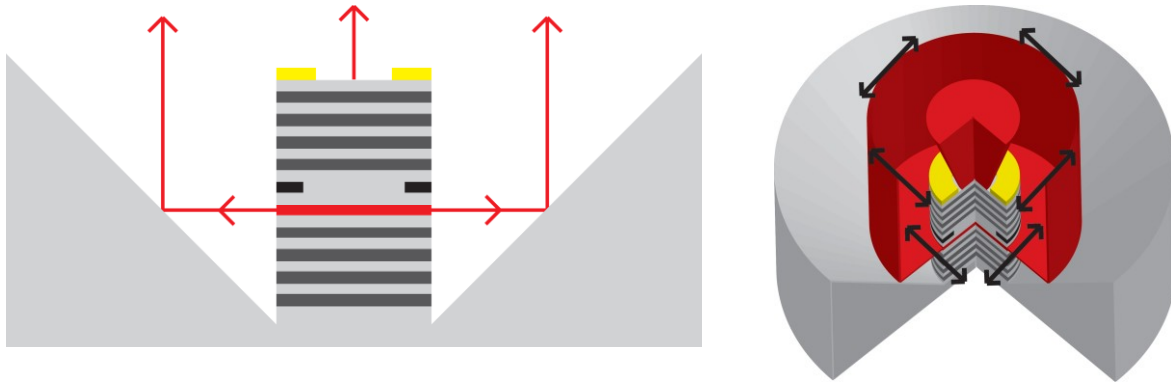
Figure 0.6 Schematic drawing of a VCSELs mesa together with the in-plane emission (red) reflected by the substrate material. Right: The orientation of the linear polarisation of the in-plane emission is illustrated by black arrows thus resulting in the observable azimuthally oriented polarisation of the arc.

Publications and Proceedings

A.   Journal papers

1) **A. Molitor**, M. Blazek, J.M. Ostermann, R. Michalzik, P. Debernardi, W. Elsäßer, "Investigations on the Intensity Noise of Surface Grating Relief VCSELs", *IEEE Journal of Quantum Electronics*, vol. 46, no. 4, pp. 554-561, (2010)

2) M. Blazek, S. Hartmann, **A. Molitor**, W. Elsäßer, "Unifying intensity noise and second-order coherence properties of amplified spontaneous emission sources", *Optics Letters*, vol. 36, no. 17, pp. 3455-3457, (2011)

3) **A. Molitor**, M. Blazek, W. Elsäßer, "Tailoring wave chaos in vertical-cavity surface-emitting lasers via polarization control", *Optics Letters*, vol. 36, no. 19, pp. 3777-3779, (2011)

4) **A. Molitor**, S. Hartmann, W. Elsäßer, "Stokes vector characterization of the polarization behavior of vertical-cavity surface-emitting lasers", *Optics Letters*, vol. 37, no. 22, pp. 4799-4801, (2012)

5) S. Hartmann, **A. Molitor**, M. Blazek, W. Elsäßer, "Tailored first and second order coherence properties of QD SLD via optical feedback", *Optics Letters*, vol. 38, no. 8, pp. 1334-1336, (2013)

6) **A. Molitor**, P. Debernardi, S. Hartmann, W. Elsäßer, "Spatially resolved Stokes parameters of small-area vertical-cavity surface-emitting lasers: experiment and simulation", *Optics Letters*, vol. 38, no. 22, pp. 4777-4780, (2013)

7) S. Hartmann, F. Friedrich, **A. Molitor**, M. Reichert, W. Elsäßer, R. Walser, "Tailored quantum statistics from broadband states of light", New J. Phys. vol. 17, 043039 (2015)

8) **A. Molitor**, S. Hartmann, W. Elsäßer, "Investigations on spatio-spectrally resolved Stokes polarization parameters of oxide-confined Vertical-Cavity Surface-Emitting Lasers", *Optics Letters*, vol. 40, no. 13, pp. 3121-3124, (2015)

9) **A. Molitor**, T. Mohr, S. Hartmann, W. Elsäßer, "Investigations on spectro-temporally resolved Stokes polarization parameters of transverse multi-mode Vertical-Cavity Surface-Emitting Lasers", *IEEE Journal of Quantum Electronics*, (submitted), (2015)

B. Conference proceedings

1) **A. Molitor**, M. Breuer, P. Debernardi, W. Elsäßer, "Investigations on wave chaos phenomena in VCSELs", in DPG-Frühjahrstagung Q 33.3, Hannover, Germany 2010 (talk)

2) **A. Molitor**, M. Breuer, P. Debernardi, W. Elsäßer, "Investigations on wave chaos phenomenon in VCSEL", in Optical Microcavities: Quantum Chaos in Open Systems Meets Optical Resonators 3rd Asian-German Workshop, Dresden, Germany 2010 (talk)

3) **A. Molitor**, W. Elsäßer, "Investigations on wave chaos phenomena in polarization-stabilized VCSELs", in European Semiconductor Laser Workshop, Pavia, Italy 2010 (talk)

4) **A. Molitor**, W. Elsäßer, "Transitions between regular and chaotic behavior in polarization-stabilized Vertical-Cavity Surface-Emitting Lasers", in Conference on Lasers and Electro-Optics/Europe - European Quantum Electronics Conference, CB-11.5, Munich, Germany 2011 (talk)

5) **A. Molitor**, M. Blazek, W. Elsäßer, "Wave chaos phenomena in Vertical-Cavity Surface-Emitting Lasers with and without polarization control", in 518. WE-Heraeus-Seminar on Quantum-Optical Analogies: a Bridge Between Classical and Quantum Physics, Bad Honnef, Germany 2012 (poster)

6) S. Hartmann, **A. Molitor**, M. Blazek, W. Elsäßer, "Investigations on photon statistics of Quantum-Dot-Superluminescent Diodes via Two-Photon-Absorption in semiconductors", in CFN Summer School 2012 on Nano-Photonics, Bad Herrenalb, Germany 2012 (poster)

7) **A. Molitor**, S. Hartmann, W. Elsäßer, "Stokes vector characterization of the polarization behavior of Vertical-Cavity Surface-Emitting Lasers", in European Semiconductor Laser Workshop, Brussels, Belgium 2012 (talk)

8) **A. Molitor**, M. Blazek, W. Elsäßer, "Tailoring wave chaos in VCSEL via polarization control", in Wave Chaos from the Micro- to the Macroscale, Dresden, Germany 2012 (poster)

9) **A. Molitor**, S. Hartmann, P. Debernardi, W. Elsäßer, "Spatially resolved Stokes parameters of small-area oxide-confined Vertical-Cavity Surface-Emitting Lasers", in Conference on Lasers and Electro-Optics/Europe - European Quantum Electronics Conference, CB-P.4, Munich, Germany 2013 (poster)

10) S. Hartmann, **A. Molitor**, M. Blazek, W. Elsäßer, "Photon Statistics of Quantum Dot Superluminescent Diodes at the Transition from Amplified Spontaneous Emission to Stimulated Emission", in Conference on Lasers and Electro-Optics/Europe - European Quantum Electronics Conference, CB-5.6, Munich, Germany 2013 (talk)

11) **A. Molitor**, S. Hartmann, P. Debernardi, W. Elsäßer, "Spatio-spectrally resolved Stokes parameters of Vertical-Cavity Surface-Emitting Lasers", in Conference on Lasers and Electro-Optics, San Jose, California, USA 2013 (talk)

12) **A. Molitor**, S. Hartmann, R. Michalzik, W. Elsäßer, "Spatially resolved Stokes parameters of Vertical-Cavity Surface-Emitting Lasers", in European Semiconductor Laser Workshop, Bristol, UK 2013 (talk)

13) **A. Molitor**, P. Debernardi, S. Hartmann, W. Elsäßer, "Spatially resolved Stokes parameters of small-area VCSEL: experiment and simulation", in DPG-Frühjahrstagung, Q30.43, Berlin, Germany 2014 (poster)

14) S. Paul, C. Gierl, **A. Molitor**, F. Küppers, "Characterization of the Stokes parameters of the polarization behavior of the 1550 nm MEMS tunable VCSEL", in European VCSEL Day, Rennes, France 2014 (talk)

Bibliography

[1] K. Iga, "Surface-Emitting Laser - Its Birth and Generation of New Optoelectronics Field," *IEEE Journal on Selected Topics in Quantum Electronics,* vol. 6, no. 6, pp. 1201-1215, 2000.

[2] K. Iga, "Vertical-Cavity Surface-Emitting Laser: Its Conception and Evolution," *Japan Journal of Applied Physics,* vol. 47, no. 1, pp. 1-10, Jan 2008.

[3] P. S. Zory, Quantum Well Lasers, London: Academic Press, 1993.

[4] M. Y. A. Raja, S. R. J. Brueck, M. Osinski, C. F. Schaus, J. G. McInerney, T. M. Brennan and B. E. Hammons, "Surface-emitting, multiple quantum well GaAs/AlGaAs laser with wavelength-resonant periodic gain medium," *Appl. Phys. Lett.,* vol. 53, no. 18, pp. 1678-1680, 1998.

[5] D. Bimberg and U. W. Pohl, "Quantum dots: promises and accomplishments," *material today,* vol. 14, no. 9, pp. 388-397, 2011.

[6] J. P. Woerdman, A. K. J. v. Doorn and M. P. v. Exter, "Symmetry Breaking in Vertical-Cavity Semiconductor lasers," *Laser Physics,* vol. 7, no. 1, pp. 63-67, 1997.

[7] A. K. J. v. Doorn, M. P. v. Exter and a. J. P. Woerdman, "Strain-induced birefringence in vertical-cavity semiconductor lasers," *IEEE Journal of Quantum Electronics,* vol. 34, no. 4, pp. 700-706, 1998.

[8] F. Monti di Sopra, M. Brunner and R. Hövel, "Polarization control in strained T-bar VCSELs," *IEEE Journal of Quantum Electronics,* vol. 14, no. 8, pp. 1034-1036, 2002.

[9] C. Degen, I. Fischer, W. Elsäßer, L. Fratta, P. Debernardi, G. Bava, M. Brunner, R. Hövel, M. Moser and K. Gulden, "Transverse modes in thermally detuned oxide-confined vertical-cavity surface-emitting lasers," *Physical Review A,* vol. 63, no. 023817, pp. 1-12, Jan 2001.

[10] S. Balle, E. Tolkachova, M. San Miguel, J. R. Tredicce, J. Martin-Regalado and A. Gahl, "Mechanisms of polarization switching in single-transverse-mode vertical-cavity surface-emitting lasers: thermal shift and nonlinear semiconductor dynamics," *Optics Letters,* vol. 24, no. 6, pp. 1121-1123, 1999.

[11] R. F. M. Hendriks, M. P. v. Exter, J. P. Woerdman, K. H. Gulden and M. Moser, "Memory Effect for Polarization of Pump Light in Optically Pumped Vertical-Cavity Semiconductor Lasers," *IEEE Journal of Quantum Electronics,* vol. 34, no. 8, pp. 1455-1460, 1998.

[12] M. P. v. Exter, A. K. J. v. Doorn and J. P. Woerdman, "Electro-optic effect and birefringence in semiconductor vertical-cavity lasers," *Physical Review A,* vol. 56, no. 1, pp. 845-853, 1997.

[13] M. P. v. Exter, R. F. M. Hendriks and J. P. Woerdman, "Physical insight into the polarization dynamics of semiconductor vertical-cavity lasers," *Physical Review A,* vol. 57, no. 3, pp. 2080-2090, 1998.

[14] A. K. J. v. Doorn, M. P. v. Exter, M. Travagnin and J. P. Woerdman, "Polarization behavior of surface-emitting semiconductor lasers in an axial magnetic field," *Optics Communications,* vol. 133, pp. 252-258, 1997.

[15] A. Molitor, M. Blazek, J. M. Ostermann, R. Michalzik, P. Debernardi and W. Elsäßer, "Investigations on the Intensity Noise of Surface Grating Relief VCSELs," *IEEE Journal of Quantum Electronics,* vol. 46, no. 4, pp. 554-561, 2010.

[16] A. Molitor, M. Blazek and W. Elsäßer, "Tailoring wave chaos in vertical-cavity surface-emitting lasers via polarization control," *Optics Letters,* vol. 36, no. 19, pp. 3777-3779, 2011.

[17] P. Debernardi, G. P. Bava, C. Degen, I. Fischer and W. Elsäßer, "Influence of Anisotropies on Transverse Modes in Oxide-Confined VCSELs," *IEEE Journal of Quantum Electronics,* vol. 38, no. 1, pp. 73-84, 2002.

[18] C. Degen, B. Krauskopf, G. Jennemann, I. Fischer and W. Elsäßer, "Polarization selective symmetry breaking in the near-fields of vertical cavity surface emitting lasers," *J. Opt. B: Quantum Semiclass. Opt.,* vol. 2, pp. 517-515, 2000.

[19] A. Barchanski, T. Gensty, C. Degen, I. Fischer and W. Elsäßer, "Picosecond emission dynamics of vertical-cavity surface-emitting lasers: Spatial, spectral, and polarization-resolved characterization," *IEEE Journal of Quantum Electronics,* vol. 39, no. 7, pp. 850-858, Jul 2003.

[20] C. Fuchs, T. Gensty, P. Debernardi, G. P. Bava, J. M. Ostermann, R. Michalzik, A. Haglund, A. Larsson and W. Elsäßer, "Spatiotemporal Turn-On Dynamics of Grating Relief VCSELs," *IEEE Journal of Quantum Electronics,* vol. 43, no. 12, pp. 1227-1234, Dec 2007.

[21] G. G. Stokes, "On the composition and resolution of streams of polarized light from different sources," *Transactions of the Cambridge Philosophical Society,* vol. 9, no. 399, pp. 233-258, 1852.

[22] C. W. Wilmsen, H. Temkin and L. A. Coldren, Vertical-Cavity Surface-Emtting Lasers, Cambridge: Cambridge University Press, 1999.

[23] H. Li and K. Iga, Vertical-Cavity Surface-Emitting Laser Devices, Berlin: Springer, 2003.

[24] S. Yu, Analysis and Design of Vertical Cavity Surface Emitting Lasers, Hoboken: Wiley, 2003.

[25] R. Michalzik, VCSELs - Fundamentals, Technology and Applications of Vertical-Cavity Surface-Emitting Lasers, Berlin: Springer, 2013.

[26] W. W. Chow, S. W. Koch and M. Sargent, Semiconductor-Laser Physics, Berlin: Springer, 1994.

[27] D. L. Huffaker, L. A. Graham, H. Deng and D. G. Deppe, "Sub-40μA continuous-wave lasing in an oxidized vertical-cavity surface emitting laser with dielectric mirrors," *IEEE Photonics Technology Letters,* vol. 8, no. 8, pp. 974-976, 1996.

[28] M. Grabherr, M. Miller, R. Jäger, R. Michalzik, U. Martin, H. Unold and K. J. Ebeling, "High-power VCSELs: single devices and densely packed 2-D-arrays," *IEEE Journal of Selected Topics in Quantum Electronics,* vol. 5, no. 3, pp. 495-502, 1999.

[29] M. Miller, M. Grabherr, R. King, R. Jäger, R. Michalzik and K. J. Ebeling, "Improved output performance of high-power VCSELs," *IEEE Journal on Selected Topics in Quantum Electronics,* vol. 7, no. 2, pp. 210-216, 2001.

[30] A. E. Siegman, Laser, Mill Valley: University Science Books, 1986.

[31] L. A. Coldren, S. W. Corzine and M. L. Mašanović, "Appendix 10: Transition Matrix Elements," in *Diode Lasers and Photonic Integrated Circuits 2nd Edition*, New Jersey, Wiley, 2012, pp. 639-646.

[32] M. San Miguel, Q. Feng and J. V. Moloney, "Light-polarization dynamics in surface-emitting semiconductor lasers," *Physical Review A,* vol. 52, no. 2, pp. 1728-1739, 1995.

[33] C. Degen, I. Fischer and W. Elsäßer, "Transverse modes in oxide confined VCSELs: Influence of pump profile, spatial hole burning, and thermal effects," *Optics Express,* vol. 5, no. 3, pp. 38-47, 1999.

[34] K. Panajotov, B. Nagler, G. Verschaffelt, A. Georgievski, H. Thienpont, J. Danckaert and I. Veretennicoff, "Impact of in-plane anisotropic strain on the polarization behavior of vertical-cavity surface-emitting lasers," *Applied Physics Letters,* vol. 77, no. 11, pp. 1590-1592, 2000.

[35] G. Verschaffelt, K. Panajotov, J. Albert, B. Nagler, M. Peeters, J. Danckaert, I. Veretennicoff and H. Thienpont, "Polarisation switching in vertical-cavity surface-emitting lasers: from experimental observations to applications," *Opto-Electronics Review,* vol. 9, no. 3, pp. 257-268, 2001.

[36] T. Ackemann and M. Sondermann, "Characteristics of polarization switching from the low to the high frequency mode in vertical-cavity surface-emitting lasers," *Applied Physics Letters,* vol. 78, no. 23, pp. 3574-3576, 2001.

[37] K. D. Choquette, R. P. Schneider-Jr., K. L. Lear and R. E. Leibenguth, "Gain dependent polarization properties of vertical-cavity lasers," *IEEE Journal of Selected Topics in Quantum Electronics,* vol. 1, no. 2, pp. 661-666, 1995.

[38] C. Brosseau, Fundamentals of polarized light - A statistical optics approach, New York: Wiley inter science, 1998.

[39] E. Collett, Polarized Light - Fundamentals and Applications, New York: Marcel Dekker, 1993.

[40] W. Shurcliff, Polarized Light, Cambridge: Harvard University Press, 1962.

[41] M. Born and E. Wolf, Principles of Optics - Electromagnetic Theory of Propagation, Interference and Diffraction of Light 4th Edition, Great Britain: Pergamon Press, 1970.

[42] E. Wolf, Introduction to the Theory of Coherence and Polarization of Light, Cambridge: Cambridge University Press, 2007.

[43] E. Wolf, "Unified theory of coherence and polarization of random electromagnetic beams," *Physics Letters A,* vol. 312, pp. 263-267, 2003.

[44] U. Fano, "A Stokes-Parameter Technique for the Treatment of Polarization in Quantum Mechanics," *Physical Review,* vol. 93, no. 1, pp. 121-123, 1954.

[45] R. W. Schmieder, "Stokes-Algebra Formalism," *Journal of the Optical Society of America,* vol. 59, no. 3, pp. 297-302, 1969.

[46] M. V. Trantnki and J. E. Sipe, "Stokes vectors and polarization lasers," *J. Opt. Soc. Am. B,* vol. 2, no. 10, pp. 1690-1695, 1985.

[47] F. M. Cady and D. Krings, "Spatially resolved Stokes vector measurements," *Review of Scientific Instruments,* vol. 69, no. 10, pp. 3491-3493, 1998.

[48] H. G. Berry, G. Gabrielse and A. E. Livingston, "Measurement of the Stokes parameters of light," *Applied Optics,* vol. 16, no. 12, pp. 3200-3206, 1977.

[49] B. Schaefer, E. Collett, R. Smyth, D. Barrett and B. Fraher, "Measuring the Stokes polarization parameters," *American Journal of Physics,* vol. 75, no. 2, pp. 163-168, 2007.

[50] N. V. D`yachkov and A. P. Bogatov, "Measuring the Stokes parameters of radiation of semiconductor lasers," *Quantum Electronics,* vol. 41, no. 10, pp. 869-874, 2011.

[51] R. Castagna, D. E. Lucchetta, F. Vita, L. Criante and F. Simoni, "At a glance determination of laser light polarization state," *Applied Physics Letters,* vol. 92, no. 041115, pp. 1-3, 2008.

[52] R. D. Ramkhalawon, T. G. Brown and M. A. Alonso, "Imaging the polarization of a light field," *Optics Express,* vol. 21, no. 4, pp. 4106-4115, 2013.

[53] F. S. White and H. E. Jenkins, Fundamentals of optics, New York: McGraw-Hill, 1957.

[54] P. Bhattacharya, M. Holub and D. Saha, "Spin-polarized surface-emitting lasers," *phys. stat. sol. (c),* vol. 3, no. 12, pp. 4396-4400, Dec 2006.

[55] M. Holub, J. Shin, D. Saha and P. Bhattacharya, "Electrical Spin Injection and Threshold Reduction in a Semiconductor Laser," *Physical Review Letters,* vol. 98, no. 146603, pp. 1-4, Apr 2007.

[56] N. C. Gerhardt and M. R. Hofmann, "Spin-Controlled Vertical-Cavity Surface-Emitting Lasers," *Advances in Optical Technologies,* vol. Article ID 268949, 2012.

[57] W. L. Erikson and S. Singh, "Polarization properties of Maxwell-Gaussian beams," *Physical Review E,* vol. 49, no. 6, pp. 5778-5786, 1994.

[58] T. G. Brown and Q. Zhan, "Focus Issue: Unconventional Polarization States of Light," *Optics Express,* vol. 18, no. 10, pp. 1-2, 2010.

[59] L. Fratta, P. Debernardi, G. P. Bava, C. Degen, J. Kaiser, I. Fischer and W. Elsäßer, "Spatially inhomogeneously polarized transverse modes in vertical-cavity surface-emitting lasers," *Physical Review A,* vol. 64, no. 031803, pp. 1-3, Aug 2001.

[60] P. Debernardi, J. M. Ostermann, M. Feneberg, C. Jalics and R. Michalzik, "Reliable polarization control of VCSELs through monolithically integrated surface gratings: a comparative theoretical and experimental study," *IEEE Journal of Selected Topics in Quantum Electronics,* vol. 11, no. 1, pp. 107-116, 2005.

[61] P. Debernardi and G. P. Bava, "Coupled mode theory: A powerful tool for analyzing complex VCSELs and designing advanced device features," *IEEE Journal of Selected Topics in Quantum Electronics,* vol. 9, no. 3, pp. 905-917, May 2003.

[62] N. V. D`yachkov and A. P. Bogatov, "Stokes parameters of the radiation of transverse.single-mode InGaAs/AlGaAs lasers with a quantum-well active region," *Quantum Electronics,* vol. 41, no. 1, pp. 20-25, 2011.

[63] A. Molitor, P. Debernardi, S. Hartmann and W. Elsäßer, "Spatially resolved Stokes parameters of small-area vertical-cavity surface-emitting lasers: experiment and simulation," *Optics Letters,* vol. 38, no. 22, pp. 4777-4780, 2013.

[64] P. Debernardi, R. Orta, T. Gründl and M.-C. Amann, "{3-D} Vectorial Optical Model for High-Contrast Grating Vertical-Cavity Surface-Emitting Lasers," *IEEE Journal of Quantum Electronics,* vol. 49, no. 2, pp. 137-145, Feb 2013.

[65] A. Molitor, S. Hartmann and W. Elsäßer, "Stokes vector characterization of the polarization behavior of vertical-cavity surface-emitting lasers," *Optics Letters,* vol. 37, no. 22, pp. 4799-4801, 2012.

[66] K. Panajotov, J. Danckaert, G. Verschaffelt, M. Peeters, B. Nagler, J. Albert, B. Ryvkin, H. Thienpont and I.Veretennicoff, "Polarization behavior of vertical-cavity surface-emitting lasers: experiments, models and applications," *American Institute of Physics Conference Proceeding,* vol. 56396, pp. 403-417, 2001.

[67] G. W. Taylor and P. A. Evaldsson, "Temperatur Dependent Operation of the Vertical Cavity Surface Emitting Laser," *IEEE Journal of Quantum Electronics,* vol. 30, no. 10, pp. 2262-2270, 1994.

[68] M. B. Willemsen, M. U. F. Khalid, M. P. v. Exter and J. P. Woerdman, "Polarization Switching of a Vertical-Cavity Semiconductor Laser as a Kramers Hopping Problem," *Physical Review Letters,* vol. 82, no. 24, pp. 4815-4818, 1999.

[69] M. B. Willemsen, M. P. v. Exter and J. P. Woerdman, "Anatomy of a Polarization Switch of a Vertical-Cavity Semiconductor Laser," *Physical Review Letters,* vol. 84, no. 19, pp. 4337-4340, 2000.

[70] O. Buccafusa, J. L. A. Chilla, J. J. Rocca, S. Feld, C. Wilmsen, V. Morozov and R. Leibenguth, "Transverse mode dynamics in vertical cavity surface emitting lasers excited by fast electrical pulses," *Applied Physics Letters,* vol. 68, no. 5, pp. 590-592, 1996.

[71] J. Mulet and S. Balle, "Spatio-Temporal Modeling of the Optical Properties of VCSELs in the Presence of Polarization Effects," *IEEE Journal of Quantum Electronics,* vol. 38, no. 3, pp. 291-305, 2002.

[72] J. Martín-Regalado, F. Prati, M. San Miguel and N. B. Abraham, "Polarization Properties of Vertical-Cavity Surface-Emitting Lasers," *IEEE Journal of Quantum Electronics,* vol. 33, no. 5, pp. 765-783, 1997.

[73] M. Virte, K. Panajotov, H. Thienpont and M. Sciamanna, "Deterministic polarization chaos from a laser diode," *nature photonics,* vol. 7, pp. 60-65, 2012.

[74] T. Setälä, A. Shevchenko, M. Kaivola and A. T. Friberg, "Polarization time and length for random optical beams," *Physical Review A,* vol. 78, no. 033817, pp. 1-6, 2008.

[75] M. Marconi, S. Barland and M. Giudici, "VCSEL, Nonvolatile polarization control of a bistable," *Optics Express,* vol. 20, no. 26, pp. 299-305, 2012.

[76] J. Martín-Regalado, *Polarization properties of Vertical-Cavity Surface-Emitting Lasers,* 1997.

[77] C. Gierl, Mikromechanisch weit abstimmbare Oberflächen-emittierende Laser mit Vertikalresonator, Göttingen: Cuvillier, 2013.

[78] J. M. Ostermann, Diffrative optics for polarization control of Vertical-Cavity Surface-Emitting Lasers, Göttingen: Cuvillier, 2007.

[79] M. Ortsiefer, R. Shau, G. Böhm, F. Köhler, G. Abstreiter and M.-C. Amann, "Low-resistance InGa(Al)As Tunnel Junctions for Long Wavelength Vertical-Cavity Surface-Emitting Lasers," *Japanese Journal of Applied Physics,* vol. 1, no. 4, pp. 1727-1729, 2000.

[80] C. Gierl, T. Gruendl, P. Debernardi, K. Zogal, C. Grasse, H. A. Davani, G. Böhm, S. Jatta, F. Küppers, P. Meißner and M.-C. Amann, "Surface micromachined tunable 1.55 μm-VCSEL with 102nm continous single-mode tuning," *Optics Express,* vol. 19, no. 18, pp. 17336-17343, 2011.

[81] K. Ikeda, T. Fujimoto, H. Fujino, T. Katayama, S. Koh and H. Kawaguchi, "Switching of Lasing Circular Polarizations in a (110)-VCSEL," *IEEE Photonics Technology Letters,* vol. 21, no. 18, pp. 1350-1352, 2009.

[82] K. Panajotov, Y. Xie, M. Dems, C. Belmonte, H. Theinpont, J. Beeckman and K. Neyts, "Vertical-cavity surface-emitting laser emitting circularly polarized light," *Laser Physics Letters,* vol. 10, no. 105003, pp. 1-5, 2013.

[83] A. K. J. v. Doorn, M. P. v. Exter, A. M. v. d. Lee and J. P. Woerdman, "Coupled-mode description for the polarization state of a vertical-cavity surface-emitting laser," *Physical Review A,* vol. 55, no. 2, pp. 1473-1484, 1997.

[84] M. Schulz-Ruhtenberg, Y. Tanguy, R. Jäger and T. Ackemann, "Length scales and polarization properties of annular standing waves in circular broad-area vertical-cavity surface-emitting lasers," *Applied Physics B: Lasers and Optics,* vol. 97, no. 2, pp. 397-403, 2009.

[85] I. V. Babushkin, M. Schulz-Ruhtenberg, N. A. Loiko, K. F. Huang and T. Ackemann, "Coupling of Polarization and Spatial Degrees of Freedom of Highly Divergent Emission in Broad-area Square Vertical-Cavity Surface-Emitting Lasers," *Physical Review Letters,* vol. 100, no. 213901, pp. 1-4, 2008.

Acknowledgement

To express my gratefulness in appropriate manner I switch language from english to german with one exception.

Danksagung

Curriculum Vitae

2009-2014	Promotion in the group of Prof. Elsäßer at Technische Universität Darmstadt, Germany Title: *Investigations on Stokes polarization parameters of Vertical-Cavity Surface-Emitting Lasers: spatially, spectrally and time-resolved*
2009	Diploma thesis in the group of Prof. Elsäßer at Technische Universität Darmstadt, Germany Title: *Untersuchungen zum Intensitätsrauschen an polarisationsstabilen VCSELn*
2001-2009	Physics studies at the Technischen Universität Darmstadt, Germany

Erklärungen

Selbstständigkeitserklärung

Hiermit erkläre ich, dass ich die vorliegende Arbeit „Investigations on Stokes polarization parameters of Vertical-Cavity Surface-Emitting Lasers: spatially, spectrally and time-resolved" selbstständig verfasst und keine anderen als die angegebenen Quellen und Hilfsmittel verwendet habe.

Bürstadt, 19. November 2014

Andreas Molitor

Erklärung über frühere Promotionsversuche

Hiermit erkläre ich, dass von mir keine früheren Promotionsversuche mit dieser oder einer anderen Dissertation erfolgt sind. Die vorliegende Arbeit wurde bisher weder im In- noch im Ausland in gleicher oder ähnlicher Form einer anderen Prüfungsbehörde vorgelegt.

Bürstadt, 19. November 2014

Andreas Molitor